INSTITUTO SUPERIOR TÉCNICO
Universidade Técnica de Lisboa

Multiaxial Fatigue Simulation of an AZ31 Magnesium Alloy using ANSYS and a Plasticity Program

Agostinho Matos

Master's Thesis in

Aerospace Engineering

Jury

President:	Prof. Fernando Lau
Supervisors:	Prof. Luís Filipe Galrão dos Reis
	Prof. Manuel José Freitas
Examiners:	Prof. Virgínia Isabel Infante
	Prof. Bin Li

October 2010

Acknowledgments

I want to thank to Professor Luís Reis for his availability to discuss multiaxial fatigue theories and critics, to Professor Manuel Freitas for his participation in taking decisions about how the data results should be presented and to Vítor Anes to help me test ANSYS simulations and Matlab program. I want to thank to my family for all the support given during this work too.

Abstract

Magnesium and its alloys are becoming more and more used in the aerospace and automobile industry because of its low weight. The technology has suffered many improvements allowing magnesium alloys to have a mechanical performance close to aluminum alloys and corrosion protection. This allows many possible applications for magnesium alloys subjected to multiaxial fatigue.

The objective of this work is to perform multiaxial fatigue simulations in ANSYS and in a Plasticity program using Jiang & Sehitoglu plasticity model adapted for nonproportional effects of an AZ31 magnesium alloy. The damage parameters of Findley, Brown & Miller, Smith-Watson-Topper, Fatemi & Socie, Liu I and Liu II are applied.

The life cycles number results show that all the damage parameters don't take into account how much time the multiaxial loading is above the yield value. New damage parameters which take account this effect are presented. The results shown during ANSYS and Plasticity program simulations that for the same cases the work done not considering nonproportional effects (ANSYS) is greater than considering them. However other cases show the opposite.

KEY-WORDS

Multiaxial Fatigue

Magnesium

Numerical Simulations

Plasticity

Fatigue Life

Resumo

O magnésio e as suas ligas estão a tornar-se cada vez mais usadas nas indústrias automóvel e aeroespacial devido à sua baixa densidade. A tecnologia sofreu grande evolução permitindo às ligas de magnésio terem uma performance mecânica e protecção contra a corrosão próximas das ligas de alumínio. Tal poderá permitir variadas aplicações de ligas de magnésio sujeitas a fadiga multiaxial.

O objectivo deste trabalho consiste em obter simulações de fadiga multiaxial em ANSYS e num programa de plasticidade que usa o modelo de plasticidade de Jiang & Sehitoglu adaptado a efeitos não proporcionais de uma liga de magnésio AZ31. Os parâmetros de dano de Findley, Brown & Miller, Smith-Watson-Topper, Fatemi & Socie, Liu I e Liu II são aplicados.

Os resultados do número de ciclos de vida mostram que os parâmetros de dano não têm em conta quanto tempo o carregamento multiaxial está acima do valor da cedência. Novos parâmetros de dano a ter em conta este efeito são apresentados. Os resultados mostrados durante as simulações de ANSYS e do programa Plasticity mostram que, para alguns casos, o trabalho realizado, não considerando efeitos não proporcionais (ANSYS), é maior do que considerando estes. No entanto, noutros casos observa-se o oposto.

Palavras-Chave

Fadiga Multiaxial

Magnésio

Simulações Numéricas

Plasticidade

Vida à Fadiga

Index

Figures Index

Tables Index

Nomenclature

Acronyms

AISI	American Iron and Steel Institute
ASME	American Society of Mechanical Engineers
ASTM	American Society for Testing and Materials
EADS	European Aeronautic Defence and Space Company
HCF	High Cycle Fatigue
LCF	Low Cycle Fatigue
MCC	Minimum Circumscribed Circle
MCE	Minimum Circumscribed Ellipse
SWT	Smith, Watson & Topper
SAE	Society of Automotive Engineers
USAMP	United States Automotive Materials Partnership

Symbols

γ^p	Plastic Shear Strain
$\Delta\gamma$	Shear Strain Range
γ_f'	Torsional Fatigue Ductility Coefficient
ε	Strain
ε^e	Elastic Strain
ε^p	Plastic Strain
ε_n	Normal Strain to a Plane
ε_f'	Fatigue Ductility Coefficient
$\Delta\varepsilon_n$	Normal Strain Range to a Plane
$\varepsilon_{nominal}$	Nominal or Engineering Strain
ε_{real}	Real Strain
θ	Principal Stresses Plane Angle
K'	Cyclic Strength Coefficient
K_{np}'	Nonproportional Cyclic Strength Coefficient
υ	Poisson Coefficient
σ	Stress
σ_{yield}	Yield Stress
σ_X	Stress along X axis
σ_Y	Stress along Y axis
σ_Z	Stress along Z axis
σ_n	Normal Stress to a Plane

σ_a	Alternating Stress
σ_{max}	Maximum Stress
σ_f'	Fatigue Strength Coefficient
$\sigma_{n,max}$	Maximum Normal Stress to a Plane
$\sigma_{a,R=-1}$	Alternating Stress for Completely Reversed Cycling
σ_{real}	Real Stress
$\sigma_{nominal}$	Nominal or Engineering Stress
σ_1	First Principal Normal Stress
σ_2	Second Principal Normal Stress
σ_3	Third Principal Normal Stress
$\Delta\sigma_n$	Normal Stress Range to a Plane
$\sigma_{von\ Mises}$	von Mises Stress
τ	Shear Stress
τ_{XY}	Shear Stress in XY plane
τ_{YZ}	Shear Stress in XY plane
τ_{XZ}	Shear Stress in XY plane
$\Delta\tau$	Shear Stress Range
τ_a	Alternating Shear Stress
$\tau_f{}'$	Torsional Fatigue Strength Coefficient
$\tau_{a,R=-1}$	Alternating Shear Stress for Completely Reversed Cycling
b	Fatigue Strength Exponent
$b\gamma$	Torsional Fatigue Strength Exponent
c	Fatigue Ductility Exponent
$c\gamma$	Torsional Fatigue Ductility Exponent
D	Total Cyclic Energy
E	Young Modulus
F	Kanazawa Nonproportional Factor
G	Shear Modulus
n'	Cyclic Strain Hardening Exponent
N_f	Life Cycles Number
t	Time
V	Traversed Angles Velocity
Y_F	Yield Function

In the case of specific symbols the designation can be found in the text where it is referred.

1 Introduction

Nowadays the demand for low fuel consumption led to the continuous search of low density materials. In this context magnesium and its alloys are of great interest because magnesium and its alloys have the lowest density of all metallic constructional materials. They have other advantages too [1]:

1. high specific strength;
2. good castability, suitable for high pressure die-casting;
3. can be turned/milled at high speed;
4. good weldability under controlled atmosphere;
5. much improved corrosion resistance using high purity magnesium;
6. readily available;
7. compared with polymeric materials:
    a) better mechanical properties;
    b) resistant to ageing;
    c) better electrical and thermal conductivity;
    d) recyclable.

Because of these advantages magnesium and its alloys were used in the World War I and World War II extensively. However magnesium and its alloys have not become widely used because of their disadvantages [1]:

1. low elastic modulus;
2. limited cold workability and toughness;
3. limited high strength and creep resistance at elevated temperatures;
4. high degree of shrinkage on solidification;
5. high chemical reactivity;
6. in some applications limited corrosion resistance.

To make magnesium alloys more competitive in the market, research work is being done to overcome some of the disadvantages pointed above. Nowadays the magnesium alloys are reaching a mechanical performance similar to that of aluminum alloys, the major opponent in automobile and aerospace applications. To illustrate that, a mechanical performance comparison between magnesium and aluminum alloys is presented in figure 1.1. To measure the mechanical performance a coefficient Q_{OS} is used. The higher the coefficient, the higher mechanical performance of the material. As it can be observed in figure 1.1, magnesium alloys are reaching a mechanical performance coefficient value approximate of the aluminum alloys. However as it can be observed in table 1.1, limitations continue to exist due to limits in the yield strength (R_p) and strain energy density (W) relative to aluminum alloys.

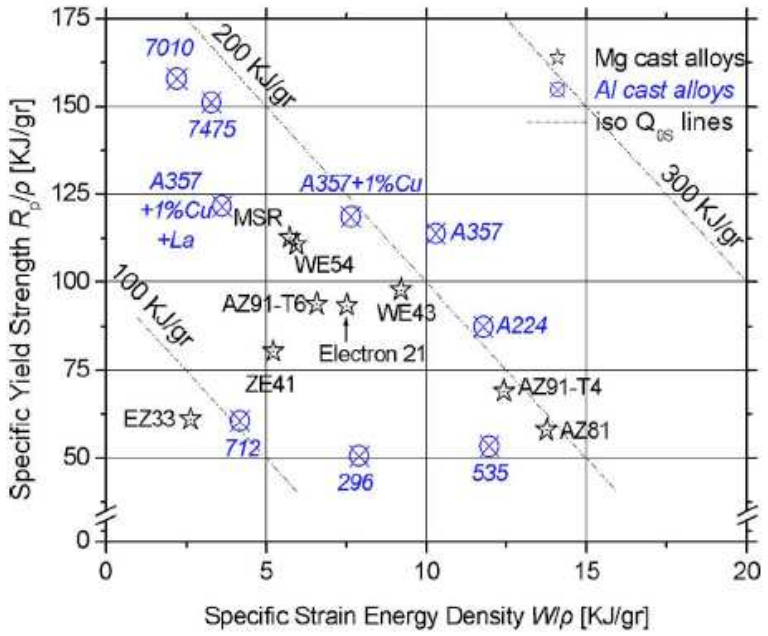

Figure 1.1 – Mechanical performance of aluminum and magnesium alloys [2]

	Alloys	Alloy series	ρ (kg/m^3)	R_p (MPa)	W (MJ/m^3)	Q_{0S} (MPa)
Al alloys	A224	Al–Cu	2.70	236	31.8	205.2
	296	Al–Cu–Si	2.79	141	22.1	129.5
	A357	Al–Si–Mg	2.68	305	27.6	216.8
	A357+1% Cu	Al–Si–Mg	2.69	319	20.5	195.0
	A357+1% Cu+La	Al–Si–Mg	2.69	327	9.7	157.7
	535	Al–Mg	2.62	140	31.3	173.1
	7010	Al–Zn	2.83	447	6.2	180.0
	712	Al–Zn	2.81	170	11.7	102.2
	7475	Al–Zn	2.80	423	9.2	183.9
Mg alloys	ZE41-T5	Mg–Zn–RE	1.84	148	9.6	132.6
	WE43-T6	Mg–Y–RE	1.84	180	16.9	189.9
	EZ33-T5	Mg–RE–Zn	1.80	110	4.7	87.4
	MSR-T6	Mg–Ag–RE	1.82	205	10.4	170.0
	AZ81-T4	Mg–Al–Zn	1.81	105	24.9	195.5
	AZ91E-T4	Mg–Al–Zn	1.81	125	22.5	193.3
	AZ91E-T6	Mg–Al–Zn	1.81	170	11.9	159.6
	Electron 21	Mg–Zn–Ne	1.82	170	13.7	168.6
	WE54-T6	Mg–Y–RE	1.85	205	11.0	170.2

Table 1.1 – Mechanical properties of magnesium and aluminum alloys [2]

Alenia, Eurocopter and Airbus with the EADS (European Aeronautic Defence and Space Company) Research Centers defined the requirements for new magnesium alloys to be applied within interior and systems or secondary structural aeronautic applications [3]. These data are presented in table 1.2. Note that some magnesium alloys of table 1.1 have yield strength value between 200 to 310 MPa, the interval mentioned in table 1.2 for systems application.

Property	Temperature	Requirements of new Mg alloys for	
		systems application	structural application
Tensile Ultimate Strength	RT	275-350 MPa	450 MPa
Tensile Yield Strength	RT	200-300 MPa	350 MPa
Elongation to fracture	RT	12-16 %	16-18 %
Yield Strength	150°C	- 10% of YTS	-10% of YTS
Compressive Yield Strength	RT	± 10% of YTS	± 10% of YTS
Failure under compression	RT	comparable Al 5083	comparable Al 2024 T3
Specific Weight	RT	1,75	1,75
Residual Strength	RT	n.a.	comparable to 2024 T3
Fatigue Crack Growth	RT	n.a.	comparable to 2024 T3
Fatigue limit (K_t=1.0, R=0.1)	RT	160 MPa	140 MPa

Table 1.2 – Requirements of magnesium alloys for aeronautic applications [3]

They summarize the most promising magnesium alloys for aeronautic applications in figure 1.2 and compare with commonly used aluminum alloys. The magnesium alloys were selected due to corrosion behavior, environmental friendliness and mechanical performance.

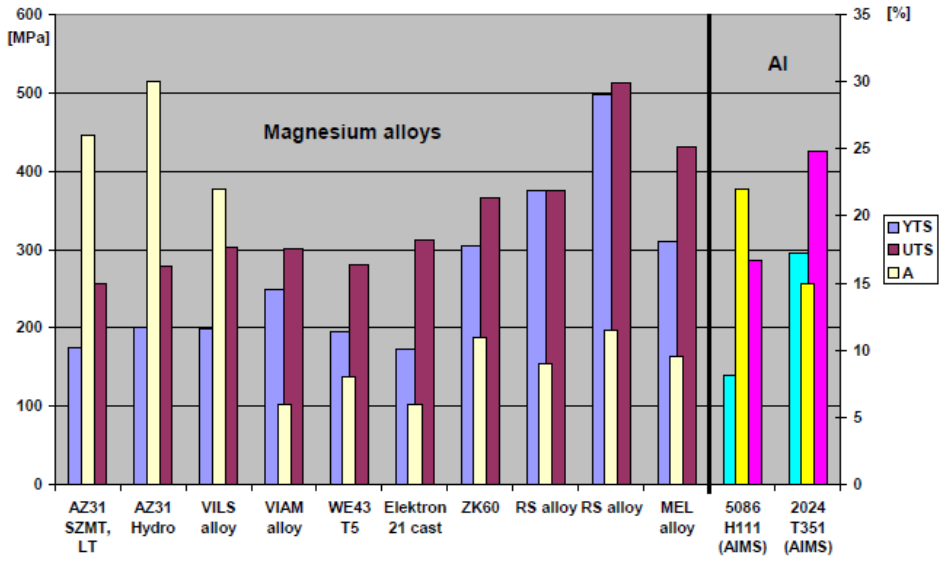

Figure 1.2 – Comparison between magnesium and aluminum alloys in terms of tensile yield strength (YTS), tensile ultimate strength (UTS) and elongation to fracture (A) [3]

Another important development of magnesium alloys is in corrosion resistance. This was the main reason for magnesium use restriction in the past [4] on the aerospace industry. The major concerns of magnesium corrosion protection are firstly with galvanic corrosion and secondly with general corrosion. In terms of general corrosion, the current magnesium and aluminum alloys are compared in figure 1.3. As it can be observed there are some magnesium alloys that have similar corrosion rates to the aluminum alloys.

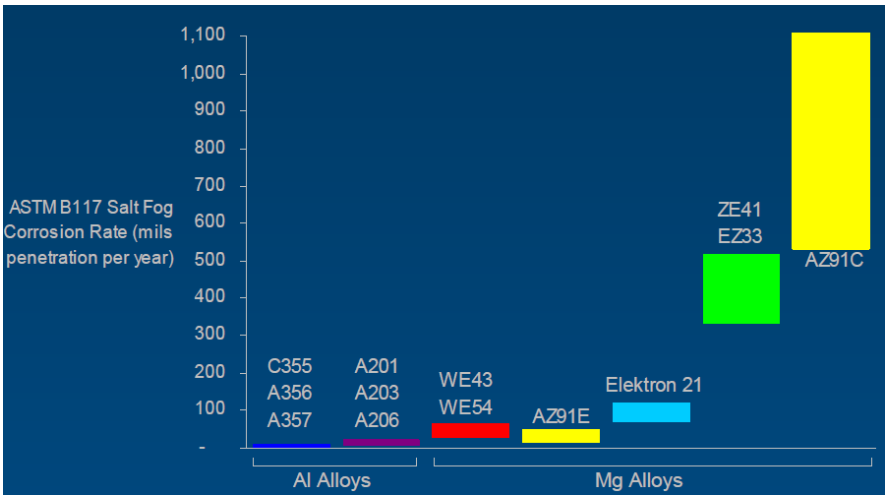

Figure 1.3 – Corrosion rate of ASTMB117 salt fog test for magnesium and aluminum alloys [5]

Galvanic corrosion, as it is said, is the primary concern in terms of corrosion. Galvanic corrosion [6] happens when two different metals are electrically connected and there is an electrochemical potential difference between them. So that the metals can have an electrical connection, an electrolyte is needed, so that ions can flow from the anode to the cathode, i. e., the anode and cathode have to be immersed in the electrolyte. Note that water or moisture can be that electrolyte. This process leads to the anodic metal corrosion with the corrosion of the cathode metal being retarded. In table 1.3 it is presented the galvanic series of metals to compare the potential corrosion of two metals in the presence of each other.

Anodic - Least Noble	Manganese Bronze , Tin Bronze
Magnesium	Nickel Silver
Magnesium Alloys	Copper - Nickel Alloy 90-10
Zinc	Copper - Nickel Alloy 80-20
Cadmium	Stainless Steel 431
Aluminum	Nickel, Aluminum, Bronze
Mild Steel , Wrought Iron	Monel
Cast Iron, Low Alloy High Strength Steel	Silver Solder
Chrome Iron (active)	Nickel (passive)
Stainless Steel, 431 Series (active)	60 Ni- 15 Cr (passive)
Stainless Steel 312, 313, 332, 357, 410,416, (Active)	Inconel 600 (passive)
Ni - Resist	80 Ni- 20 Cr (passive)
Stainless Steel 326, 328, (Active)	Chrome Iron (passive)
Aluminum Bronze	Stainless Steel 312, 313, 314, 332, 357,(PASSIVE)
Hastelloy C (active) Inconel 625 (active)	Stainless Steel 326, 328,(PASSIVE)
Titanium (active)	Incoloy 825nickel - Molybdeum - Chromium
Lead - Tin Solders	Iron Alloy (passive)
Lead	Silver
Tin	Titanium (pass.) Hastelloy C (passive)
Inconel 600 (active)	Inconel 625(pass.)
Nickel (active)	Graphite
Hastelloy B (active)	Zirconium
Brasses	Gold
Copper	Platinum
Manganese Bronze , Tin Bronze	**Cathodic Most Noble.**

Table 1.3 – Galvanic series of metals [7]

The galvanic series lists the metals in order of their electrical potential relative to a recognized standard, that can be, for example, seawater electrolyte. Metals that are farther away from each other in the list of table 1.3 will cause more anodic metal corrosion in the presence of an electrolyte. Note that magnesium and its alloys are at the top of the list, being the most anodic metals. There are several ways to solve this problem. Two methods are referred here. One is to design in a manner to minimize galvanic corrosion. In figure 1.4 it can be seen that the improper location of a bolt can result in galvanic corrosion. In figure 1.5 it can be seen that this can happen in real helicopter component.

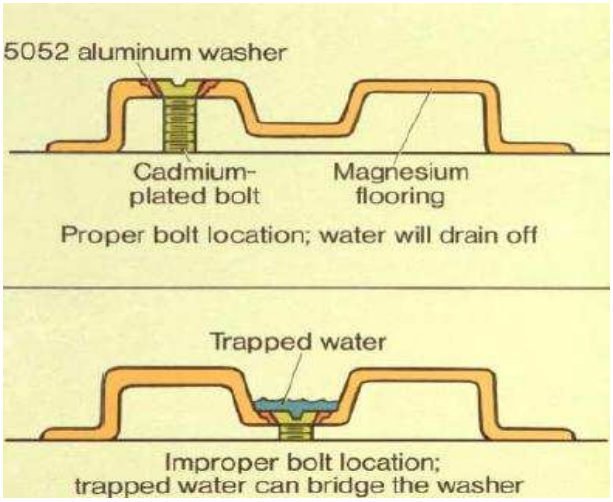

Figure 1.4 – Two possible bolt locations [5]

Figure 1.5 – Water trap in a helicopter tail rotor [5]

Another method consists of applying a coating protection for magnesium alloy surface. Examples of that are Tagnite coating, the most corrosive and abrasive resistant anodic coating for magnesium alloys [8], Magoxid coating and Keronite coating [9].

Along with these developments, several development studies produce technologies to help magnesium alloys to become more used in the industry:

- MagForming – a project to develop new magnesium forming technologies for the aeronautics industry [10];
- MagForge – a project to develop forged components for structural lightweight transport applications [11];
- The United States Materials Automotive Partnership´s (USAMP) Structural Cast Magnesium Development Project – this project ended with the successful development and production of prototype magnesium engine cradles. General Motors put a similar magnesium engine cradle into production for the 2006 Corvette Z06 [12];
- More projects can be found in *http://www.ist-world.org/default.aspx* searching for magnesium in the projects section.

There are some internet websites that have news information about magnesium alloys: *http://www.intlmag.org/index.cfm* International Mg Association, *http://www.magnesium.com/w3/* Magnesium.com and Efunda website [13] for magnesium alloys mechanical properties.

To understand what development studies are needed for magnesium alloys to become more used in the industry, the report Magnesium Vision 2020 [14] is a reference. In this report it is mentioned that performing life-cycle analyses or fatigue analyses of magnesium alloys is a major research need to reduce cost/ quality challenge. In the next paragraph the fatigue concept is explained. The intuitive idea presented is based on reference [15].

The components of transports, machines and structures are often subjected to repeated loads. The loadings can cause microscopic physical damage to the materials involved which can accumulate with continued cyclic loads in spite of stresses well lesser than material ultimate strength. The damage accumulation with continued cyclic loads can result in a crack or other macroscopic damage that leads to failure of the component. This process of damage and failure due to cyclic loading is called fatigue. The technical definition of fatigue by the American Society for Testing and Materials (ASTM) is “the process of progressive localized permanent structural change occurring in a material subjected to conditions which produce fluctuating stresses and strains at some point or points and which may culminate in cracks or complete fracture after a sufficient number of fluctuations”. Fatigue study is very important because it is estimated [16] that 50 to 90 % of all mechanical failures are caused by fatigue phenomenon. Fatigue can have different causes which can happen simultaneously. The different fatigue causes have originated different fatigue areas. Examples of them are time-varying loading fatigue, thermal fatigue, corrosion fatigue, surface/contact fatigue and combined creep & fatigue. The time-varying loading fatigue is divided in two areas dependent on the number of loading cycles of the component until failure. Typically if the cycles number is $> 10^2\ to\ 10^4$, fatigue is called high cycle fatigue (HCF); however the HCF begins in a number range that changes with the material. The other area is the low cycle fatigue (LCF) and it happens for a number of cycles below of HCF.

Nowadays there are 3 major methodologies to study fatigue [15]. They are stress-based approach, strain-based approach and fracture mechanics based approach. The stress-based approach is based on the average stresses which affect a region of a component. The strain-based approach is based on a detailed analysis of the localized yielding. The approach of fracture mechanics studies the growing of the cracks with the help of fracture mechanics methods.

There are several fatigue design philosophies [13]:

- Infinite-life design – considers that all stresses are enough below to ensure an “infinite” service life;
- Safe-life design – expects and allows that cracks occur during service but never grow to critical length during the service life;
- Fail-safe design – expects and allows that cracks occur during service but never result in failure before the scheduled maintenance;
- Damage-tolerant design – based in fracture mechanics; counts initial imperfections; is more accurate than the other philosophies.

Fatigue problems can have a uniaxial or multiaxial loading. In the case of uniaxial loading there is consensus in which theory has to be applied depending on the context to give accurate determination to the fatigue life. However in multiaxial loading case there is no consensus about what is the best theory to determine fatigue life. This problem will be better explained in the next chapters.

1.1 Applications

There are several applications for magnesium alloys and multiaxial fatigue. Focus is made here in aircraft and automobile applications. In figure 1.6, some aerospace applications of magnesium and magnesium alloys can be observed. In figure 1.6 a) it is the airplane TU-135 (43100 Kg). The red zones represent the location of magnesium components (780 Kg). Figure 1.6 b) shows a utility aircraft gearbox, the figure 1.6 c) shows a service door inner panel and the figure 1.6 d) an experimental F-80-C aircraft of complete magnesium construction.

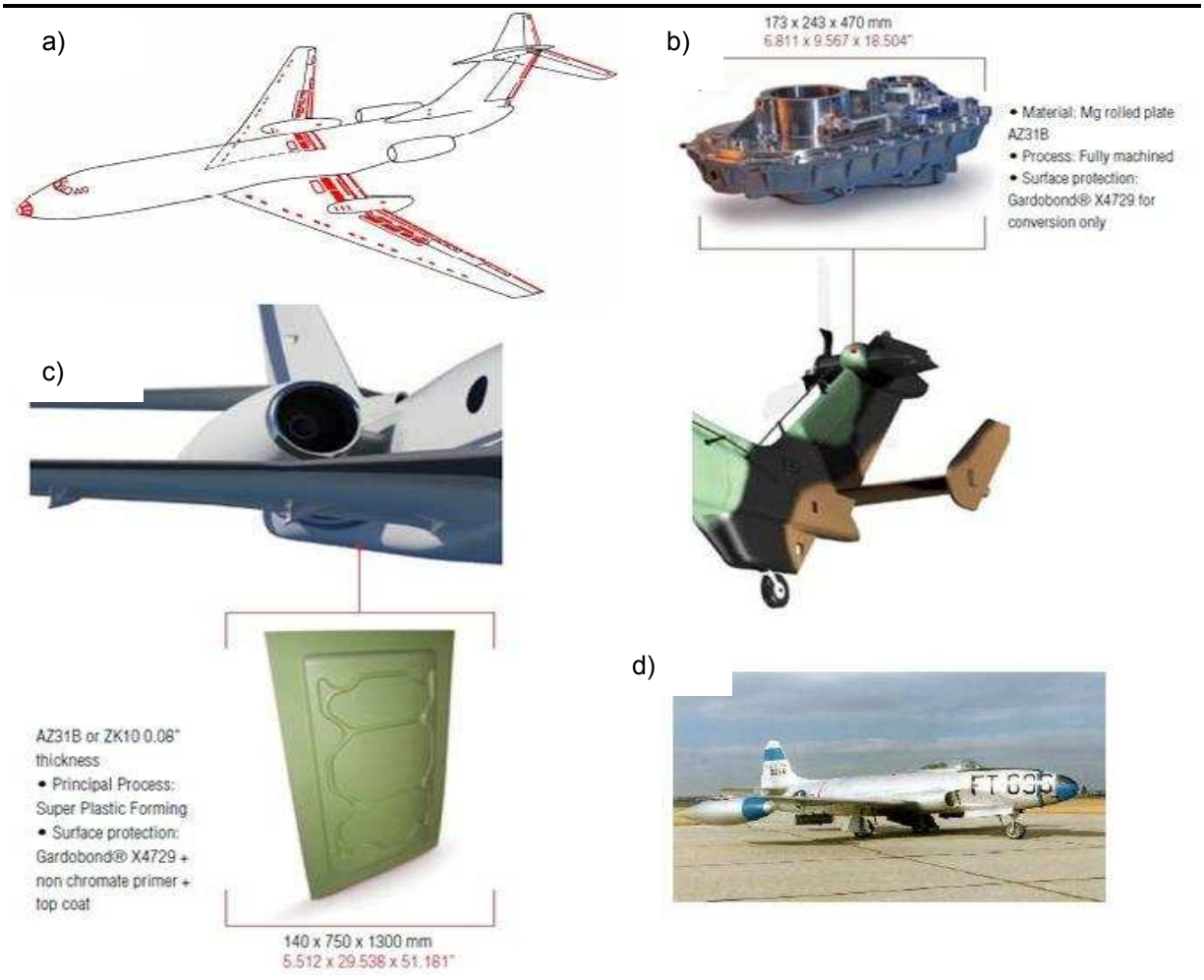

Figure 1.6 – Magnesium alloys in aerospace applications; a) Mg components in the TU-135 [4]; b) utility aircraft gearbox [17]; c) service door inner panel [17]; d) experimental modification of the Lockheed F-80-C [4]

In figure 1.7 automobile applications for magnesium alloys are presented. Figure 1.7 a) represents possible locations to use magnesium alloys in a car. Figure 1.7 b) shows the magnesium wheel of the Porsche Carrera GT. There are various magnesium alloys that are used to forge wheels, e. g., ZK60, AZ31 or AZ91. Figure 1.7 c) shows a door inner component made from a magnesium single sheet of the alloy AZ31B-O.

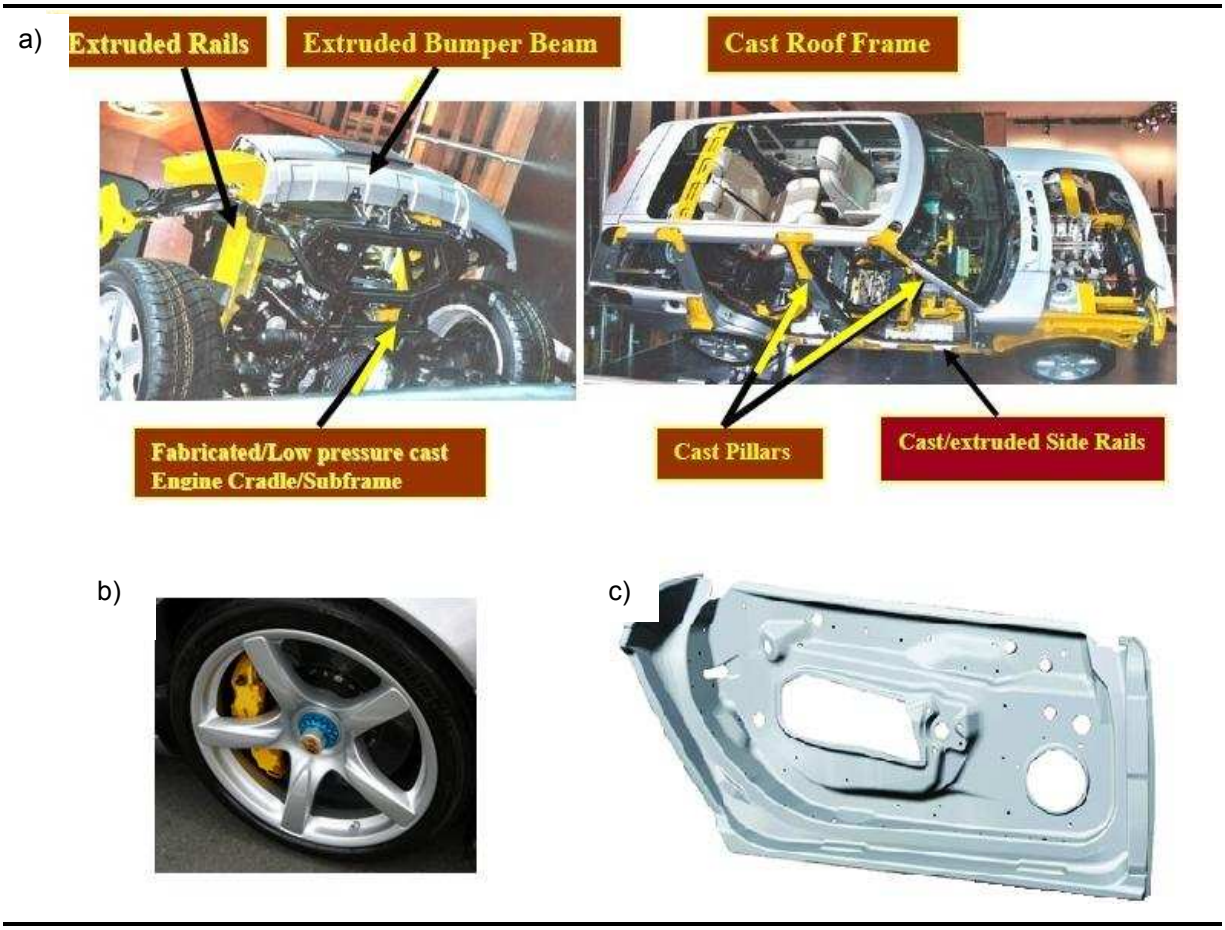

Figure 1.7 – Magnesium alloys automotive applications; a) applications in automobile structure [14]; b) wheel of a Porsche Carrera GT [18]; c) door inner component [19]

Magnesium has other areas of applications too [19]. The Sony Mini-Disc Walkmans MZ-R90 and MZ-E80 (launched in 1999) were manufactured by press forging the magnesium wrought alloy AZ31. Magnesium alloys AZ80, AZ61 and AZM are used in extruded bar form to make anti tank ammunition rounds. Magnesium wrought alloys AZ31, AZM and AZ61 are used in the construction of satellite components.

As it can be seen in figure 1.7 magnesium alloys have many applications. To extend its applications range and build lighter objects and vehicles it is important to understand its behavior in multiaxial fatigue. Two applications of multiaxial fatigue are presented next.

In figure 1.8 an example of multiaxial fatigue acting in the wing of an aircraft is illustrated. It is placed a strain gauge in a wing, see figures 1.8 a) to c), to measure the loading stresses. Using the convention of fig. d), the stresses measurements e) were obtained. As it can be seen the wing is subjected at least to shear stresses and stresses along X-axis, so a multiaxial loading is observed. This multiaxial loading changes with the time causing multiaxial fatigue.

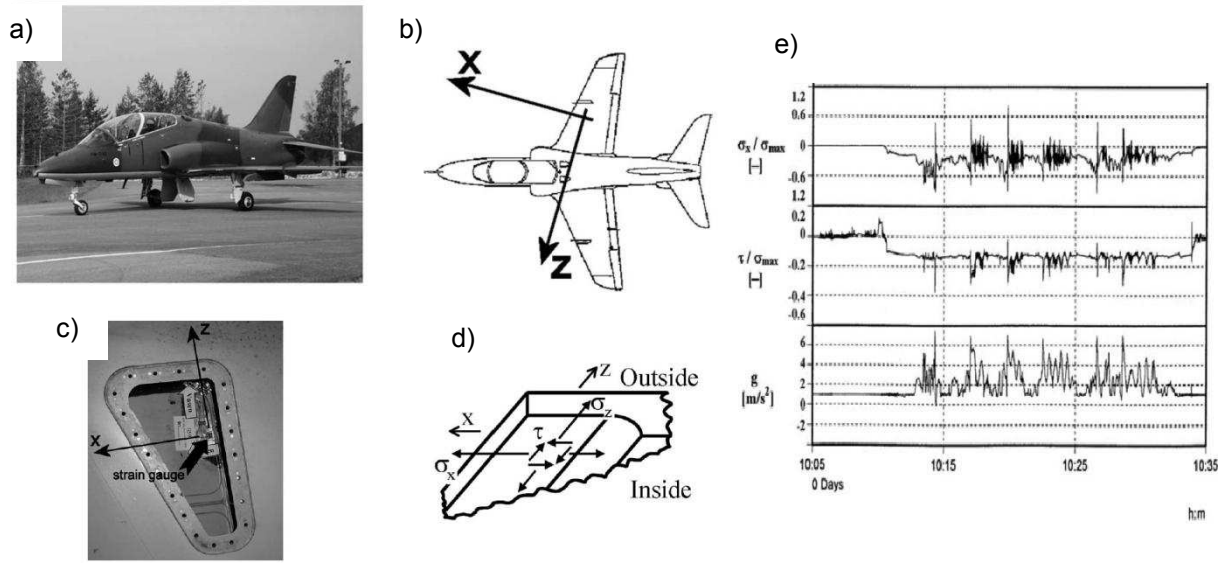

Figure 1.8 – Multiaxial fatigue on a wing; a) British Aerospace Hawk Mk.51; b) & c) location of strain gauge; d) stress components near strain gauge location; e) stresses obtained in flight measurements [20]

In figures 1.9 a) and b) a finite element modeling of a railroad wheel can be observed. The stresses presented in fig. 1.9 c) are at a point 3 mm below tread surface. The wheel is subjected to shear stresses in the YZ plane and stresses along Y axis, so a multiaxial loading is observed. This multiaxial loading changes with the time causing multiaxial fatigue.

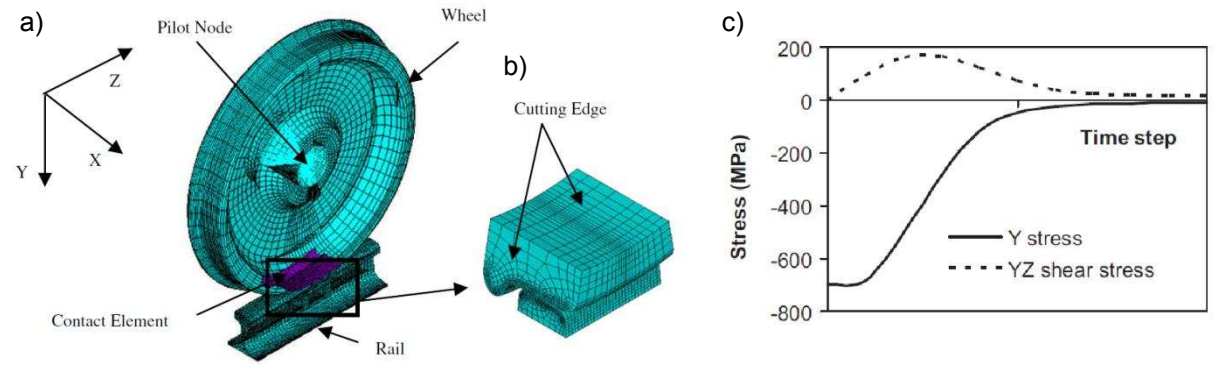

Figure 1.9 – Multiaxial fatigue on railroad wheels; a) full model of finite element modeling of wheel/rail contact; b) sub model; c) stress history [21]

1.2 Objectives

The main objective of this work is to perform a multiaxial fatigue analysis of a magnesium alloy. As it can be noted in the text above, the alloy AZ31 has many applications. Because of that the magnesium alloy AZ31B-F is chosen. To achieve this objective there are various tasks that have to be done:

1. Study the multiaxial fatigue theory and understand its physical basis;
2. Determine fatigue damage criteria;
3. Do multiaxial loading simulations using ANSYS and a C++ programmed plasticity model;
4. Determine the fatigue life based on the stress states simulated applying different damage criteria;
5. Perform a tension test to the AZ31B-F alloy;
6. Find possible applications of multiaxial fatigue in aerospace and automobile industries.

2 Multiaxial Fatigue Bibliographical Revision

Fatigue studies started in XIX century. The continuous studies led to the technologies presented in this chapter. In figure 2.1 it can be seen that the study of fatigue involves studies in different size scales. The objective of the engineer is to construct structures based on specimen experiments. The theories that are used to extrapolate the results of the specimens to the structures have to be in accordance with the observed phenomena at size scales of crystals, dislocations and atoms.

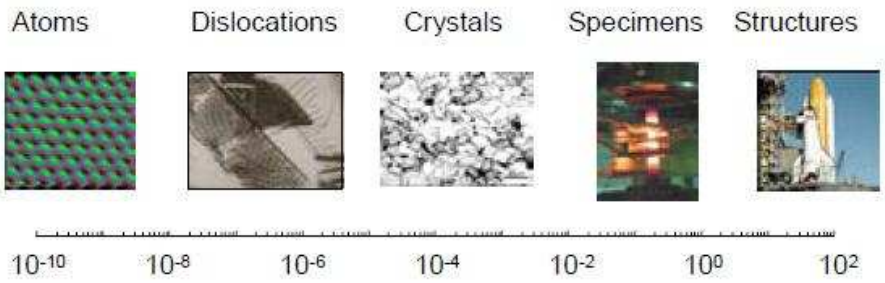

Figure 2.1 – Size scale for studying fatigue [22]

2.1 Fatigue History & Recent Works

Fatigue history is presented here by a chronological date. The history presented is based on references [16] and [23] to [26]. Focus is made in multiaxial fatigue and general fatigue advancements.

1837 – Albert, a German mining administrator, published the first fatigue test results. To do the tests he constructed a test machine for the conveyor chains which had failed in service at the Clausthal mines.

1842 and next years – In this period many disastrous railroad accidents happened due to fatigue, e. g., on 5th October 1842, a locomotive axle broke at Versailles killing 60 people.

1854 – Braithwaite, an Englishman, used by the first time the term “fatigue” in his published papers where he describes many service fatigue failures of brewery equipment, water pumps, propeller shafts, crankshafts, railway axles, levers, cranes, etc.

1858 to 1870 – Whöler, a German engineer, measured service loads of railway axles with self developed deflection gages at 1858 and 1860. In 1860 Whöler published the results of fatigue tests with railway axles. In 1870 he presented a final report concluding: “material can be induced to fail by many repetitions of stresses, all of which are lower than the static strength. The stress amplitudes are decisive for the destruction of the cohesion of the material. The maximum stress is of influence only in so far as higher it is, the lower are the stress amplitudes which lead to failure”. According to Whöler, the stresses amplitudes are the most important parameter for fatigue life, but a mean stress also has a

significant influence. Whöler represented his test results in form of tables but never plotted them, i. e., the stress vs life cycles number or S-N curve. His successor Spangenberg will have done it.

1881 – Bauschinger, a German engineer, named the Bauschinger effect. This effect is “the change of the elastic limit by often repeated stress cycles” by author’s words.

1903 – Ewing and Humfrey, from England, observed the slip bands on the surface of rotating bending specimens. This was probably the first metallurgical description of the fatigue process.

1918 – The first full-scale fatigue test with a large aircraft component was carried out at the Royal Aircraft Establishment in the U.K. and the analysis was published: “Methods employed at the Royal Aircraft Establishment for the experimental determination of the ultimate strength of aeroplane structures”.

1910 – Basquin, an American, represented the type of Whöler data table in the form $log(\sigma_a)$ on the ordinate and $log(N)$ on the abscissa. He describes the plotted data by the formula:

$$\sigma_a = CN^n$$

which is still used nowadays. In a large table Basquin presented values for C and n based on Whöler data.

1917 – Haigh, an Englishman, mentioned by the first time the term corrosion fatigue.

1920 – Griffith, a Welshman, working in the Royal Aircraft Establishment in the U.K., developed the basis of fracture mechanics. He showed by tests on the brittle material glass that small cracks like scratches considerably reduced the breaking strength and that the crack size also had an influence. He described this process by a formula.

1921 – Mason did a study of cyclic deformations in combined bending and torsion tests with a steel material. The first work considering the out of phase angle between loadings appears this year due to Mason and Delaney.

1941 to 1945 – Gassner, a German, established the topic of operational fatigue strength. This is described by several steps: dimensioning (sizing) of a component for finite, but sufficient fatigue life under variable loads. That is accomplished following the steps:

1. measuring the service stresses in the form of a stress spectrum employing the correct counting method, also counting the number of cycles per flying hr, Km, etc;
2. determining the corresponding forces or moments for obtaining generally valid load assumptions for similar components;
3. extrapolating the always too short measured spectrum to the one to be expected in service;

4. selecting a suitable return period containing rare high stress cycles in order to include their nonlinear damaging effects;
5. if it is possible, standardizing the shape of the spectrum, for example, specific spectra for civil aircraft, military aircraft and automobile components, respectively;
6. simulating the service spectrum by a blocked variable-amplitude test (program test) and – after this it is possible with suitable test machines – by a random fatigue test with the component;
7. plotting the results in the form of "Gassner" – curves with the maximum amplitude of the spectrum on the ordinate and the total number of cycles on the abscissa, both to a logarithmic scale;
8. considering the scatter of fatigue lives by a safety factor, calculated on a statistical basis, to obtain the necessary probability of survival. Its numerical value depends on the component in question, i. e., an automobile component has to have a high probability of survival and a ship component a low one.

1934 to 1951 – Gough et al. did a study of fatigue for combined bending and torsion in phase loadings. They concluded that the known yield criteria when applied to fatigue were impropriate to describe the obtained results.

1944 – Zapffe introduced the term fractography. The objective of fractography is to analyze the fracture features and relate the material crack surface topography with the mechanisms and causes of fracture. The fractography enables the study of crack origins and the direction of its propagation.

1954 – Manson & Coffin presented the linear equation in log-log coordinates for the plastic deformation versus fatigue life.

1955 – Sines published a report in which he reviews experimental data available in alternated biaxial loadings and combined static and alternated stresses. He concluded that for brittle material, in spite of yield occurring near maximum theoretical normal stress, the failure could not be caused by normal stresses; the shear cyclic stress appears to be the fatigue failure cause. Because of the last statement Sines analyzed the static stresses influence in geometric planes where cyclic shear stresses are bigger.

1956 – Findley reviewed many experimental works in fatigue. He concluded that none previous result is in contradiction with a shear stress limit. He investigated the Aluminum alloy 7075-T6 fatigue behavior subjected to combined bending and torsion. All the loadings were in-phase. Findley extended some yield known criteria to fatigue analysis. Trying to determine a better criterion for multiaxial fatigue analysis, he observed in the plane of maximum shear stress amplitude the influence of normal tension.

1968 – Elber observed that after a high traction load the crack closed before the load return to zero. Today this phenomenon is known as crack closure.

1969 to 1974 – The American Society of Mechanical Engineers (ASME) debated about applying Tresca criterion to the project of pressurized reservoirs involving multiaxial fatigue. Because of its simplicity, conservatism and flexibility, Tresca criterion gained advantage to von Mises criterion. In 1974 it was chosen to estimate multiaxial fatigue life based on a procedure code.

1970 – Smith, Watson and Topper (SWT) presented a fatigue damage parameter for materials that generally fail in mode I. In this mode crack nucleates in shear directions and fatigue life is controlled by the crack growth in perpendicular planes to maximum principal stress and maximum principal strain.

1972 – McDiamird reviewed the available experimental data in multiaxial HCF and presented a new damage parameter based on stresses. This new damage parameter was in accordance with the available results up to date.

1967 to 1973 – Brown and Miller presented a new theory for multiaxial fatigue based on a physical understanding of the crack growth causes. The new theory suggested that the multiaxial fatigue failure could be described by a relation between the maximum shear deformation range and the normal deformation range that occur in the plane of maximum shear deformation range. They classified shear cracks in Case A and Case B. They concluded in their work that there was a lack of more experimental results related to anisotropy, average deformation, out of phase loadings and temperature effects.

1974 – At the United States Air Force, the concept damage tolerance was introduced. This means that is assumed that mechanical components can have defects (cracks) in the materials, present in critical points of the components. Supervision is made to guarantee the safety of the component.

1975 – Grubisic and Simbüler by studying multiaxial fatigue concluded that the phase angle between shear stresses and normal stresses can have a high impact in fatigue life.

1977 – Kanazawa et al. studied LCF considering phase angle in multiaxial loadings. Steel 1% CrMoV specimens were subjected to combined torsion and axial loadings. They concluded that fatigue cracks initiate in the planes of maximum shear stresses subjected to all loading conditions and that fluctuations around this plane can be found in some cases; Tresca criterion and von Mises are not conservative under out of phase cyclic loadings; the multiaxial combined tension and torsion out of phase loadings produce more damage than the in phase loadings, specifically the 90º out of phase loading.

1976 – Blass and Zamrik studied multiaxial fatigue of AISI (American Iron and Steel Institute) 314 steel subjected to combined tension and torsion and combined compression and torsion loadings and concluded that the concept of equivalent deformation amplitude (ASME) doesn't apply to several results of multiaxial fatigue.

1981 – Garud proposed a new form to approach the multiaxial fatigue analysis. Garud presented a failure criterion to multiaxial fatigue based on an energetic model. He suggested applying the concept of uniaxial cyclic hysteresis energy (of Morrow) to multiaxial fatigue. Naturally plastic work per cycle is the fatigue life (crack nucleation) parameter. The calculations were made with the help of a plasticity model. The author obtained good correlations for proportional and nonproportional loadings applied to a 1 % CrMoV steel. After this work Garud concluded that traction work causes more damage than shear work. Because of that he applied a weight factor to the term representing shear work. This model however is not suitable for HCF because the work per cycle is very small and so it is very difficult to calculate accurately.

1988 – Fatemi and Socie presented a multiaxial fatigue damage parameter based on Brown and Miller work. They replaced the normal deformation term by normal stresses. The physical justification is that normal stresses make the surfaces of the crack to deviate, reducing the friction forces. Accounting the stresses instead of deformations makes the damage parameter calculus more suitable.

1989 – Dang Van developed a multiaxial fatigue failure criterion in a mesoscopic scale. The criterion is based on a critical volume where stresses are analyzed at a mesoscopic scale. Dang Van suggested that crack begins in the grains that suffer plastic deformation and form the slip bands (fatigue is a local phenomenon). He concluded that at mesoscopic scale shear stresses and hydrostatic stresses are relevant variables.

1993 – Liu and Zenner presented a criterion based on a double integral. Reviewing the previous works they concluded that there were two ways to formulate a multiaxial fatigue damage parameter, i. e., by an integral formulation or by a critical plane formulation. The advantage of integral formulation is that damage is calculated at all planes of a critical volume. The critical plane formulation only considers the plane where the damage parameter is maximum.

1995 to 1997 – Papadopoulos presented a microscopic integration model in 1995. In 1997 he presented the critical plane model named the Minimum Circumscribed Circle (MCC) to estimate the shear stress amplitude.

1997 – Palin-Luc and Morel working in multiaxial fatigue concluded that for HCF a model based on a critical plane is not enough to explain all the experimental observations. Because of that they proposed a model based on the analysis of the volume around a critical point (that influences crack propagation initiation). The damage parameter is calculated per cycle and it is the energy density of volumetric elastic deformation that exceeds a limit value. This limit value depends on the material and it is based on a new fatigue limit which is less than the considered normal fatigue limit. This is because (according to the authors) conventional considered fatigue limit is not a limit to damage initiation, but a limit of not propagation of damage. The presented model is based on Papadopoulos mesoscopic criterion. There are problems with the determination of the volume because it is needed a good computational equipment and the model was still in development.

2000 – Freitas, Li and Santos proposed a new damage parameter based on the MCC of Papadopoulos. They proposed the Minimum Circumscribed Ellipse (MCE) parameter to take into account the nonproportional loading effects that are not considered in the MCC model.

2003 – Reis, Li and Freitas studied the effects of nonproportional loadings in the steel 42CrMo4. The conclusions changed the ASME code.

2004 – Reis, in his PhD thesis, [16] studying steels behaviors subjected to axial-torsion nonproportional and proportional loadings, concluded that the model which showed better results in accordance with experimental data was the minimum circumscribed ellipse model.

2006 – Wang et al. concluded that for the same equivalent Von Mises stress (of multiaxial loadings), fatigue life became shorter with the increase in the loading nonproportionality, being the minimum fatigue life obtained for the 90º out of phase loading. This was based on tests done with Aluminum LY12CZ specimens. They proposed a new critical plane damage parameter based on shear stress range, normal stress and normal stress range which acts perpendicularly to the critical plane. The new parameter showed good correlation for the tests they had done.

In this same year Reis et al. [27] did a multiaxial loading experimental study of the steels 42CrMo4 and CK45. By fractography analysis they concluded that initial crack planes were determined with a high precision by the multiaxial fatigue damage models that were based mainly in shear, i. e., Findley, Brown Miller, Fatemi-Socie and Liu II. The models based mainly on the axial strengths, i. e., SWT and Liu I didn't show so good critical plane location determination.

2007 – In the study [28] S. Hasegawa et al. presented several conclusions on uniaxial LCF of an extruded AZ31 magnesium alloy which have been obtained for stress controlled loads:

- easy yielding in compression by twinning makes the hysteresis curve asymmetric. The curve is further characterized by quasi-elasticity during unloading from compression;
- the asymmetry of the hysteresis curve fairly disappears at half life with the stress controlled loads; the fatigue lives and deformation characteristics can be expressed by Coffin-Mason type equation.

2009 – In the study [29] S. Begum et al. observed asymmetrical cyclic behavior as in reference [28] doing strain controlled axial tests of an extruded AZ31 magnesium alloy.

2010 – In the study [30] J. Albinmousa et al. did cyclic axial and cyclic shear tests to a tubular specimen of an extruded bar of AZ31B magnesium alloy. They observed that cyclic axial test results exhibit asymmetrical cyclic behavior due to twinning as in the references [28] and [29]. Plastic strain recovery is also observed in axial hysteresis loop (the size of the half life hysteresis loop is smaller than the 1st cycle size) as in figure 2.2 a). The cyclic torsional behavior exhibits a symmetric behavior as in figure 2.2 b).

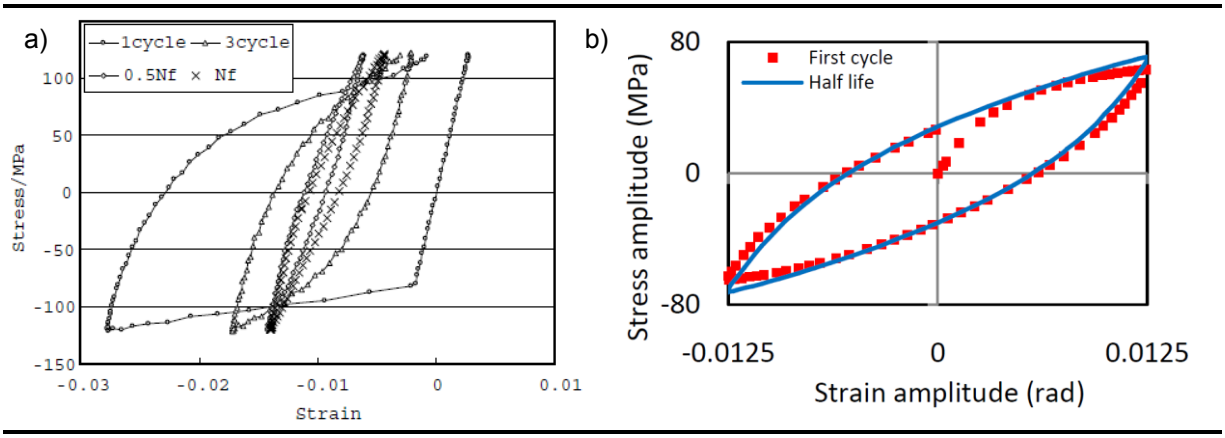

Figure 2.2 – Hysteresis curves for: a) cyclic stress controlled axial test [28] and b) cyclic strain controlled shear test [30]

In the reference [30], studies are also made about strain controlled multiaxial fatigue for proportional and nonproportional loadings. Asymmetric hysteresis loop is observed for axial mode or axial hysteresis loop; it is also observed plastic strain recovery for axial mode. The hysteresis curve of shear mode is observed to be asymmetric in contradiction of the symmetric behavior shown in cyclic shear test. The asymmetry of the shear mode tends to vanish with the increase of cycles number (by half life symmetric observation); this is due to large plastic strain recovery in the compression cycle, leading to an increase in the compression yield value.

In terms of damage parameters the opinion of the authors [30] is that any damage parameter must accommodate the yield asymmetry observed in the hysteresis cycles. They proposed total cyclic energy (plastic strain and positive elastic energies) as damage parameter D and established a fatigue life time equation:

$$log(D) = m\left[log\left(N_f\right)\right]^n \quad (2.1)$$

In the equation 2.1, m and n are fatigue parameters and have values, e. g., respectively 20.5 and -0.45. The relation 2.1 presented a correlation factor value of $R^2 = 0.830$ for the multiaxial proportional and nonproportional loadings data.

In the work [31] Reis et al. did a multiaxial fatigue analysis of a specimen using the finite elements method and the plasticity model of Jiang and Sehitoglu's. They concluded that the state of stresses evolution observed in these simulations agreed well with experimental results obtained in the case of the steel 42CrMo4.

2.2 Proportional and Nonproportional Loadings

From history it has been observed that multiaxial fatigue loads can be proportional or nonproportional. To understand the concept of proportional and nonproportional loads a simple example is given. Consider the shaft in figure 2.3. The shaft has axial and shear loadings. Since fatigue is generally a surface phenomenon, the state of stresses can be considered 2D because the normal stress to the surface is zero. Consider a coordinate system XY fixed with the shaft. Consider a coordinate system X´Y´ defined so that, stress along X´ axis $\sigma_{X'} = \sigma_1$ the first (the biggest) principal normal stress. As can be observed in figure 2.3 from point A to B and from point B to C, X´ axis remains fixed relative to X. Since principal normal stresses axes are perpendicular to one another, it can be concluded that the orientation of the principal stresses axes hasn't changed with time. Because principal stresses axes are fixed in space along time, the loading is named proportional loading.

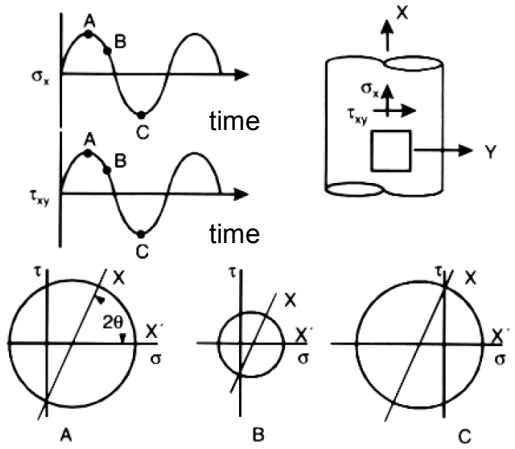

Figure 2.3 – Proportional loading [32]

However as it can be seen in figure 2.4, if axial stress is made constant and shear stress sinusoidal (considering that $\sigma_{X'} = \sigma_1$ and the same axis too) from point A to E it can be observed that X' doesn't always coincide with the maximum principal normal stress. This means that there is a rotation of the principal stress axis in space or a rotation relative to the coordinate system XY. Because principal stresses axes rotate in space along time, these types of loadings are called nonproportional loadings.

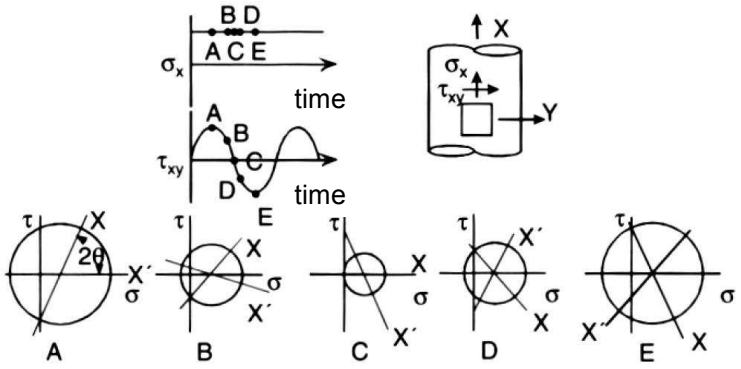

Figure 2.4 – Nonproportional loading [32]

To illustrate the principal stresses orientation changes with multiaxial sinusoidal loadings, let´s consider a generic multiaxial sinusoidal load applied to the shaft in such a way that in the surface of the shaft the present loads are as in figure 2.5 a). σ represents axial stress and is the same for all loading cases. τ_i in figure 2.5 b) is the shear stress that is i degrees out of phase with axial stress. A combination of a σ and one τ_i is a multiaxial stress state, so there are 4 different stress states presented in figure 2.5. Other variables referenced to the τ_i multiaxial load case will have the i index. In the abscissas, time is represented in a variation from 0 s to 2π seconds. The stress states obey to the relation $\sigma = \sqrt{3} * \tau$. Representation in typical form $\sqrt{3} * \tau \; vs \; \sigma$ is presented in figure 2.5 b).

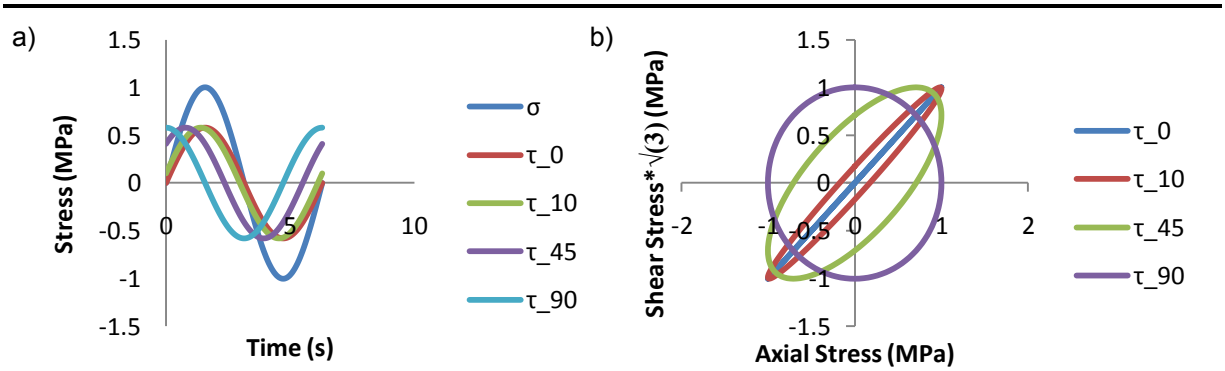

Figure 2.5 – a) Stresses vs time; b) shear stresses vs axial stress

The respective principal axis angle can be determined by the equation (see annex A):

$$\theta = \frac{1}{2} tan^{-1}\left(\frac{2\tau}{\sigma}\right) \quad (2.2)$$

Applying this relation, the figure 2.6 a) is obtained. As it can be seen the angle doesn't change for the case of τ_0 as discussed about figure 2.3. As the shear stress τ out of phase angle becomes near 90 from 0 degrees, more principal axis angles are traversed. Velocity of how these angles are traversed can be determined by the equation 2.3, which is represented in figure 2.6 b).

$$V = \frac{\theta_{i+1} - \theta_i}{t_{i+1} - t_i} \quad (2.3)$$

The velocity is approximately constant for the case of 90 degrees. As soon as stress state becomes more near 0 degrees from 90 degrees, the velocity tends to go near zero with more quick variations.

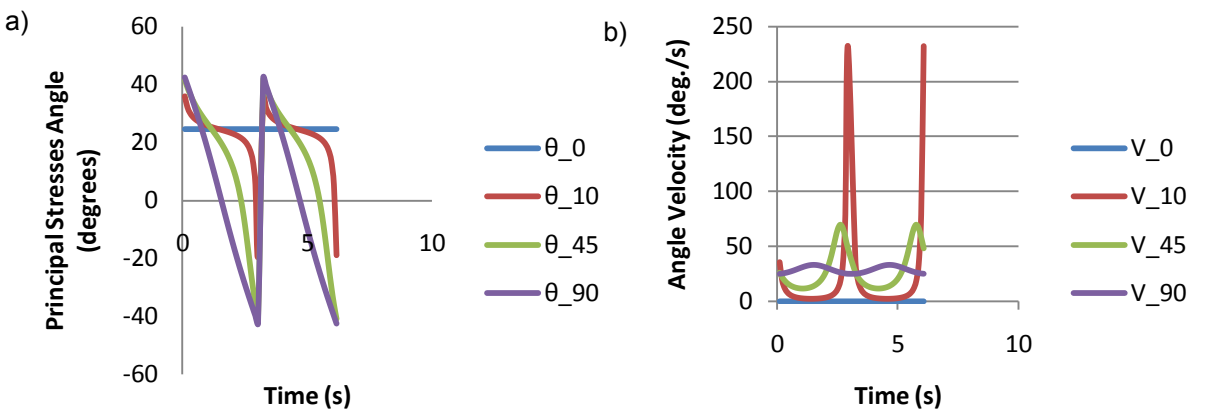

Figure 2.6 – Description of multiaxial sinusoidal loads a) principal stresses angle; b) angle velocity

2.3 Material Behavior

To characterize the cyclic deformation of a material, it is needed to understand the material behavior. This information is used to build plasticity models that simulate the change of material stresses states because of a loading acting on it during the cyclic deformation. Material behavior in cyclic deformation can generally be characterized by a group of different phenomena:

- isotropic hardening;
- kinematic hardening;
- cyclic creep or ratcheting;
- mean stress relaxation;
- nonproportional hardening.

These features will be analyzed in the next sections. A particular case of 2D stress state of torsion and tension loading is used to describe the concepts previously mentioned.

2.3.1 Isotropic Hardening

Isotropic hardening is the change in the material yield strength due to strain of the material after its yield limit. Figure 2.7 shows an example. On the left it is the equivalent stress vs equivalent strain response to isotropic hardening. On the right it is the response in the $\sqrt{3} * \tau \, vs \, \sigma$ plane as circumferences representing von Mises yield surface. The yield surface is determined equaling von Mises yield stress (defined by the equation 2.4) of torsion & tension stress state to the yield stress verified in a tension test. The result is the equation 2.5, which represents a circle in the $\sqrt{3} * \tau \, vs \, \sigma$ plane. At point A plastic deformation begins causing hardening work in the material as dislocations are interacting with each other. At point B material is unloaded to a zero stress state. Next it is reloaded to

$\bar{\sigma}_B$ stress state, which will make the material yield at $\bar{\sigma}_B$ (a new yield strength) and the plastic deformation will continue along its original stress-strain path; this effect is called material memory.

$$\sigma_{von\ Mises} = \frac{1}{\sqrt{2}}\sqrt{(\sigma_X - \sigma_Y)^2 + (\sigma_Y - \sigma_Z)^2 + (\sigma_X - \sigma_Z)^2 + 6({\tau_{XY}}^2 + {\tau_{YZ}}^2 + {\tau_{XZ}}^2)} \quad (2.4)$$

$$\sigma^2 + 3(\tau^2) = {\sigma_{yield}}^2 \quad (2.5)$$

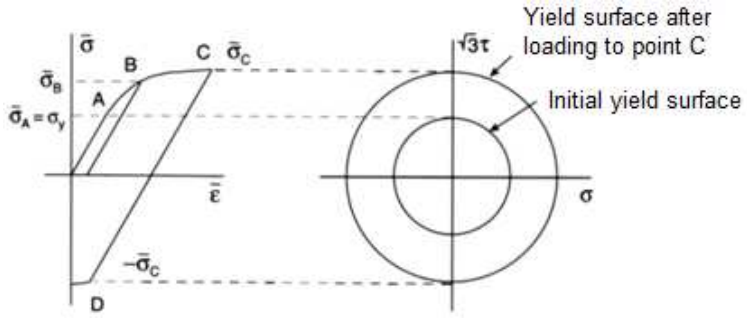

Figure 2.7 – Isotropic hardening [32]

Continuing loading to point C will make $\bar{\sigma}_C$ the new yield strength. Note that the yield surface has changed size as in figure 2.7. If now the material is compressed, since it is isotropic, will have yield strength value as $-\bar{\sigma}_C$ (point D). Note that isotropic hardening only makes the yield surface expand in all directions.

2.3.2 Kinematic Hardening

Kinematic hardening models the Bauschinger effect and material memory. There is a yield surface translation with no change in shape or size which happens only when there is plastic straining. Figure 2.8 illustrates this type of hardening. Material begins to yield at point A. Next it is loaded to point B where the plastic deformation results in a translation of the yield surface. Now the material is unloaded to zero stress state. Reloading it to point B will make it yield at $\bar{\sigma}_B$. However if at point B material is compressed to C, it will yield at $\bar{\sigma}_B - 2\sigma_y$ because of the translation of the yield surface. Translation of the yield surface is generally represented by a vector α and occurs in the direction of the plastic strain.

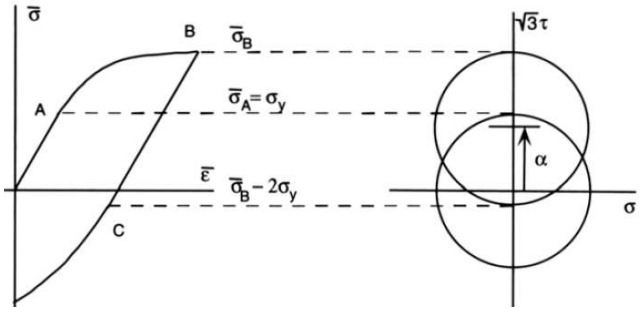

Figure 2.8 – Kinematic hardening [32]

Real materials show aspects of both kinematic and isotropic hardening until they become cyclically stable. After that they only show kinematic hardening effects. Because of that if transient material response is not of interest (most cases of fatigue analysis), only kinematic hardening is modeled.

2.3.3 Cyclic Creep or Ratcheting

Ratcheting or cyclic creep models the mean plastic strain increase during each cycle of a stress controlled deformation with a mean stress. It is the accumulation of plastic deformation and it is observed in materials subjected to a mean stress. In figure 2.9 it is illustrated the stress state of a thin walled tube subjected to a cyclic shear strain with a static axial stress. Consider that shear strain range is enough to do plastic deformation during each cycle. As can be observed in figure 2.9 total axial deformation is increasing during each cycle. First the specimen is loaded both in axial and shear strains to point A. After that the specimen shear strain is cycled with a constant axial stress. Loading the specimen to point B as in figure 2.9 it is an elastic phenomenon. However as soon as point B is passed, plastic deformation occurs and shear loadings produce axial deformation. The cyclic creep decreases after some cycles and becomes stable.

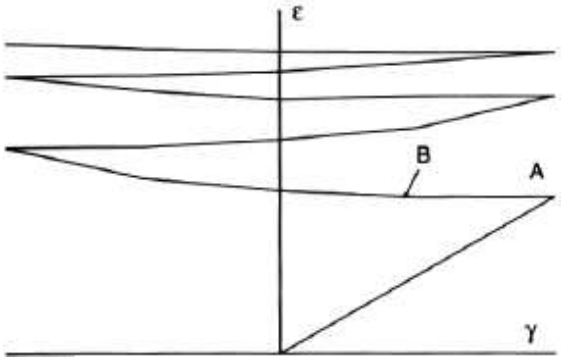

Figure 2.9 – Ratcheting [32]

2.3.4 Mean Stress Relaxation

Mean stress relaxation models the tendency of the mean stresses to go to zero during stress controlled deformation with a mean strain. This is illustrated by figure 2.10. In figure 2.10 it can be seen that the mean stress tends to zero after each cycle.

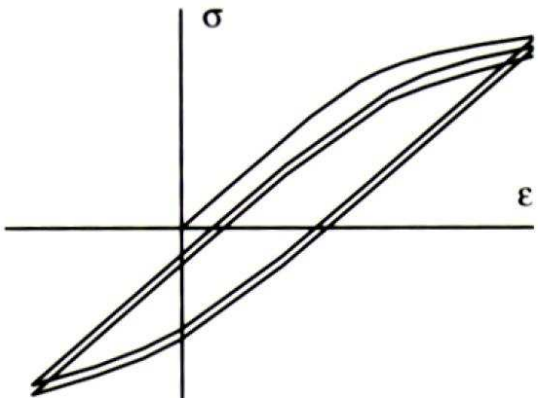

Figure 2.10 – Mean stress relaxation [32]

Plasticity models of mean stress relaxation and cyclic creep have been built for years, but none of them has gained widespread use.

2.3.5 Nonproportional Cyclic Hardening

As it has been explained in section 2.2, nonproportional loadings are the load paths that cause the principal stress axis to rotate. In figure 2.11 stress vs strain curves are presented for proportional and nonproportional loadings. Nonproportional loading as it can be observed causes additional cyclic hardening relative to an in phase load. The 90º out of phase loading has been verified as the loading path to produce the largest degree of nonproportional hardening. The magnitude of this hardening effect is highly dependent on the material microstructure and the ease with which slip systems develop in a material.

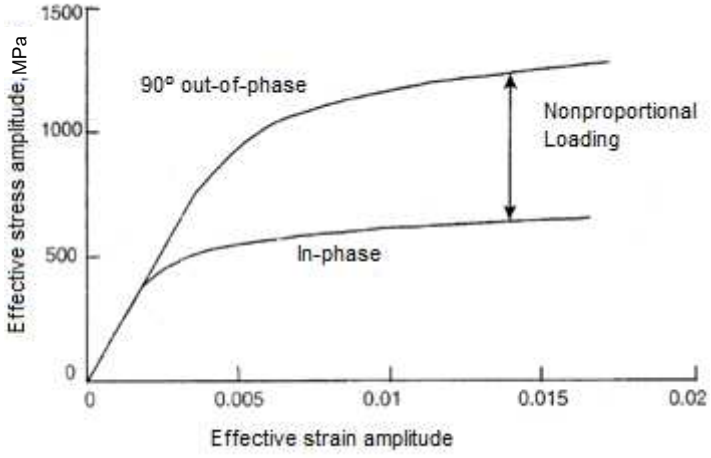

Figure 2.11 – Proportional and nonproportional loading stress-strain curves [32]

To quantify this new nonproportional hardening several factors were developed. One of them is Kanazawa nonproportionality factor. Other measures of nonproportionality have been proposed but

due to high complexity they have not become widely used. Kanazawa factor is based on the interaction of slip on different planes in the material. It can be calculated using the equation:

$$F = \frac{Shear\ strain\ range\ at\ 45º\ to\ maximum\ shear\ plane}{Maximum\ shear\ strain\ range} \quad (2.6)$$

The factor F depends on both phase angle and amplitude. To illustrate this, a series of sinusoidal loading paths are presented in figure 2.12. On the left loadings of equal amplitude ($\gamma = 2\varepsilon$) are presented with different phase angles. On the right the figure shows loading paths of different shear

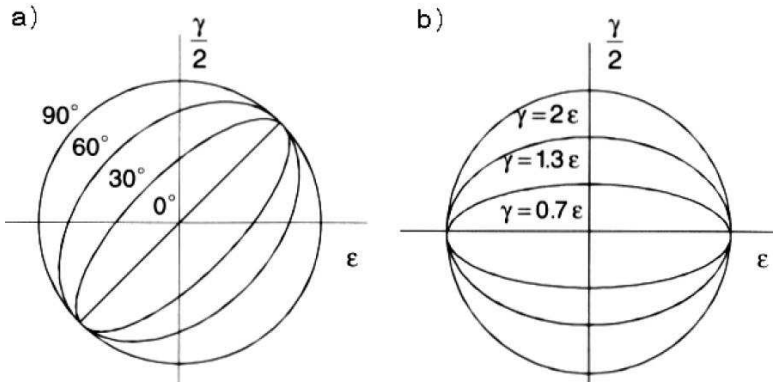

Figure 2.12 – Nonproportional loading histories; a) with $\gamma = 2\varepsilon$; b) with the same phase angle [32]

strain amplitudes with equal phase angle. Calculating Kanazawa factor for the different loading paths the results presented in table 2.1 can be obtained. As it can be observed in table, F is a measure of the ellipticity of the loading history in the $\frac{\gamma}{2} vs\ \varepsilon$ plane because as soon as the ellipse becomes more similar to a circumference the factor goes from 0 to 1.

Phase angle	**0º**	**31º**	**60º**	**90º**	$\boldsymbol{\gamma = 1.3\varepsilon}$	$\boldsymbol{\gamma = 0.7\varepsilon}$
$\boldsymbol{F}$	0	0.27	0.57	1.0	0.67	0.33

Table 2.1 – Kanazawa factor for strain histories in figure 2.11 [32]

Experiments have shown that Kanazawa factor can be used to model the increase in the cyclic strength coefficient using the equation:

$$K'_{np} = K'(1 + \alpha F) \quad (2.7)$$

In the equation 2.7, α is a constant dependent on the material and temperature. The nonproportional hardening coefficient α has values from zero to 1. Several examples are presented in table 2.2.

Material	$\boldsymbol{\alpha}$
314 stainless steel	0.5-1.0
OFHC copper	0.3
6061-T6 aluminum	0.2
1% Cr-Mo-V steel	0.14
1100 aluminum	0.0

Table 2.2 – Nonproportional hardening coefficient [32]

2.4 Plasticity Model

A cyclic plasticity model is generally build by 3 components:

- Yield function;
- Flow rule;
- Hardening rule.

Before yielding occurs, Hook´s Law can be used to calculate stresses. To determine when yield occurs a yield function is used. The function describes the combinations of stresses that cause the material to yield or to begin plastic deformation. Typical yield function is von Mises criterion which states that yield occurs when the equality is verified:

$$Yield\ Function = Y_F = {\sigma_X}^2 + {\sigma_Y}^2 + {\sigma_Z}^2 - \sigma_X\sigma_Y - \sigma_Y\sigma_Z - \sigma_Z\sigma_X + 3({\tau_{XY}}^2 + {\tau_{YZ}}^2 + {\tau_{XZ}}^2) = {\sigma_{yield}}^2 \quad (2.8)$$

Stresses and strains during material plastic deformation show a dependence on the prior loading history. Because of that typically an incremental plasticity procedure is implemented. To make this incremental plasticity model procedure, relations between the stresses and plastic strains are needed, i. e., constitutive equations. These relations are called the flow rule. Typically increments of strain are decomposed in elastic and plastic components:

$$d\varepsilon = d\varepsilon^e + d\varepsilon^p \quad (2.9)$$

Commonly the flow rules are based on the normality postulate by Drucker [32], i. e., it is supposed that plastic strain increment vector $d\varepsilon_{ij}^p$ is normal to the yield surface during plastic deformation. For axial & torsion loadings this statement can be represented by the equations:

$$d\varepsilon_X^p = d\lambda\frac{\partial Y_F}{\partial \sigma_X} \quad \& \quad d\gamma_{XY}^p = d\lambda\frac{\partial Y_F}{\partial \tau_{XY}} \quad (2.10)$$

where the positive scalar $d\lambda$ is given by:

$$d\lambda = \frac{1}{C}\frac{\frac{\partial Y_F}{\partial \sigma_X}d\sigma_X + \frac{\partial Y_F}{\partial \tau_{XY}}d\tau_{XY}}{\left(\frac{\partial Y_F}{\partial \sigma_X}\right)^2 + \left(\frac{\partial Y_F}{\partial \tau_{XY}}\right)^2} \quad (2.11)$$

where C is the tangent modulus of the stress vs strain curve.

To describe the changes in yield criterion during plastic straining there are hardening rules. So they describe changes in the yield surfaces. Detailed description of the hardening plasticity models will not be mentioned here. The reference [32] can be consulted for further details.

The incremental plasticity procedure used in this work is the model of Jiang & Sehitoglu [33], [34] which uses von Mises yield function. The model has been programmed in C++ language by Darrell F. Socie. The only task left is to program the input data and material properties.

2.5 Damage Parameters & Fatigue Life Estimation

To determinate how much damage a multiaxial fatigue load path does to the material, fatigue damage parameters are used. There are several damage parameters which have been described in the section fatigue history. In this work focus is made in parameters based on the critical plane approach. Remember that the critical plane approach considers only one or more planes within a material subject to a maximum value of a damage criterion. Naturally fatigue life is determined by the combination of stresses and strains acting on a critical plane.

2.5.1 Findley Model

Observing the fatigue crack initial orientation in the steel, Findley (1956) and in aluminum Findley & Tracy (1973) discussed the influence of normal stresses that load the maximum shear stress plane. According to Findley the material damage is caused by normal stress acting on a plane that has a linear contribution relative to the shear stresses present in that plane. Failure is verified for:

$$\left(\frac{\Delta\tau}{2} + k\sigma_n\right)_{max} = f \quad (2.12)$$

By this equation, the previous critical plane formulation states that initial crack begins with θ orientation which corresponds to the maximum damage parameter:

$$max\left(\tau_a + k\sigma_{n,max}\right) \quad (2.13)$$

The constant k is a material constant. τ_a is the alternating stress and $\sigma_{n,max}$ is the maximum normal stress acting in plane θ. The constant k can be determined by using a torsion test and a axial or bending test. The equations to calculate f are respectively:

$$\sqrt{1+k^2}\frac{\Delta\tau}{2} = f \quad (2.14)$$

$$\sqrt{(\sigma_a)^2 + k^2(\sigma_{max})^2} + k\sigma_{max} = 2f \quad (2.15)$$

Combining the equations 2.14 and 2.15 the equation 2.16 is obtained.

$$\frac{\sigma_{a,R=-1}}{\tau_{a,R=-1}} = \frac{2}{1 + \frac{k}{\sqrt{1+k^2}}} \quad (2.16)$$

Which can be solved to determine k.

To determine fatigue life or fatigue life cycles number in LCF the fatigue life equation is:

$$\left(\frac{\Delta\tau}{2} + k\sigma_n\right) = {\tau_f}^* \left(N_f\right)^b \quad (2.17)$$

Where the variable ${\tau_f}^*$ is determined using the torsional fatigue strength coefficient, ${\tau_f}'$, in the equation:

$${\tau_f}^* = \sqrt{1+k^2} * {\tau_f}' \quad (2.18)$$

2.5.2 Brown & Miller Model

Brown and Miller (1973) analyzed many works in LCF with focus made in the crack formation and early growth. In some cases octahedral shear stress shows being effective in describing HCF. The octahedral shear strain and maximum shear strain show not to be effective in describing LCF. Brown and Miller made tests of combined tension and torsion loading with a constant shear strain range. After observing the results they concluded two strain parameters were necessary to describe fatigue failure. They chose as the two parameters both the cyclic shear strain and the cyclic normal strain acting on the plane of maximum shear.

Brown and Miller suggested that there are two different types of cracks, i. e., Case A and Case B cracks. They are illustrated in figure 2.13. Case A crack type $(\sigma_3/\sigma_1 < 0)$ tends to be shallow and have a small aspect ratio; shear stress acts perpendicular to the free surface along the crack depth; Case A crack type is always present in combined axial & torsion loadings. Case B crack type $(\sigma_2/\sigma_1 > 0)$ tends to grow into depth due to shear stresses; Case B cracks always intersect the surface at an angle of 45º. Tension loading can present either modes of cracking.

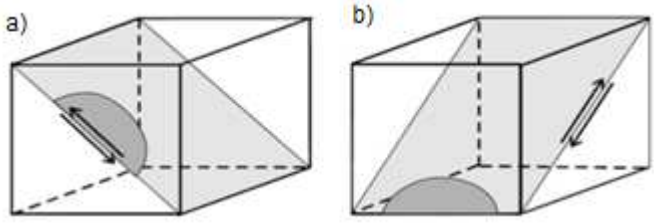

Figure 2.13 – a) Case A cracks; b) Case B cracks [32]

Based on the new information, Brown and Miller proposed a criterion for each type of cracking:

$$\begin{cases} Case\ A\text{:}\ \left(\dfrac{\Delta\gamma}{g}\right)^{j} + \left(\dfrac{\varepsilon_n}{h}\right)^{j} = 1 \\ Case\ B\text{:}\ \dfrac{\Delta\gamma}{2} = constant \end{cases} \quad (2.19)$$

In the equations 2.19 g, h and j are constant. j has values in the range from 1 for brittle materials to 2 for ductile materials.

After this model Kandil, Brown and Miller proposed a simple formulation for Case A cracks:

$$\Delta\hat{\gamma} = (\Delta\gamma_{max}^{\alpha} + S\Delta\varepsilon_n^{\alpha})^{\frac{1}{\alpha}} \quad (2.20)$$

In the equation 2.20 $\Delta\hat{\gamma}$ is the equivalent shear strain range and S is a material dependent parameter. S represents the influence of the normal strain on material crack growth and is determined correlating axial and torsion data. Wang and Brown simplified plus the above formulation, considering $\alpha = 1$ and adding a mean stress term. They obtained:

$$\frac{\Delta\hat{\gamma}}{2} = \frac{\Delta\gamma}{2} + S\Delta\varepsilon_n = A\frac{\sigma_f'}{E}(2N_f)^b + B\varepsilon_f'(2N_f)^c \quad (2.21)$$

In the equation 2.21:

$$\begin{cases} A = 1.3 + 0.7S \\ B = 1.5 + 0.5S \end{cases} \quad (2.22)$$

According to Brown and Miller the damage critical plane is determined by:

$$max\left(\frac{\Delta\gamma}{2} + S\Delta\varepsilon_n\right) \quad (2.23)$$

The Brown and Miller constant S can be determined by the expression 2.24 doing $N_f \to \infty$ and $v_e = v_p = v$:

$$S = \frac{\frac{\tau_f'}{G}(2N_f)^{b\gamma} + \gamma_f'(2N_f)^{c\gamma} - (1+v_e)\frac{\sigma_f'}{E}(2N_f)^b - (1+v_p)\varepsilon_f'(2N_f)^c}{(1+v_e)\frac{\sigma_f'}{E}(2N_f)^b + (1+v_p)\varepsilon_f'(2N_f)^c} \quad (2.24)$$

To determine fatigue life for Case A crack type and include mean stresses effects the expression 2.25 can be used:

$$\frac{\Delta\gamma_{max}}{2} + S\Delta\varepsilon_n = A\frac{\sigma_f'}{E}(2N_f)^b + B\varepsilon_f'(2N_f)^c \quad (2.25)$$

2.5.3 Fatemi & Socie Model

Fatemi and Socie studied the model of Brown and Miller. They proposed that the normal strain term should be replaced by the normal stress. The justification for this change is that during shear loading the irregular crack surface results in resistive forces that reduce crack stresses, retarding crack growth and as a result increasing fatigue life. The phenomenon is illustrated in figure 2.14. Fractography evidence for this phenomenon has been obtained. They verified that in the case of pure torsion, the specimens showed an extensive rubbing. In the case of tension tests the fractography shows individual slip bands that were observed in the fracture surface.

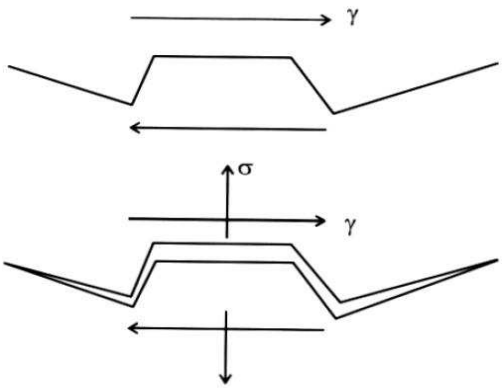

Figure 2.14 – The irregular crack surface acting as an "obstacle" to shear motion [32]

The critical plane can be determined by the equation:

$$max\left[\frac{\Delta\gamma}{2}\left(1+k\frac{\sigma_{n,max}}{\sigma_{yield}}\right)\right] \quad (2.26)$$

The Fatemi and Socie constant k can be determined by the expression 2.27 doing N_f equal to the number of cycles close to the obtained by the other damage parameters:

$$k=\left[\frac{\frac{\tau_f{}'}{G}(2N_f)^{b\gamma}+\gamma_f'(2N_f)^{c\gamma}}{1.3\frac{\sigma_f'}{E}(2N_f)^{b}+1.5\varepsilon_f'(2N_f)^{c}}-1\right]\frac{K'(0.002)^{n'}}{\sigma_f'(2N_f)^{b}} \quad (2.27)$$

This damage model can be understood as the cyclic shear strain modification by the normal stress to include crack closure effects. This model can be described by the following equation of fatigue life determination:

$$\frac{\Delta\gamma}{2}\left(1+k\frac{\sigma_{n,max}}{\sigma_{yield}}\right)=\frac{\tau_f'}{G}(2N_f)^{b\gamma}+\gamma_f'(2N_f)^{c\gamma} \quad (2.28)$$

The shear properties can be estimated by the axial properties or vice-versa using the table 3.3.

	Axial	Shear
Fatigue strength coefficient	σ_f'	$\tau_f' \approx \sigma_f'/\sqrt{3}$
Fatigue strength exponent	b	$b\gamma \approx b$
Fatigue ductility coefficient	ε_f'	$\gamma_f' \approx \sqrt{3}\varepsilon_f'$
Fatigue ductility exponent	c	$c\gamma \approx c$
Modulus	E	$G \approx E/[2(1+\nu)]$

Table 2.3 – Formulas to estimate shear fatigue properties by axial fatigue properties [32]

2.5.4 Smith, Watson & Topper Model

Brown & Miller and Fatemi & Socie critical plane models have been modeled using materials which have a dominant failure mechanism of shear crack nucleation and growth. A different model is needed for materials of crack growth on planes of maximum tensile strain or stress. Smith, Watson & Topper present that cracks nucleate in shear but initial life is determined by crack growth on perpendicular planes to the maximum principal stress and strain as illustrated in figure 2.15.

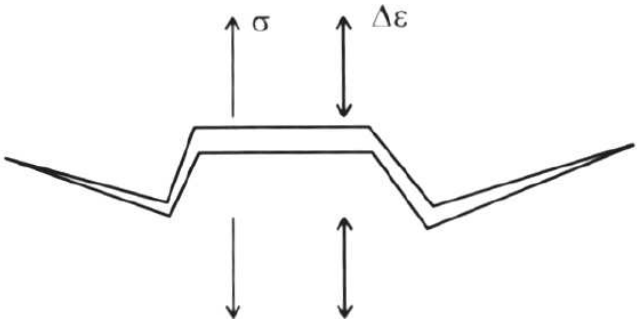

Figure 2.15 – Tensile crack growth [32]

The critical plane is determined by the expression:

$$max\left(\sigma_n \frac{\Delta\varepsilon_1}{2}\right) \quad (2.29)$$

Where $\Delta\varepsilon_1$ is the principal strain range. Fatigue life can be determined by the equation:

$$\sigma_{n,max}\frac{\Delta\varepsilon_1}{2} = \frac{\sigma_f'^2}{E}(2N_f)^{2b} + \sigma_f'\varepsilon_f'(2N_f)^{b+c} \quad (2.30)$$

2.5.5 Liu I & Liu II Models

Liu virtual strain energy (VSE) model is based on combined critical plane and energy models. They are critical plane models in the sense that work quantities are defined for specific planes within the material. In the case of multiaxial loading, VSE model considers two possible failure modes. A mode for tensile failure ΔW_I (axial work) and a mode for shear failure ΔW_{II} (shear work).

In the case of axial work, to determine work, firstly it is identified the plane where the axial energy is maximum and next it is added the respective shear energy in that plane:

$$\Delta W_I = max(\Delta\sigma_n \Delta\varepsilon_n) + \Delta\tau\Delta\gamma \quad (2.31)$$

The fatigue life is given by:

$$\Delta W_I = 4\sigma_f'\varepsilon_f'\left(2N_f\right)^{b+c} + \frac{4\sigma_f'^2}{E}\left(2N_f\right)^{2b} \quad (2.32)$$

In the case of shear work, to determine work, firstly it is identified the plane where shear energy is maximum and next it is added the respective axial energy in that plane:

$$\Delta W_{II} = max(\Delta\tau\Delta\gamma) + \Delta\sigma_n \Delta\varepsilon_n \quad (2.33)$$

The fatigue life is given by:

$$\Delta W_{II} = 4\tau_f'\gamma_f'\left(2N_f\right)^{b\gamma+c\gamma} + \frac{\left(4\tau_f'\right)^2}{G}\left(2N_f\right)^{2b\gamma} \quad (2.34)$$

3 Material, Software Analysis & Experiments Procedures

In this chapter firstly an analysis of the material properties of the extruded magnesium alloy AZ31 is made. The extruded magnesium alloy AZ31B-F is chosen. However the alloy order only arrived one month before ending the deadline to deliver this work. So a decision is taken to do ANSYS and C++ Plasticity program simulations with the available information of the AZ31 extruded magnesium alloy. The alloy arrived in a date enough to do a monotonic tension test, so the tensile test procedure is presented. Next the ANSYS and Plasticity program procedures are presented to run simulations. The last section presents how the damage parameters are programmed and how they are obtained.

3.1 Material

The material properties used for the Plasticity program analysis are the ones of the extruded AZ31 bar of reference [29] presented in figure 3.1. This bar is extruded in a temperature range of 360 to 382 ºC at an extrusion speed of 50.8 mm/s. The applied extrusion process ratio is about six, and after extrusion the alloy is air quenched.

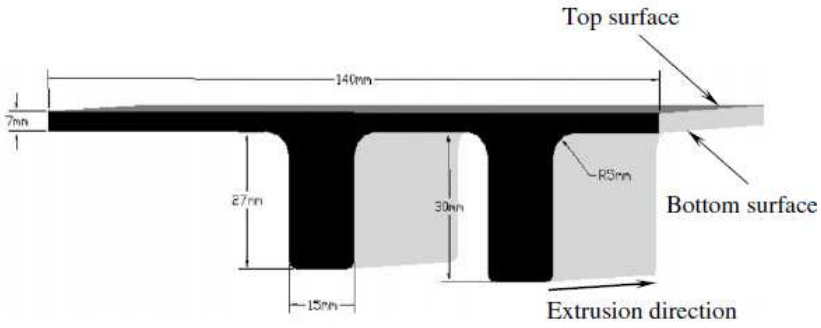

Figure 3.1 – AZ31 extruded test material selected in the paper [29]

The chemical composition of the alloy is presented in table 3.1.

Al	Zn	Mn	Fe	Ni	Cu	Mg
3.1	1.05	0.54	0.0035	0.0007	0.0008	Balance

Table 3.1 – Chemical composition (wt%) of the extruded AZ31 magnesium alloy [29]

The test specimens are taken from the plate shaped part excluding the bar sections. Fatigue samples of 140 mm in length are machined in the extrusion/longitudinal direction. The sub-sized samples for both tensile and fatigue tests followed the ASTM E8 standard. The thickness of the samples is kept unchanged (7mm). In figure 3.2 typical microstructures of the extruded AZ31 magnesium alloy are observed across the thickness.

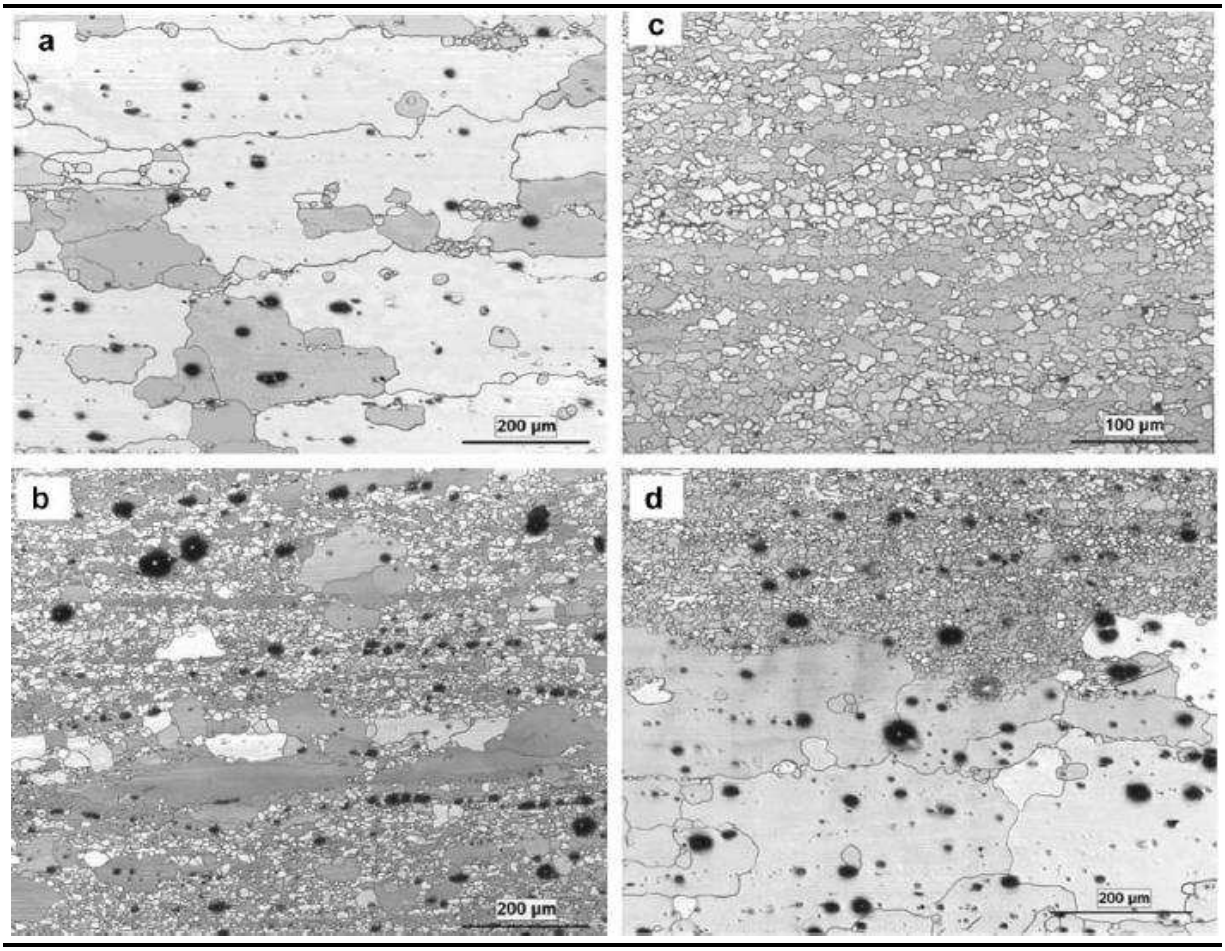

Figure 3.2 – Light microscope images of the microstructure of the extruded magnesium alloy AZ31 a) near the top surface showing large grains; b) below the top surface showing large to small grain transition; c) at the center of the specimen showing the small grains; d) near the bottom surface showing the small and large grains [29]

Figure 3.2 shows that the microstructure is non-uniform along the thickness of the specimen (grain size changes). The black dots presented in figure 3.2 are Mn- and Al- containing particles.

Tensile stress vs strain curve is determined at a strain rate of $1 \times 10^{-2}\ s^{-1}$. Figure 3.3 shows this curve. Correspondent monotonic material properties are presented at table 3.2.

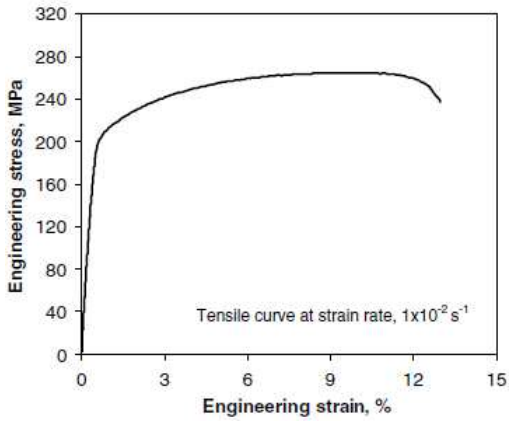

Figure 3.3 – Tensile stress vs strain curve of AZ31 Mg alloy [29]

Yield Strenght (Mpa)	Ultimate Tensile Strenght (MPa)	Elongation (%)	Young´s Modulus (GPa)	Strain Hardening Exponent (n)
201	264	15.2	45	0.13

Table 3.2 – Monotonic mechanical properties of AZ31 Mg alloy [29]

In reference [29] the LCF parameters are also determined for the extruded AZ31 magnesium alloy too. They are presented in table 3.3.

Low Cycle Fatigue Parameters	Extruded Mg Alloy AZ31
Cyclic strain hardening exponent, n'	0.34
Cyclic strength coefficient, K' (MPa)	1976
Fatigue strength coefficient, σ'_f (MPa)	616
Fatigue strength exponent, b	-0.15
Fatigue ductility coefficient, ε'_f (%)	1.78
Fatigue ductility exponent, c	-0.40

Table 3.3 – Low cycle fatigue parameters for the extruded AZ31 magnesium alloy [29]

3.2 Tensile Test

The tensile test is done in the electro-mechanics machine INSTRON 3360 illustrated in figure 3.4. The test followed the standard NP EN 10 002-1 (1990). To measure strain, an INSTRON extensometer with 25 mm of gauge length is used.

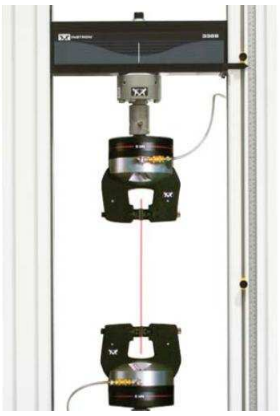

Figure 3.4 – INSTRON 3360 machine [35]

The specimen dimensions are presented in figure 3.5.

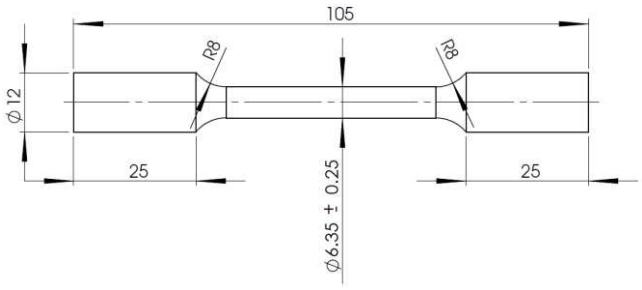

Figure 3.5 – Tensile test specimen; dimensions in mm

3.3 Stress Controlled Loadings

This is the section in which the stress controlled loadings to apply in ANSYS and C++ Plasticity program are defined. They are presented in table 3.4 in $\sqrt{3} * \tau$ vs σ plane. The loadings compare different equivalent states of stresses by changing loading path. Loadings are determined using Matlab software. The period of the loads is 0.1 s for cases 1 to 6 and 1.4 s for cases 7 and 8. A von Mises maximum load of 1 MPa is used to illustrate them.

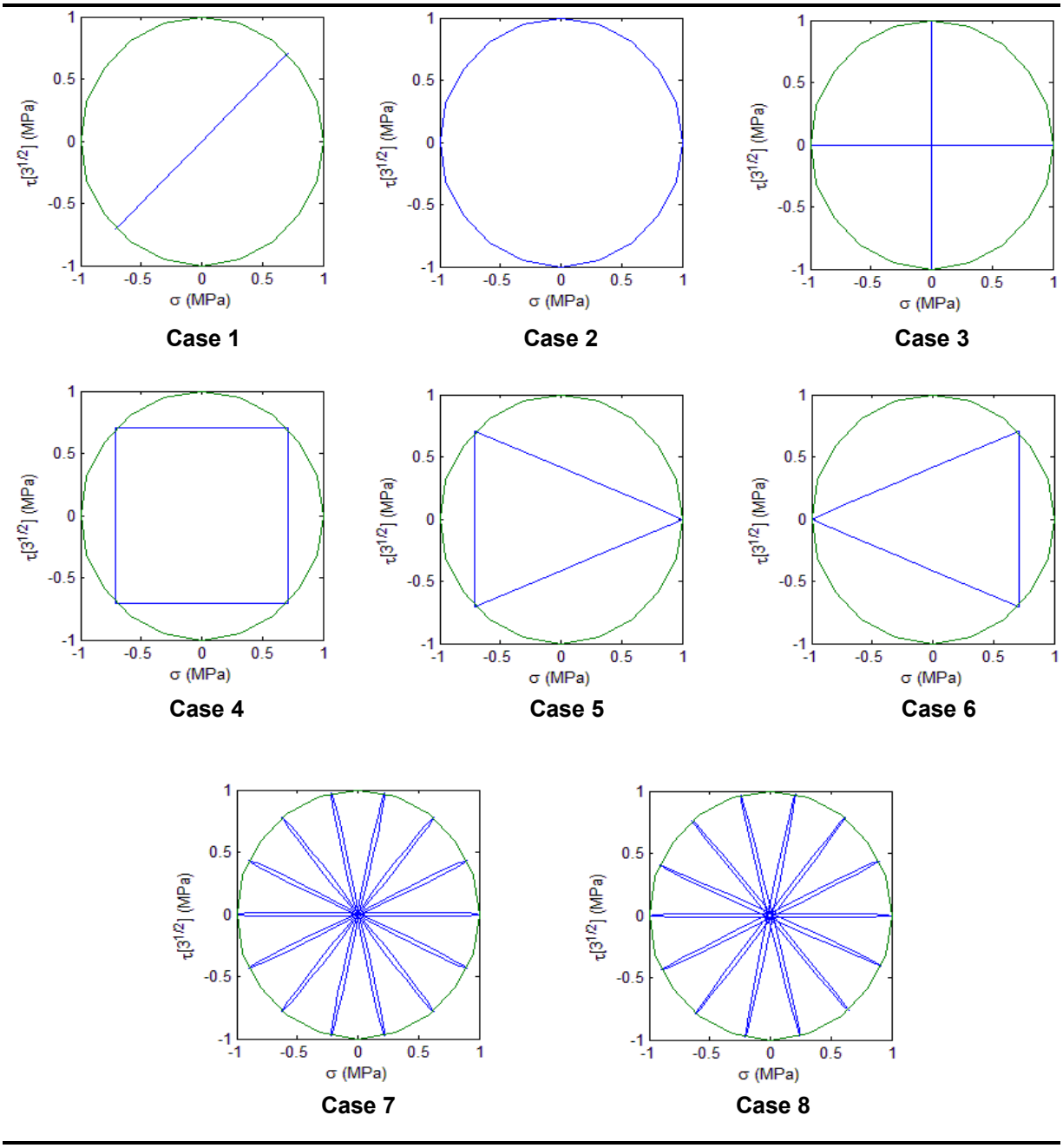

Table 3.4 – Stress controlled loads in the $\sqrt{3} * \tau$ vs σ plane

The loading cases are also presented in table 3.5 in loads vs time form.

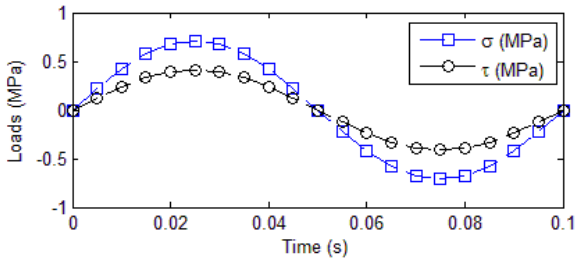

Case 1

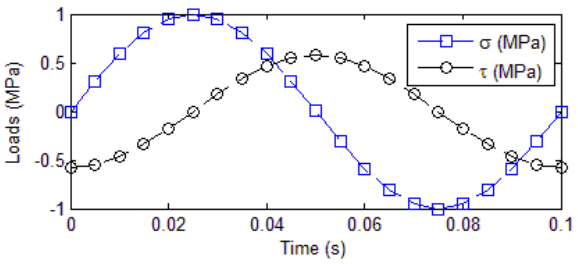

Case 2

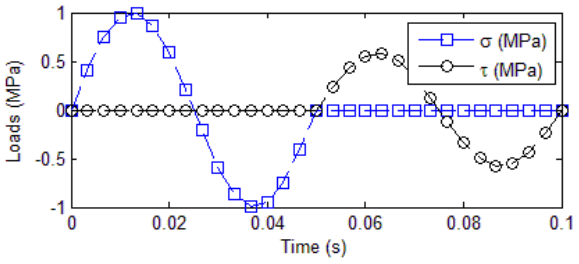

Case 3

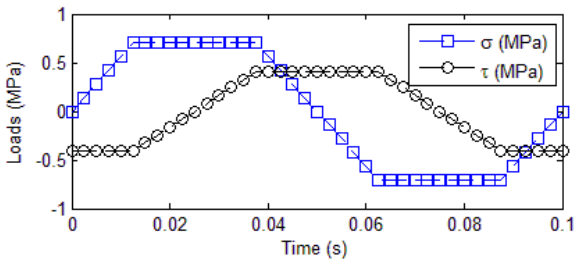

Case 4

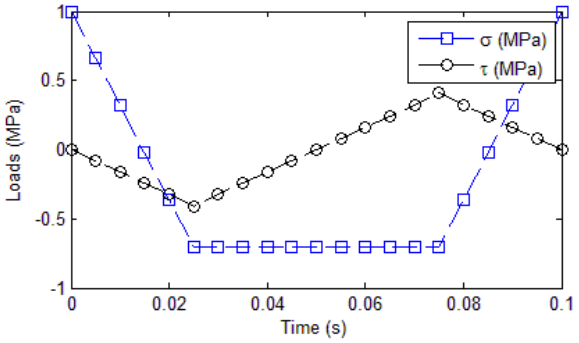

Case 5

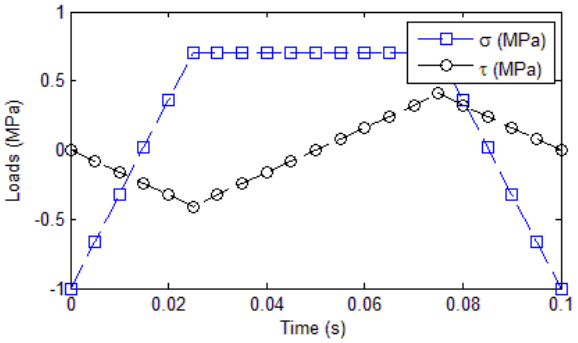

Case 6

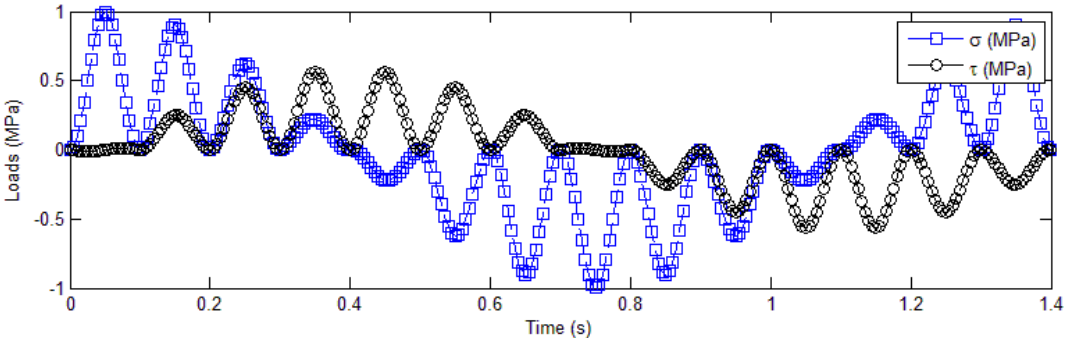

Case 7

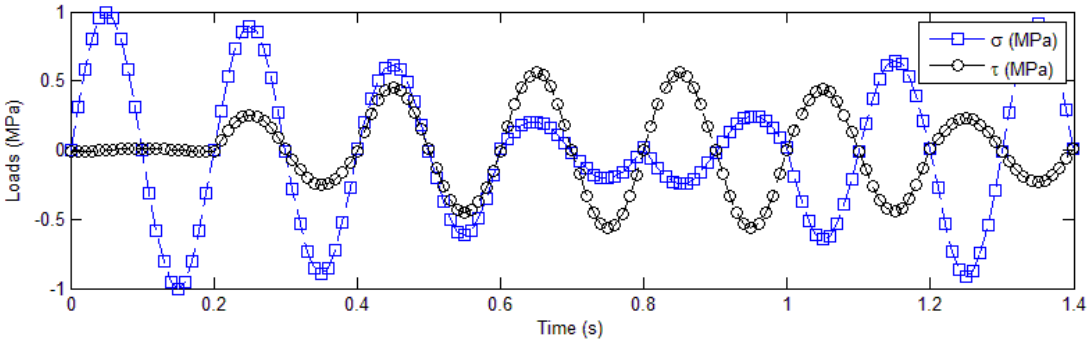

Case 8

Table 3.5 – Stress controlled loads as a function of time

3.4 ANSYS

To simulate using ANSYS multiaxial loading of a magnesium alloy several data are needed to set up the simulation: hardening model, specimen geometry and material properties. As it was said in section 2.1, multiaxial loading of magnesium has axial asymmetric stress vs strain curve and a shear curve that becomes symmetric along the cycle numbers. ANSYS doesn't have any simple hardening model for this type of material behavior. So the curve is modeled as symmetric. The hardening curve and material data used to simulate in ANSYS are the real stress vs real strain curve of the data presented in figure 3.3 and table 3.2 except the Young modulus. The value of Young modulus used is 44.8 GPa since it is the value of the AZ31B-F alloy and is near that of table 3.2, 45 GPa. The curve is configured in ANSYS using the ANSYS Multilinear Kinematic Hardening Material Model. The curve is represented in figure 3.6. Note that ANSYS values are in the SI unit system. The real stress vs real strain curve is determined based on engineering stresses and strains or respective nominal values using the equations:

$$\sigma_{real} = \sigma_{nominal}(1 + \varepsilon_{nominal}) \quad (3.1)$$

$$\varepsilon_{real} = ln(1 + \varepsilon_{nominal}) \quad (3.2)$$

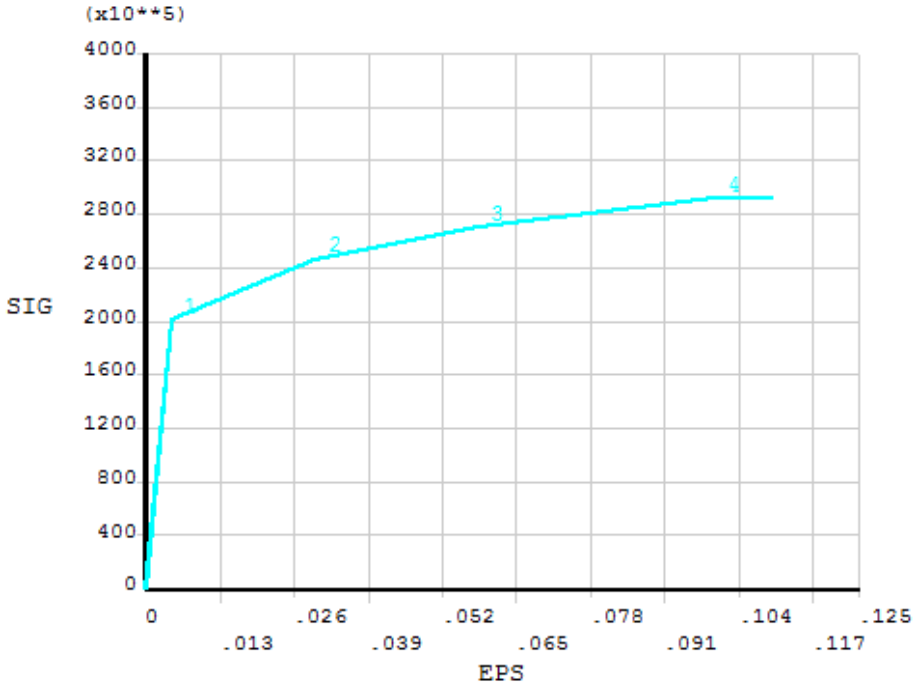

Figure 3.6 – ANSYS hardening stress vs strain curve; stress (SIG) vs strain (EPS)

The specimen modeled using ANSYS is chosen to be the same used for typical multiaxial stress controlled fatigue experiments and used in previous master theses, e. g., [25] and [26]. The specimen is presented in figure 3.7 plus the ANSYS geometric model.

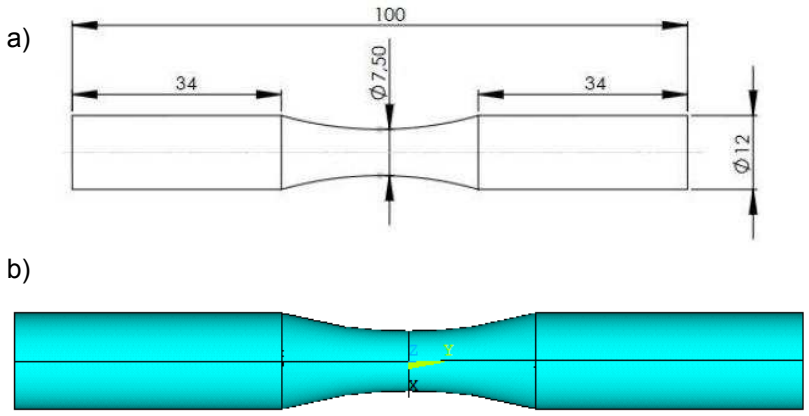

Figure 3.7 – Multiaxial fatigue a) experiment specimen geometry; b) experiment specimen modeled in ANSYS; dimensions in mm

Additional material properties are obtained searching in Efunda website [13] for the alloy AZ31B-F. These properties are in table 3.6. The Poisson coefficient is necessary for the ANSYS simulation.

	AZ31B-F Magnesium Alloy
Density, $(\mathbf{Kg/m^3})$	1770
Poisson coefficient	0.35

Table 3.6 – Material properties for ANSYS simulation [13]

The next step is to choose the finite element to use. Reis [16] has done previous finite element simulations with multiaxial loading of fatigue specimens. Based on this report it is decided that the finite element to use is a 20 nodes element of quadratic displacement behavior. The element is the SOLID 186 of the ANSYS library and has 3D displacements as degrees of freedom. It is presented in figure 3.8.

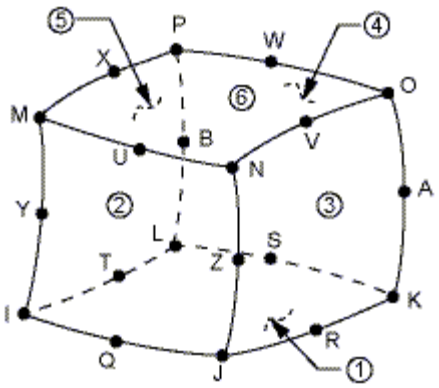

Figure 3.8 – SOLID 186 ANSYS structural element from ANSYS Help

The mesh is constructed in a manner to avoid elements distortion and irregular mesh fitting to the original geometry. In reference [16] the number of elements used for a 50 mm specimen in a multiaxial loading analysis is 1944. In this report since it is used 8424 elements for a 100 mm specimen it is assumed that the mesh is converged. The final mesh is represented in figure 3.9. Mesh is made close to 3D uniform shape so that elements rigidity can be isotropic.

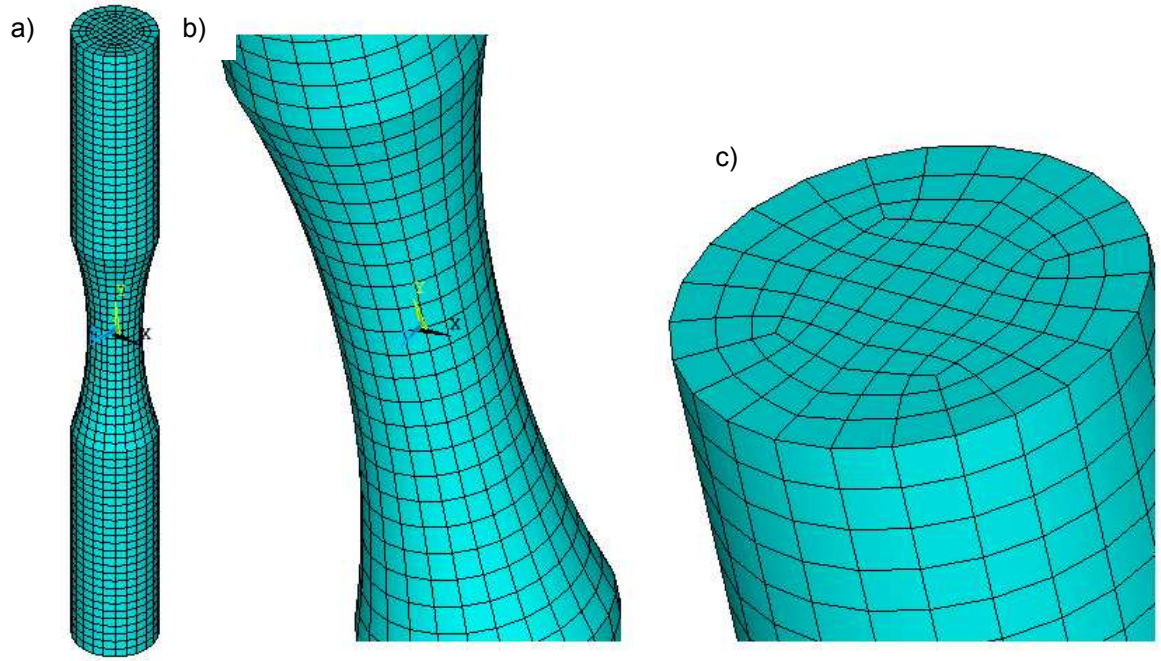

Figure 3.9 – Multiaxial fatigue specimen mesh a) general mesh; b) center section; c) top section

To apply multiaxial loadings it has to be defined how to apply the boundary conditions. The boundary conditions are applied at the bottom and at the top of the specimen as it is shown in figure 3.10 a). At the bottom all the displacements are fixed to be zero; see figure 3.10 c). At the top axial and shear loadings are applied as pressures; see figure 3.10 b). Since many loading cases cannot be defined using ANSYS Function Editor, the values have to be upload in a table TIME vs PRESSURE from text files. These text files are built with the help of Microsoft Excel and the Matlab program. The pressures boundary conditions are represented as lines across the elements the pressure acts. In figure 3.10 b) green lines represent axial pressure; red and blue lines represent shear pressure.

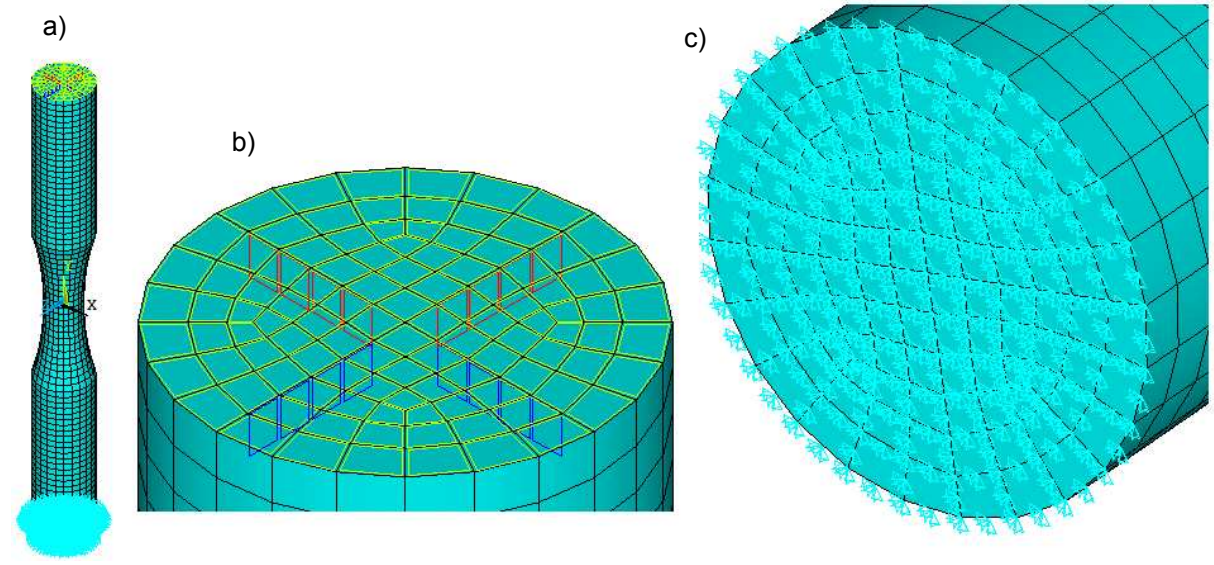

Figure 3.10 – Boundary conditions at the specimen a), top b) and bottom c)

The boundary conditions to be applied are calculated with the help of an excel spreadsheet which follows the general calculations described:

1. The input to the spreadsheet is the axial pressure in the smaller cross-sectional area A_a of the specimen P_a;
2. Knowing P_a, the force in A_a can be calculated by the equation:

$$F = P_a * A_a \quad (3.3)$$

3. The pressure is calculated at the top area of the specimen A_A to be applied as the axial boundary condition:

$$P_A = F/A_A \quad (3.4)$$

4. Knowing P_a, then the maximum shear pressure in the smaller cross-sectional area can be calculated by:

$$PS_a = P_a/\sqrt{3} \quad (3.5)$$

5. The applied torque in A_a is then given by:

$$T = PS_a/2 * J_a/(0.0075/4) \quad (3.6)$$

   where J_a is the polar moment of inertia.
6. Now the necessary shear pressure at the top of the specimen can be applied in the elements of figure 3.10 as a boundary condition:

$$PS_A = T/(0.003 * S_A) \quad (3.7)$$

Where 0.003 is the medium radius of the elements subjected to shear pressure and S_A the elements area where shear pressure is applied. Next the maximum shear and axial pressures calculated in the spreadsheet are used in the Matlab program to calculate the load path.

The general input file for ANSYS is presented in annex B.

3.5 Plasticity Program

The interaction with the Plasticity program was done programming new loads and changing material properties. The material properties to be introduced to this program are based on table 3.3 and table 3.6 and are presented in table 3.7 as program introduced variables. Units are as program units. Young modulus is of the AZ31B-F magnesium alloy.

Variable	Description	Value
Mat->E	Young modulus (MPa)	44800
Mat->KP	Proportional cyclic strength coefficient (MPa)	1976
Mat->np	Proportional cyclic hardening exponent	0.34
Mat->KP90	90 º Nonproportional cyclic strength coefficient (MPa)	2173.6
Mat->np90	90 º Nonproportional cyclic hardening exponent	0.34
Mat->nu	Poisson Coefficient	0.35
Mat->G	Shear modulus (MPa)	16592.5

Table 3.7 – Material properties of Plasticity C++ program

In table 3.7 it is assumed that the cyclic hardening exponent is constant for proportional and nonproportional loads. The 90º nonproportional cyclic strength is calculated supposing an Kanazawa nonproportionality constant as in equation 2.7 with a value $\alpha = 0.1$. The shear modulus is calculated by the classic equation presented in table 2.3.

3.6 Matlab Programming of Damage Parameters

Damage parameters are programmed in Matlab using various functions. The principal function or main program which calls the others is in Annex C. All the loads and criteria are programmed as functions so that it is possible to program a new load and apply the criterion that is wished. To do validation of the program, the case 1 of reference [16] with the steel CK45 material properties is tested. The results are presented in table 3.8. A von Mises maximum load of 1 MPa is used. A mesh of 41 points in time discretization and 91 points discretization in angles (between -90º and 90º) is used. By observing relative error, it can be concluded that the Matlab program is calculating angles with good accuracy (relative error < 13%). The error can be explained by the use of a different mesh in the mesh time vs angle discretization.

Damage Parameter	Ref. [16]	Matlab	Relative Error (%)
Findley	-18/66	-18/66	0/0
Brown & Miller	-18/66	-18/66	0/0
Fatemi & Socie	-18/66	-16/64	-12.5/-3.125
SWT	+25	25	0
Liu I	+25	25	0
Liu II	-21/69	-20/70	-5/1.43

Table 3.8 – Matlab critical plane angle results validation using the CK45 steel (degrees)

Since validation of damage parameters is done, the different parameter values for the ANSYS and Plasticity program loadings cases ($\sigma_{von\ Mises,max} = 204\ MPa$) can be plotted. However Findley, Brown & Miller and Fatemi & Socie have constant in their damage parameter to be determined before calculating the respective damage parameters. For Brown & Miller the constant is determined doing $N_f \to \infty$ in equation 2.24. For Fatemi & Socie the constant value can be determined introducing in expression 2.27 the approximate number of life cycles given by the other parameters, i.e, around 1000 life cycles. Findley constant can be determined iteratively supposing a constant value and verifying if the fatigue life value is close to the range of the other damage parameters. So the calculated constants obtained are in table 3.9.

Constant of Damage Parameters	Value
Brown & Miller	0.321
Fatemi & Socie	0.231
Findley	0.15

Table 3.9 – Damage parameters constants

4 Results & Discussion

This chapter is divided in four sections. The first presenting the tensile test results, the second the stresses results with the focus made in stresses behavior and comparison between ANSYS and Plasticity program results. The third section shows the critical plane results for the loading cases and the final and fourth section the fatigue life results and plasticity work results for ANSYS simulation.

4.1 Tensile Test Results

The tensile test is done at a strain rate of 1 mm/minute. Two specimens (S1 and S2) are tested. The engineering stress vs strain curves obtained and the curve of figure 3.3 are presented in figure 4.1. As it can be seen the magnesium alloy of paper [29] has a similar behavior of the AZ31B-F alloy.

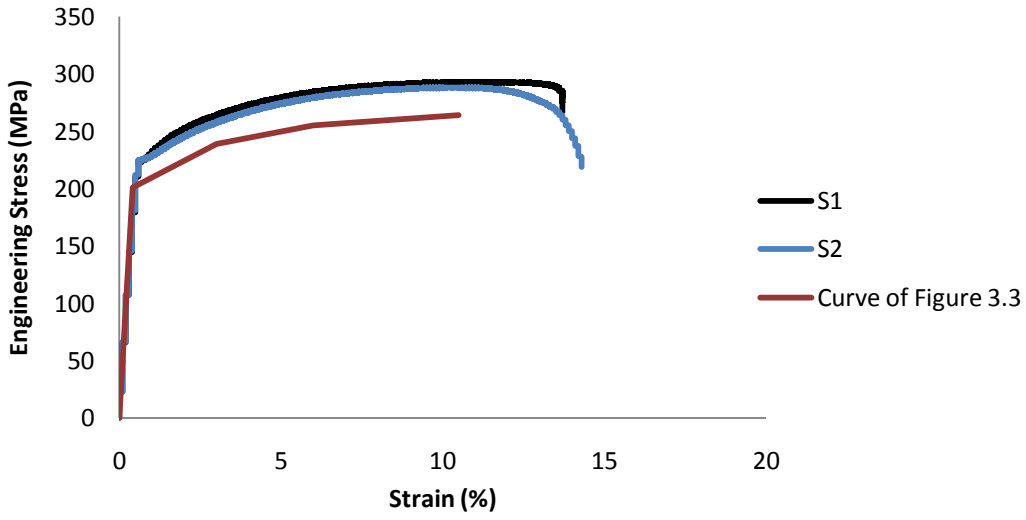

Figure 4.1 – Stress vs strain curves for tension tests and of ref. [29]

Table 4.1 lists the diameter and monotonic mechanical properties for the two tested specimens.

Specimen	Diameter (mm)	Yield Strenght (MPa)	Ultimate Tensile Strenght (MPa)	Elongation (%)	Young´s Modulus (GPa)	Fracture Tensile Strength (MPa)
S1	6.59	210	293	13.7	45	267
S2	6.29	209	288	14.3	45	219

Table 4.1 – Tensile test specimen diameter and monotonic mechanical properties of AZ31B-F alloy

Several photographs of the specimens were taken after fracture. Specimen 1 photos are presented in figure 4.2. The photos of specimen 2 are presented in figure 4.3.

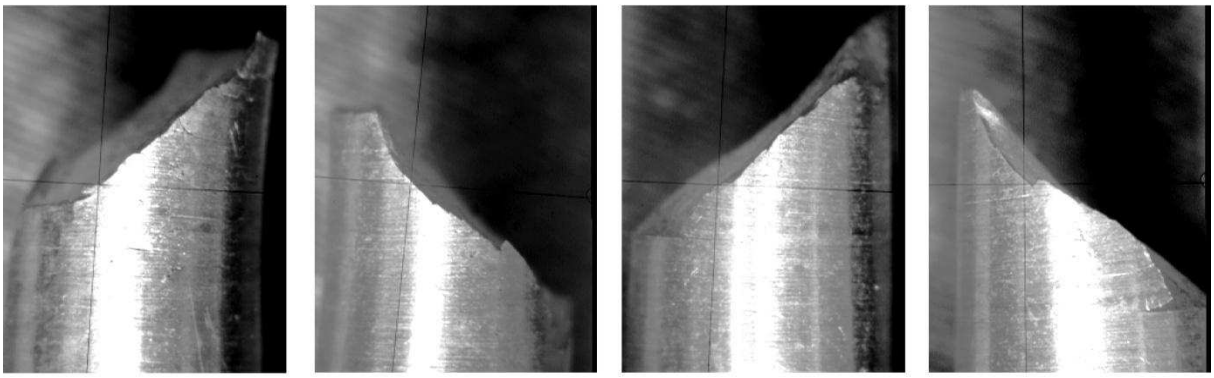

Figure 4.2 – Fracture angles of specimen S1; a) & b) side A; c) &d) side B

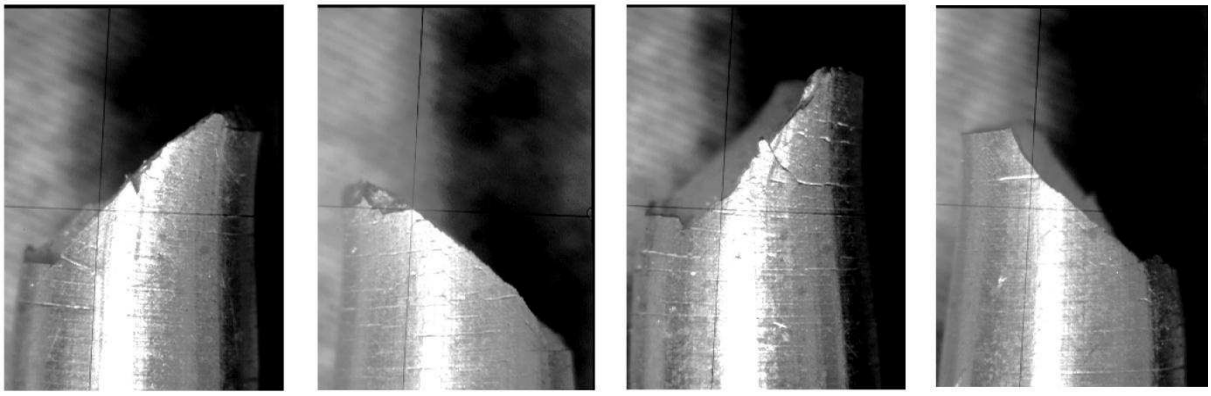

Figure 4.3 – Fracture angles of specimen S2; a) & b) side A; c) & d) side B

As it can be observed the general fracture angle is for both specimens around 45º, indicating a ductile fracture, which is in accordance with the high elongation (around 15%) and that ultimate tensile strength is around 50% higher than yield strength, showing a ductile behavior too.

4.2 Stress-Strain Results

In the next pages the results are presented for the stresses simulation using ANSYS and the plasticity model. ANSYS results are presented in parallel with Plasticity program results to compare more easily the obtained data. Both models represent real stress but they are based on different data as described in the previous chapter. A qualitative and quantitative comparison is searched. A variable suitable to preview fatigue life is searched. All the ANSYS results are obtained from the output file except the principal stresses angle. These ones are obtained using the equation 2.2. This equation is used to calculate principal stresses angle for Plasticity program results too. The ANSYS results are from node 3800 of specimen surface in the middle of the throat section. For the Plasticity program von Mises equivalent stress is calculated using the equation 2.4. The principal stresses are calculated for the Plasticity program using the equation A.6 (see annex A).

The ANSYS maximum von Mises stress used for each simulation at the boundary is presented in table 4.2.

Case	$\boldsymbol{\sigma}$ $(\boldsymbol{MPa})$
1	230
2	230
3	215
4	230
5	230
6	230
7	205
8	205

Table 4.2 – ANSYS maximum von Mises stress applied

The period of case 1 to case 6 loads is 0.1 s. The period of case 7 and case 8 loads is 1.4 s.

Plasticity program simulations need 3 s to run, to compute the data. ANSYS simulations for cases 1 to 6 need 1h40min to simulate 3 cycles. ANSYS simulation for cases 7 and 8 need 12h to simulate 1 cycle. So, only one cycle is simulated for cases 7 and 8 loads. Remember that the ANSYS hardening model doesn't have nonproportional effects as the Plasticity program.

From figures 4.4 to 4.19 the results for both ANSYS and Plasticity program are presented. In these figures the letters a), c), e) and g) correspond to ANSYS simulation results. The letters b), d), f) and h) correspond to Plasticity program results. Note that the second principal normal stress σ_2 is not presented because it is analyzed the stresses at a surface, so $\sigma_2 = 0$.

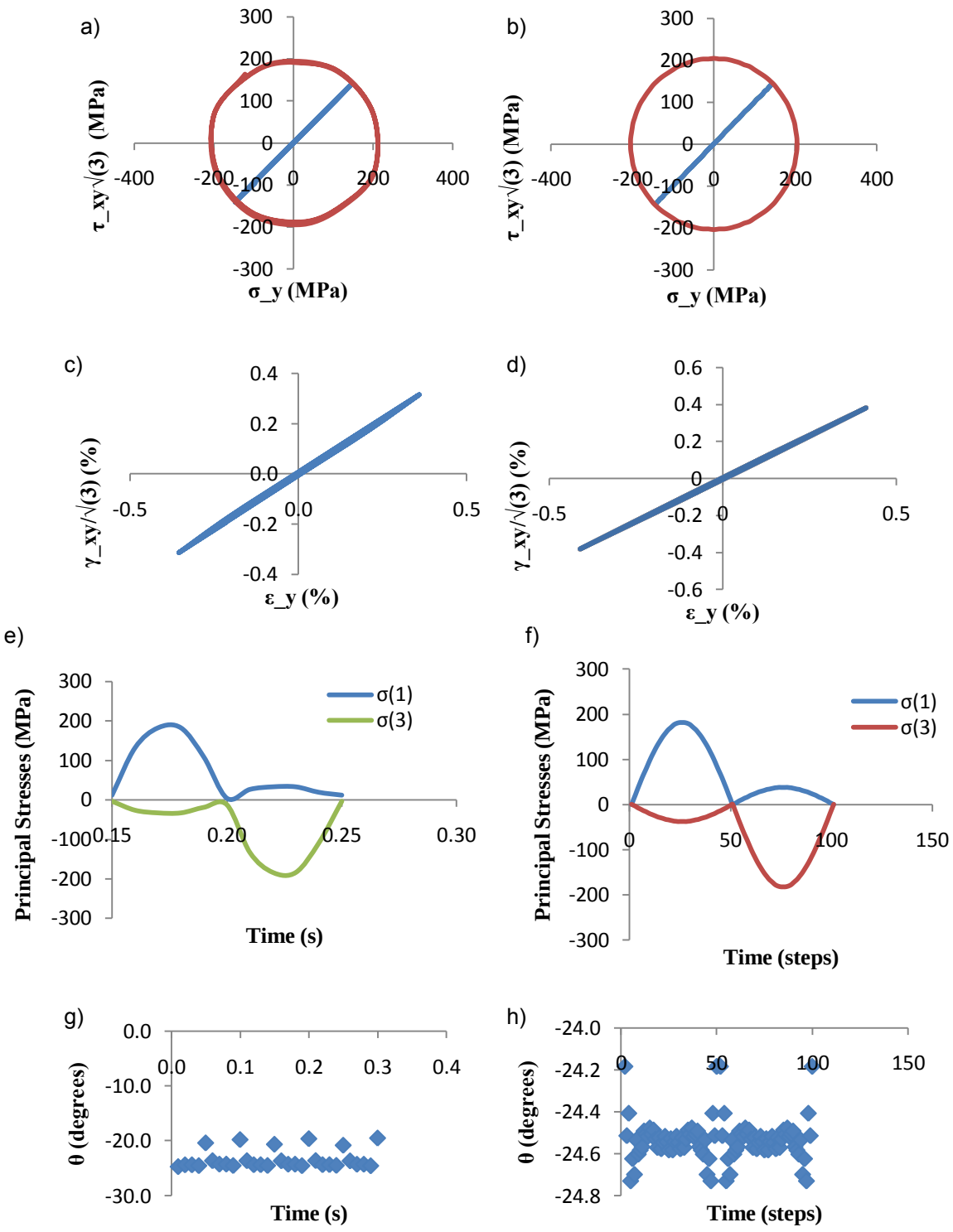

Figure 4.4 – Case 1 results: a) & b) shear stress*$\sqrt{3}$ vs axial stress, c) & d) shear strain/$\sqrt{3}$ vs axial strain, e) & f) principal stresses, g) & h) principal stresses plane angle

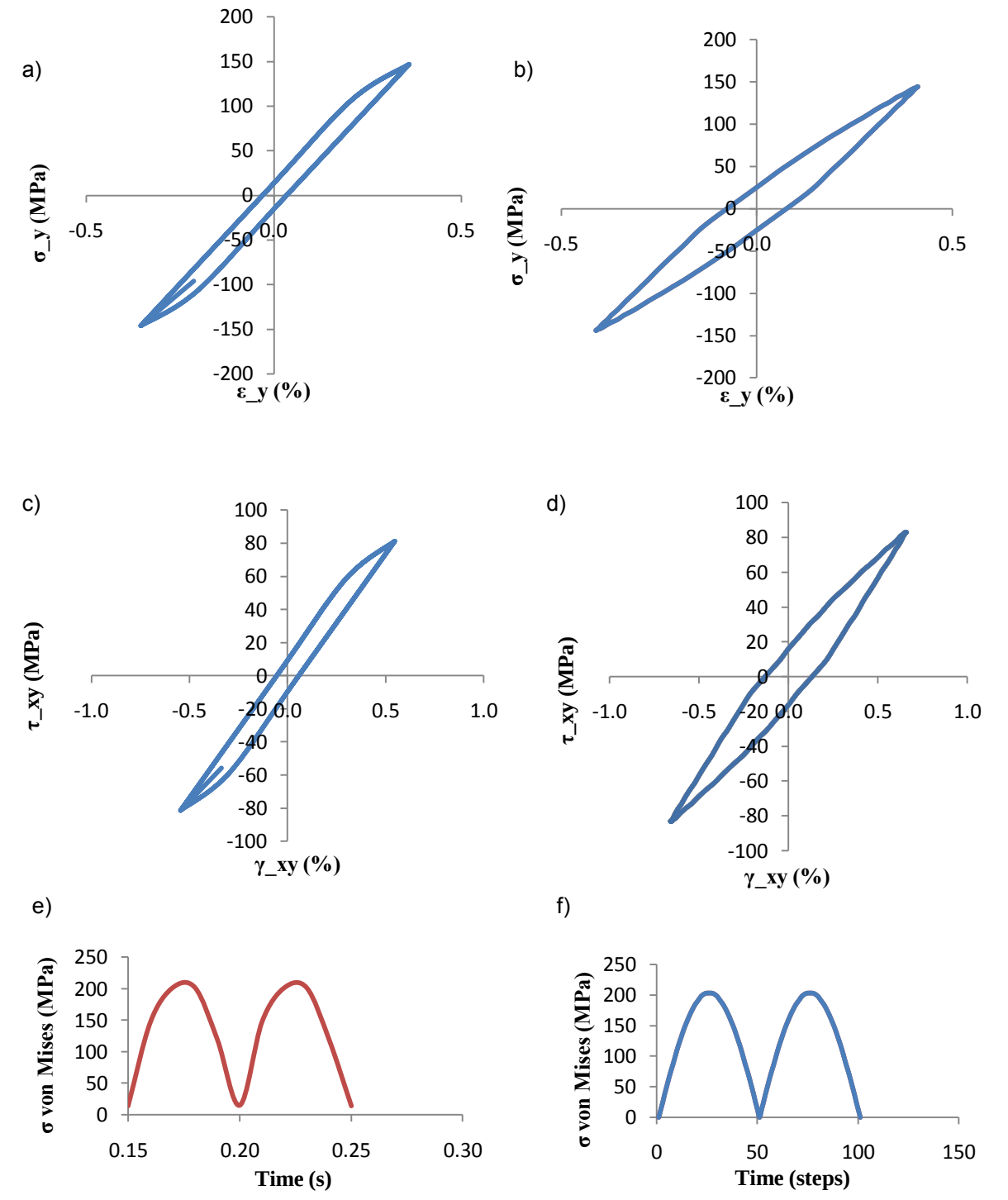

Figure 4.5 –Case 1 results: a) & b) axial stress vs axial strain, c) & d) shear stress vs shear strain, e) & f) von Mises stress

Case 1 results show similar behavior for both ANSYS and Plasticity program simulations as it was expected, i. e., since case 1 is a proportional loading. The range of stresses and strains is similar too.

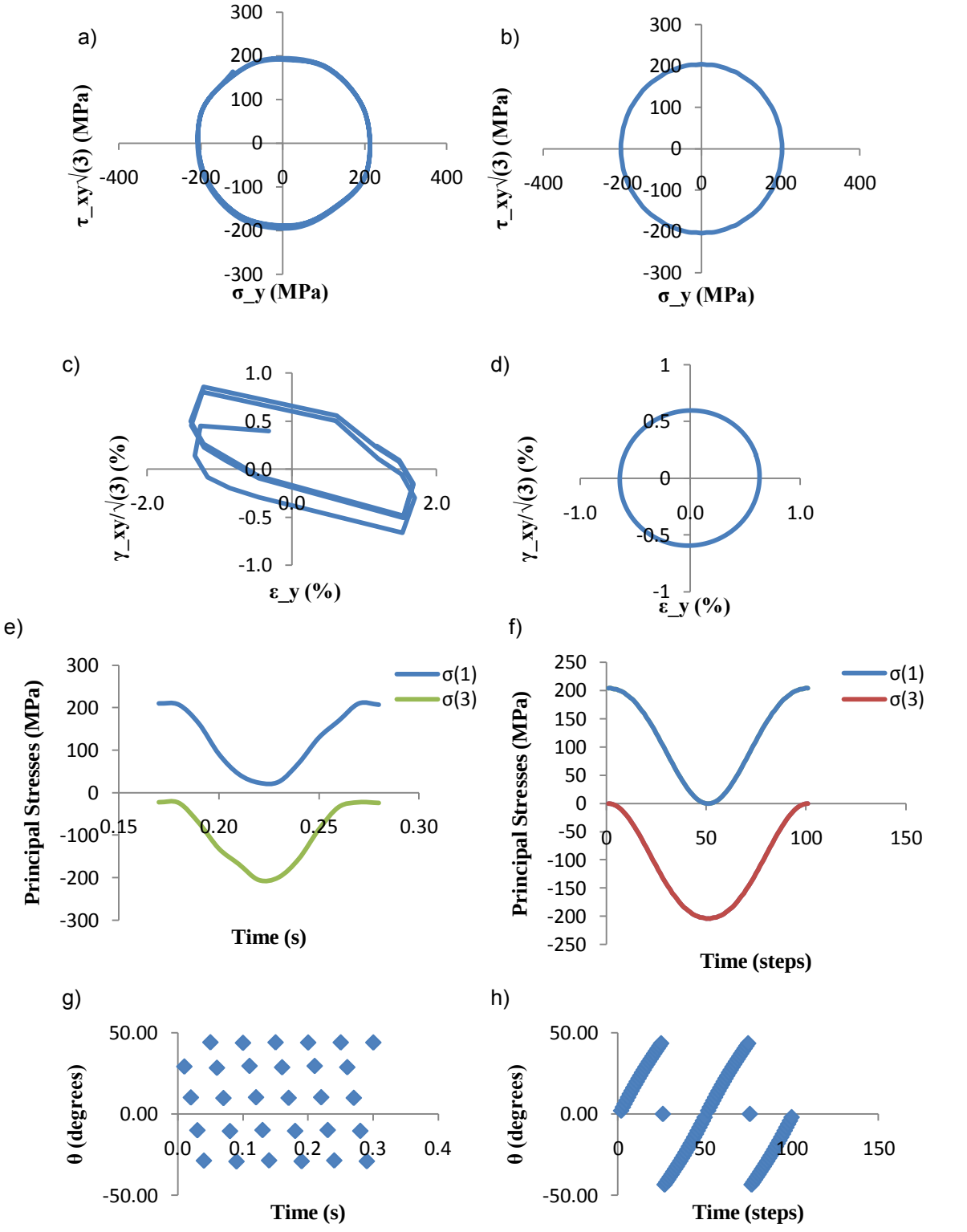

Figure 4.6 – Case 2 results: a) & b) shear stress*$\sqrt{3}$ vs axial stress, c) & d) shear strain/$\sqrt{3}$ vs axial strain, e) & f) principal stresses, g) & h) principal stresses plane angle

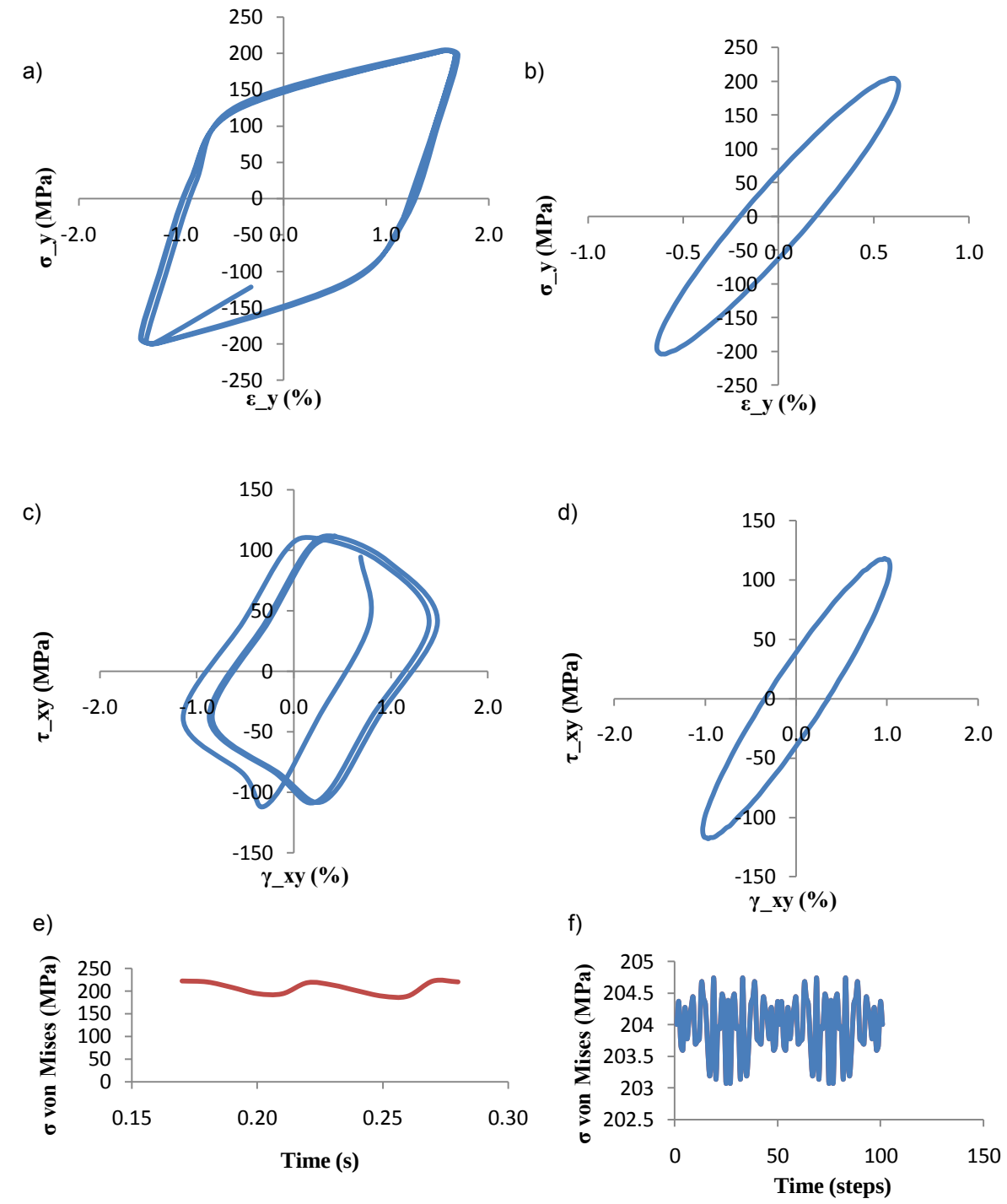

Figure 4.7 – Case 2 results: a) & b) axial stress vs axial strain, c) & d) shear stress vs shear strain, e) & f) von Mises stress

Case 2 results show similar behavior for both ANSYS and Plasticity program simulations except for the shear strain/$\sqrt{3}$ vs axial strain, axial stress vs axial strain and shear stress vs shear strain. In the hysteresis loop for both shear and axial modes loops it is observed that without nonproportional hardening effects, the work done by the material is greater, as it is observed for the ANSYS case. For the ANSYS axial stress vs axial strain, twice strains results are observed in comparison to Plasticity program. In the shear strain/$\sqrt{3}$ vs axial strain figures, the range of strains is very different. For the figures where similar behavior is found, variables have similar range.

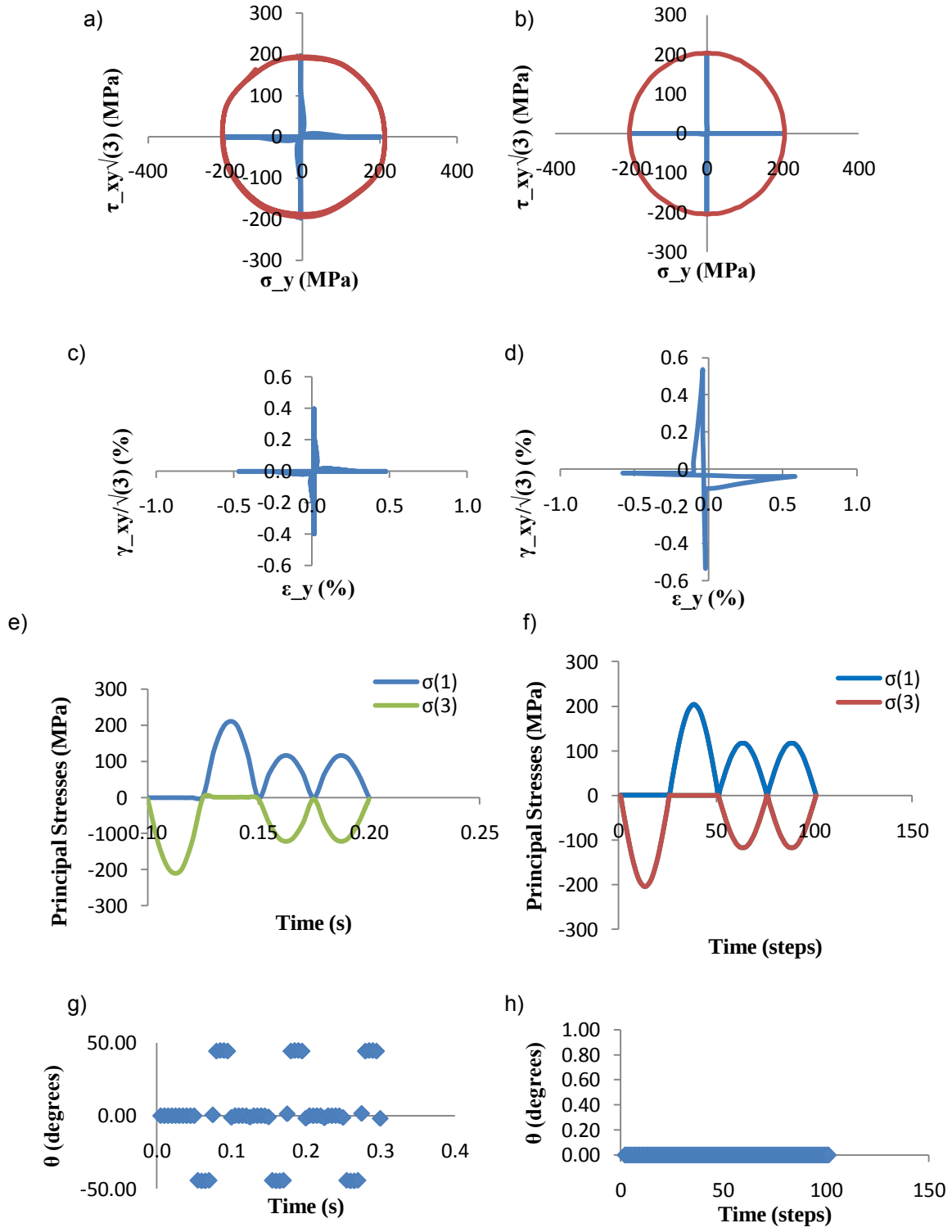

Figure 4.8 – Case 3 results: a) & b) shear stress*$\sqrt{3}$ vs axial stress, c) & d) shear strain/$\sqrt{3}$ vs axial strain, e) & f) principal stresses, g) & h) principal stresses plane angle

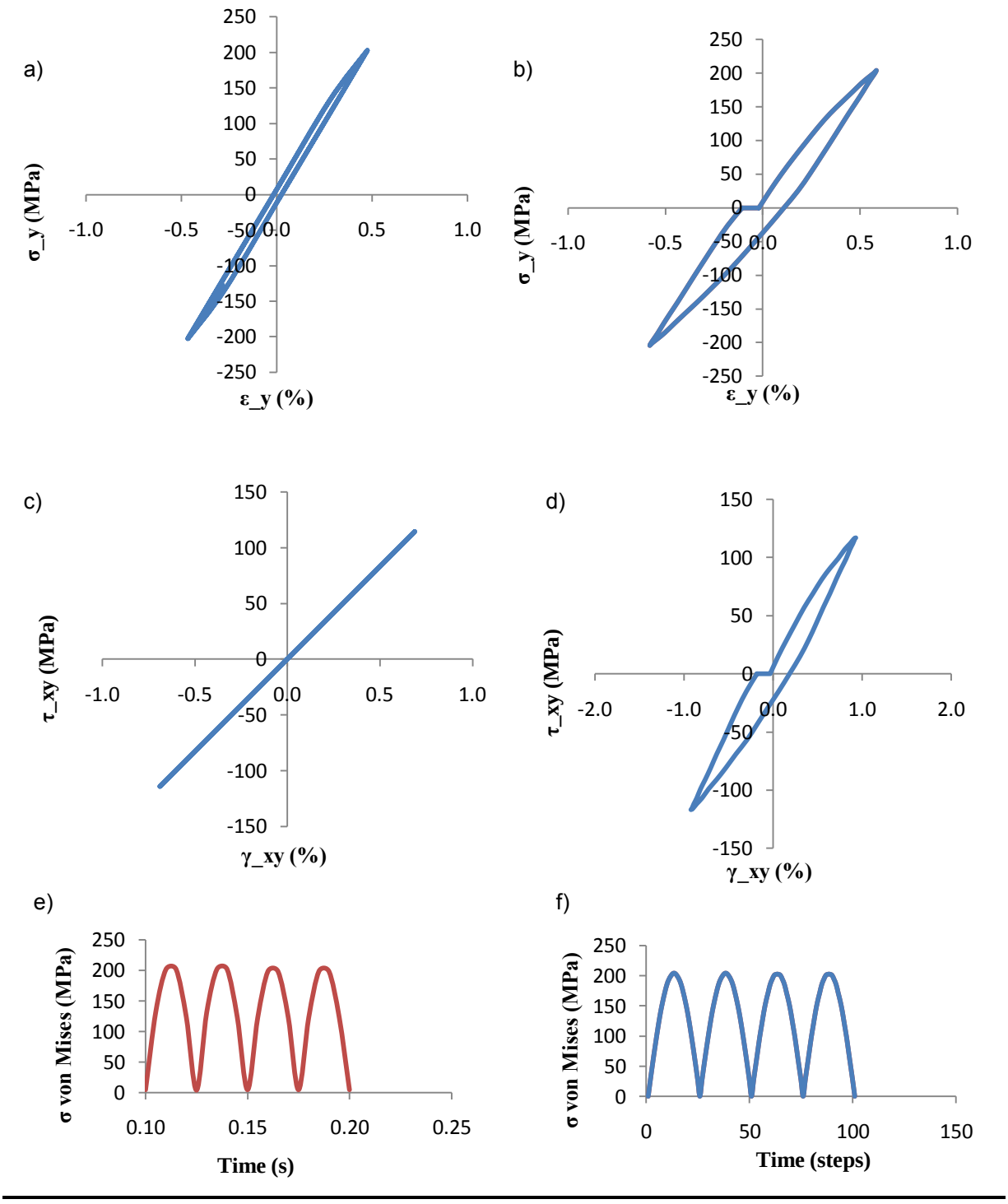

Figure 4.9 – Case 3 results: a) & b) axial stress vs axial strain, c) & d) shear stress vs shear strain, e) & f) von Mises stress

Case 3 results show similar behavior and stresses & strains ranges for both ANSYS and Plasticity program simulations only for shear stress*$\sqrt{3}$ vs axial stress, principal stresses and von Mises stress. The shear strain/$\sqrt{3}$ vs axial strain shows a similar behavior but different strains range. The principal stresses plane angle for ANSYS simulation shows that some angles near 50 degrees are traversed. The axial stress vs axial strain and shear stress vs shear strain figures show greater work results for Plasticity program. The ANSYS shear stress vs shear strain doesn't show plastic deformation.

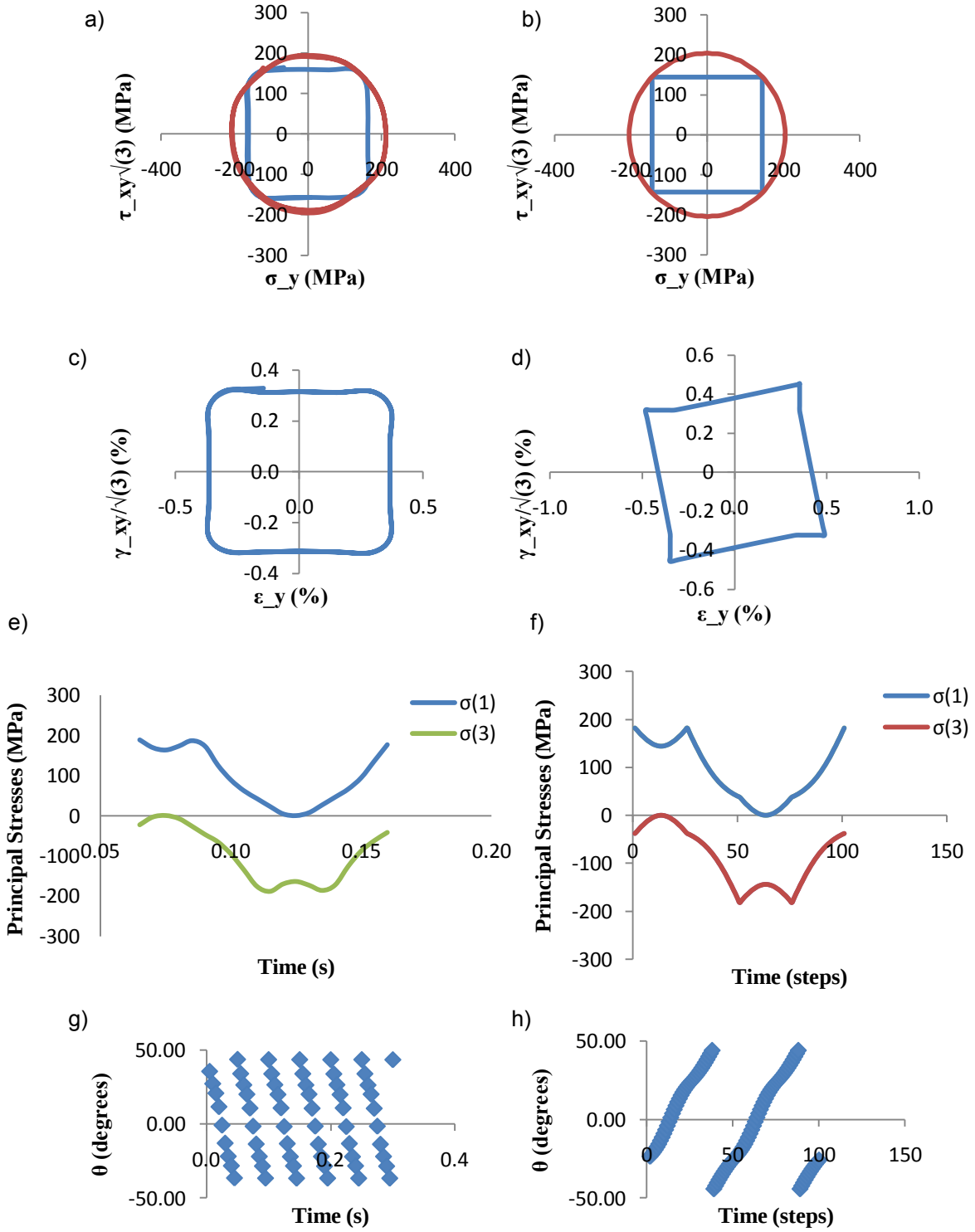

Figure 4.10 – Case 4 results: a) & b) shear stress*$\sqrt{3}$ vs axial stress, c) & d) shear strain/$\sqrt{3}$ vs axial strain, e) & f) principal stresses, g) & h) principal stresses plane angle

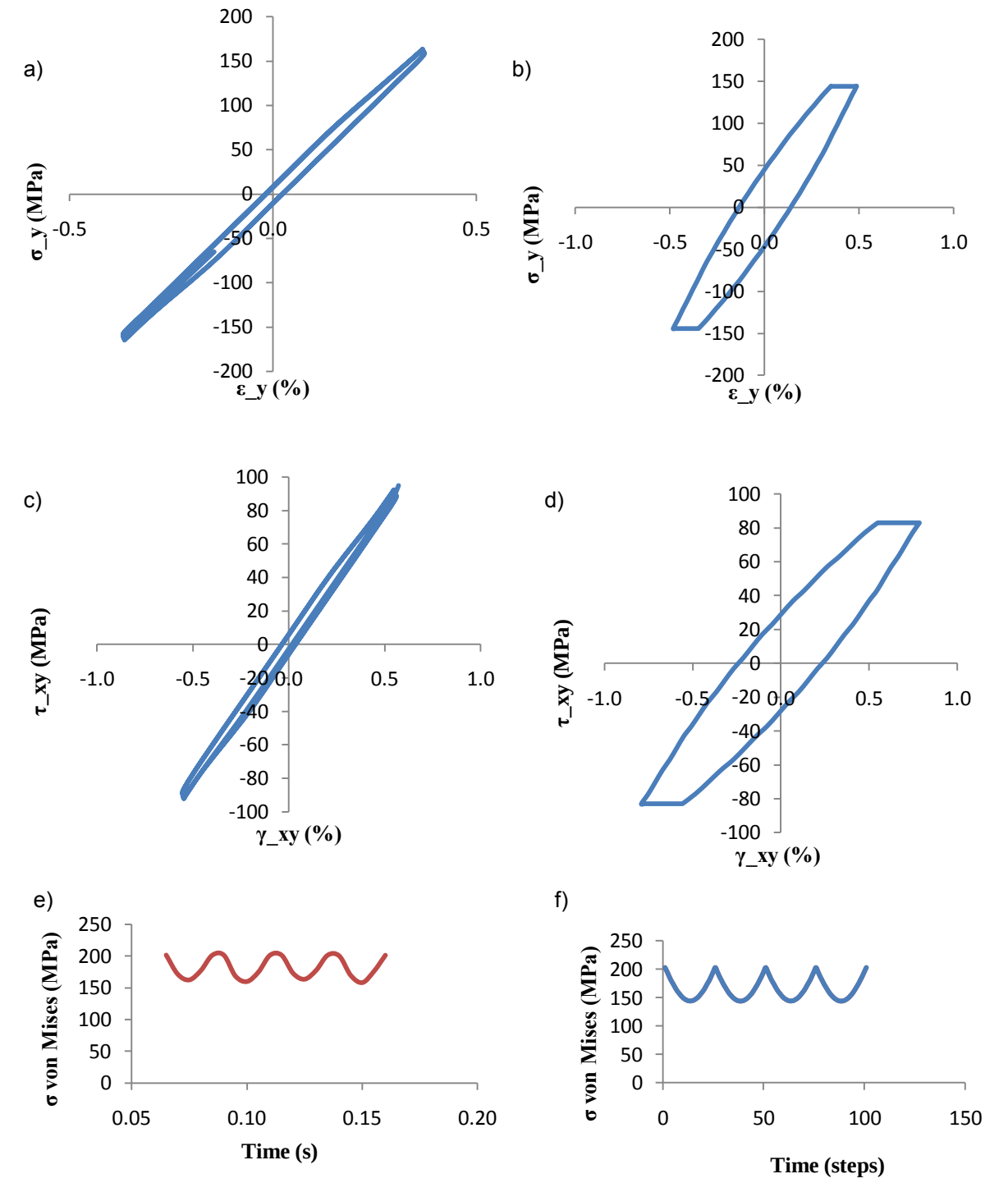

Figure 4.11 – Case 4 results: a) & b) axial stress vs axial strain, c) & d) shear stress vs shear strain, e) & f) von Mises stress

Case 4 results show similar behavior for both ANSYS and Plasticity program simulations except for the shear strain/$\sqrt{3}$ vs axial strain, axial stress vs axial strain and shear stress vs shear strain. In the hysteresis loop for both shear and axial modes loops it is observed that without nonproportional hardening effects, the work done by the material is lesser, as it is observed for the ANSYS case. In the shear strain/$\sqrt{3}$ vs axial strain figures the range of strains is similar but in the case of the Plasticity program it is observed a rotation of the loading path. For figures where similar behavior is found, variables have similar ranges.

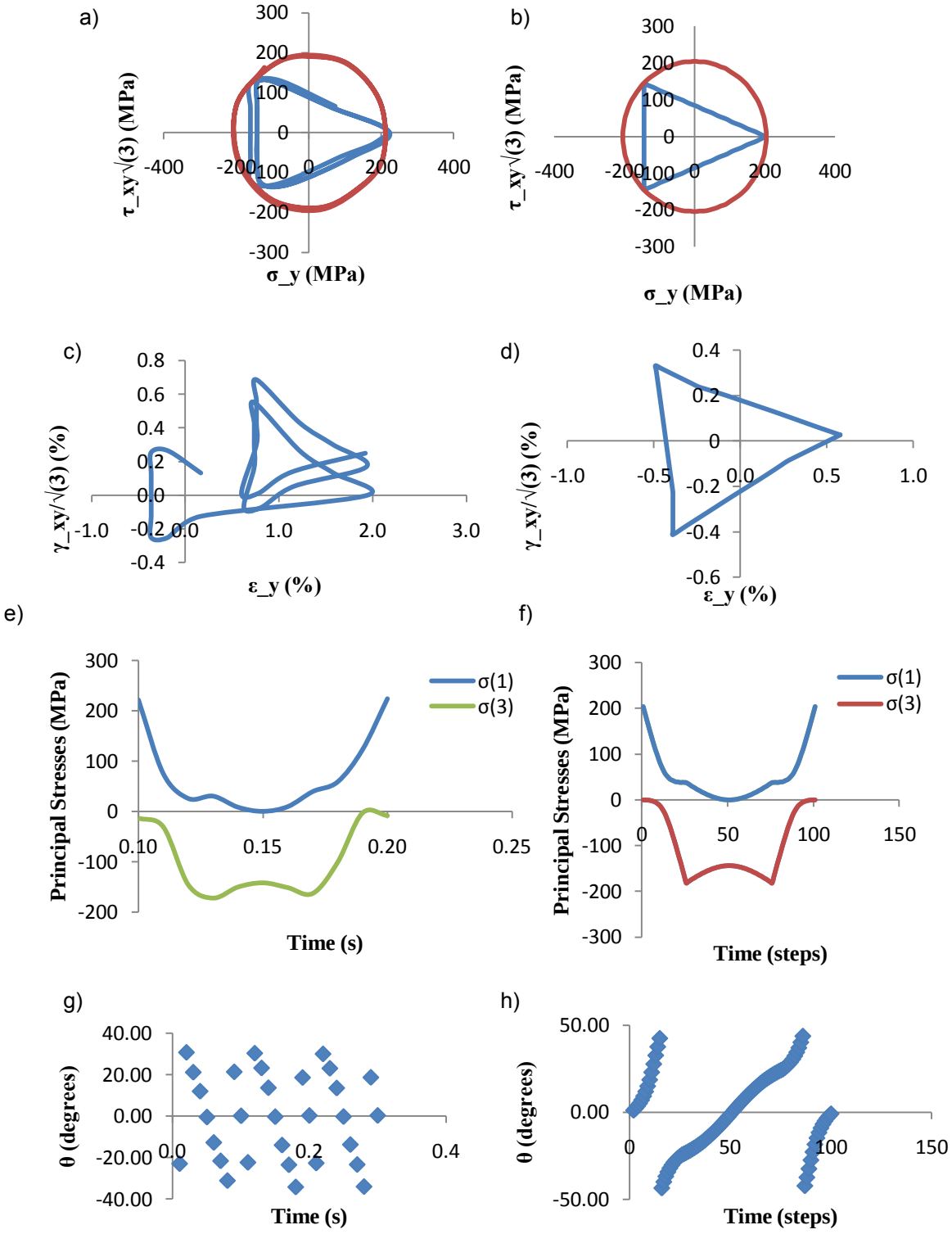

Figure 4.12 – Case 5 results: a) & b) shear stress*$\sqrt{3}$ vs axial stress, c) & d) shear strain/$\sqrt{3}$ vs axial strain, e) & f) principal stresses, g) & h) principal stresses plane angle

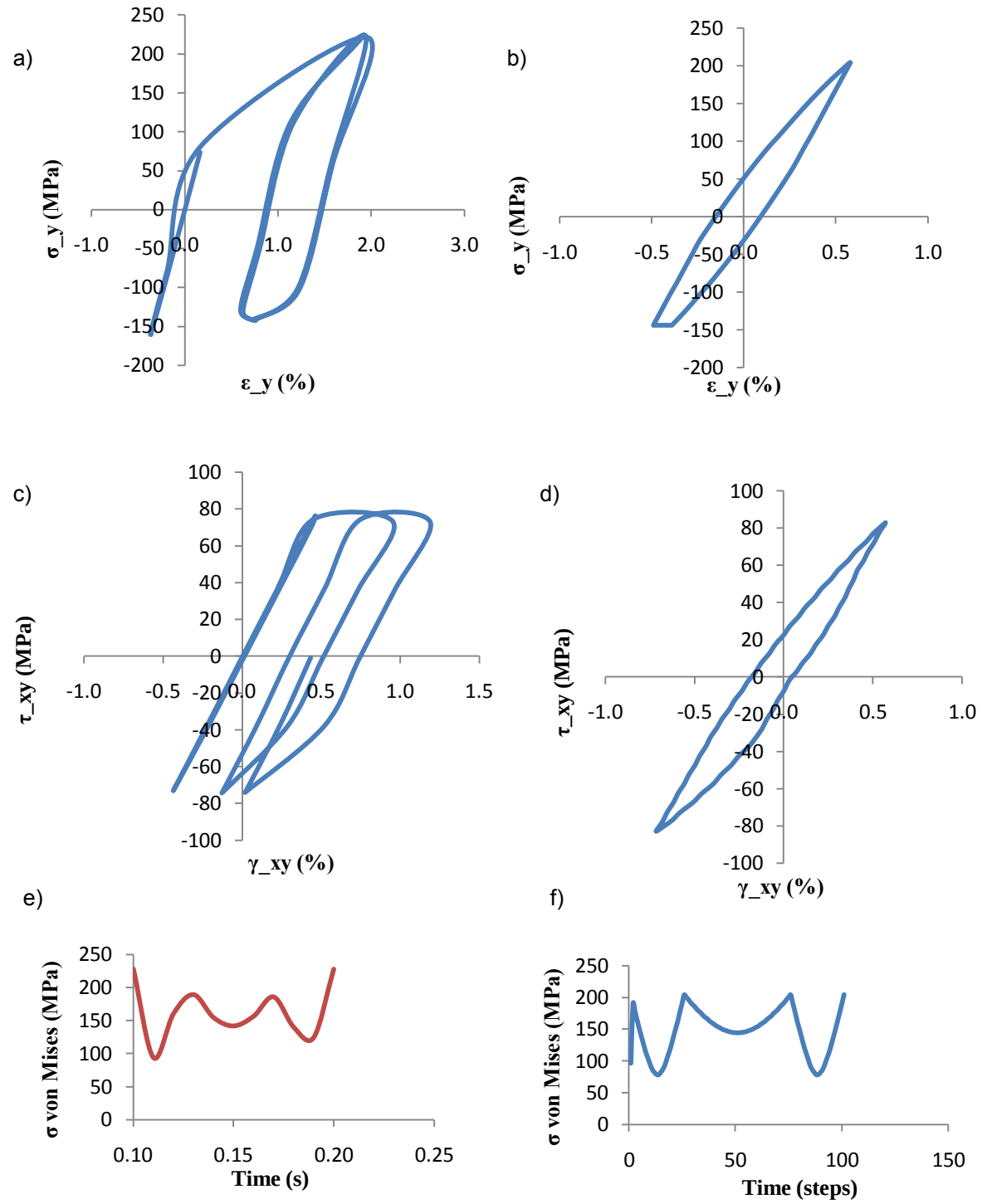

Figure 4.13 – Case 5 results: a) & b) axial stress vs axial strain, c) & d) shear stress vs shear strain, e) & f) von Mises stress

Case 5 results show similar behavior for both ANSYS and Plasticity program simulations except for the shear strain/$\sqrt{3}$ vs axial strain, axial stress vs axial strain and shear stress vs shear strain. The Plasticity program doesn't show a strains translation effect as it can be observed in the ANSYS results for the shear strain/$\sqrt{3}$ vs axial strain, axial stress vs axial strain and shear stress vs shear strain . However the range of values (max-min) for the cases mentioned before are similar. For figures where similar behavior is found, variables have similar ranges.

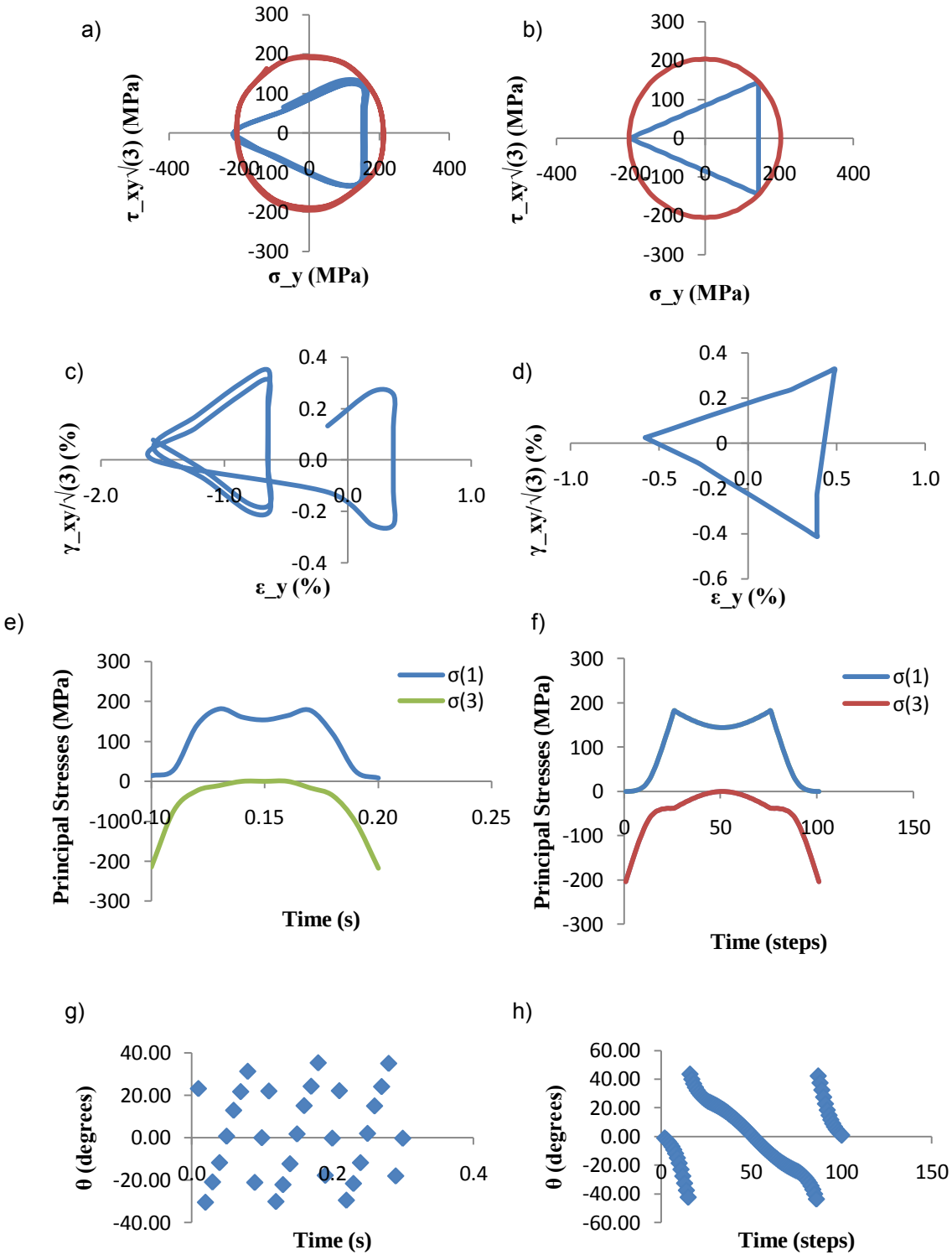

Figure 4.14 – Case 6 results: a) & b) shear stress*$\sqrt{3}$ vs axial stress, c) & d) shear strain/$\sqrt{3}$ vs axial strain, e) & f) principal stresses, g) & h) principal stresses plane angle

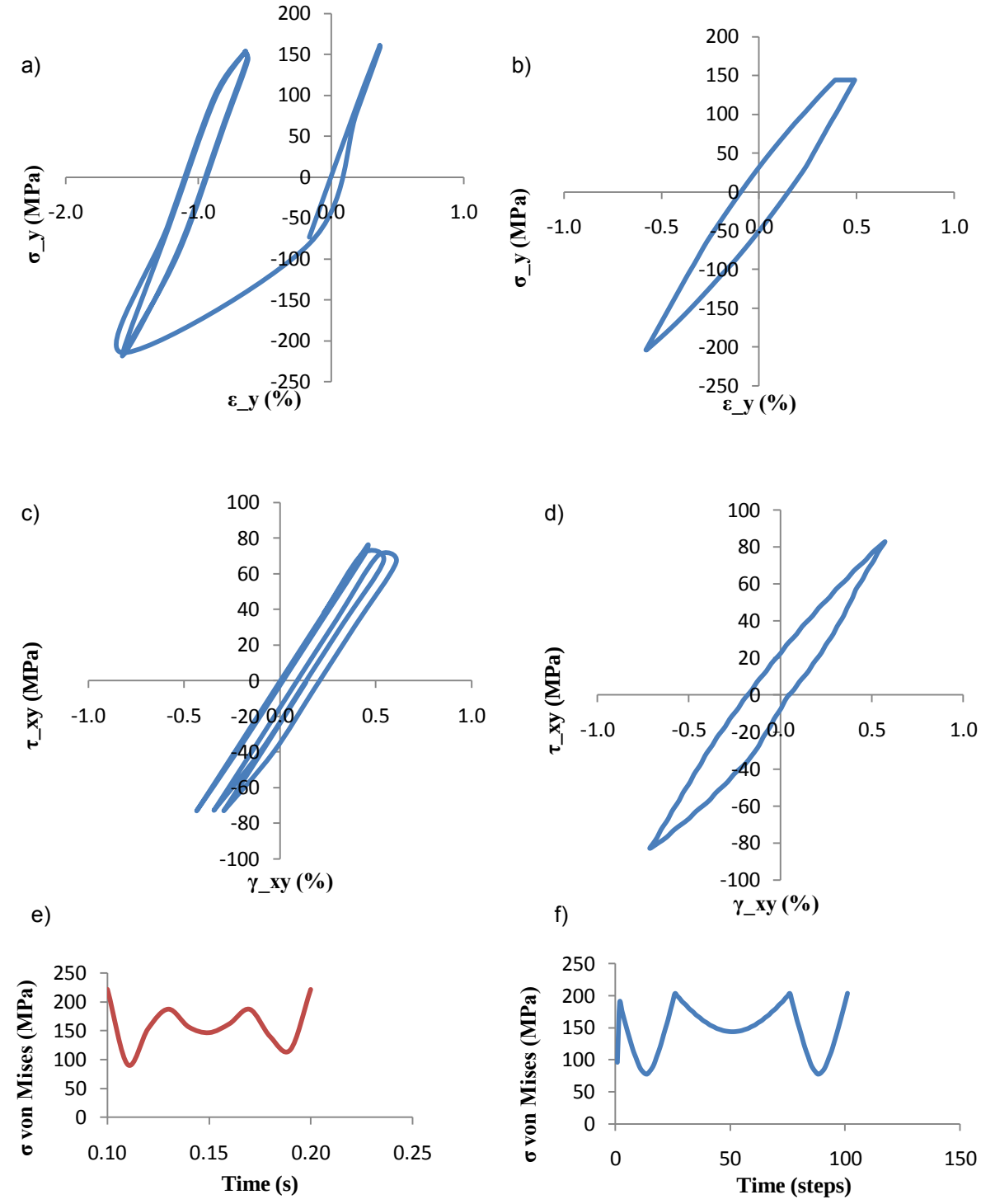

Figure 4.15 – Case 6 results: a) & b) axial stress vs axial strain, c) & d) shear stress vs shear strain, e) & f) von Mises stress

Case 6 results show similar behavior for both ANSYS and Plasticity program simulations except for the shear strain/$\sqrt{3}$ vs axial strain, axial stress vs axial strain and shear stress vs shear strain. The Plasticity program doesn't show a strains translation effect as it can be observed in the ANSYS results for the shear strain/$\sqrt{3}$ vs axial strain, axial stress vs axial strain and shear stress vs shear strain . However the range of values (max-min) for the cases mentioned before is similar. For the figures where similar behavior is found, variables have similar ranges.

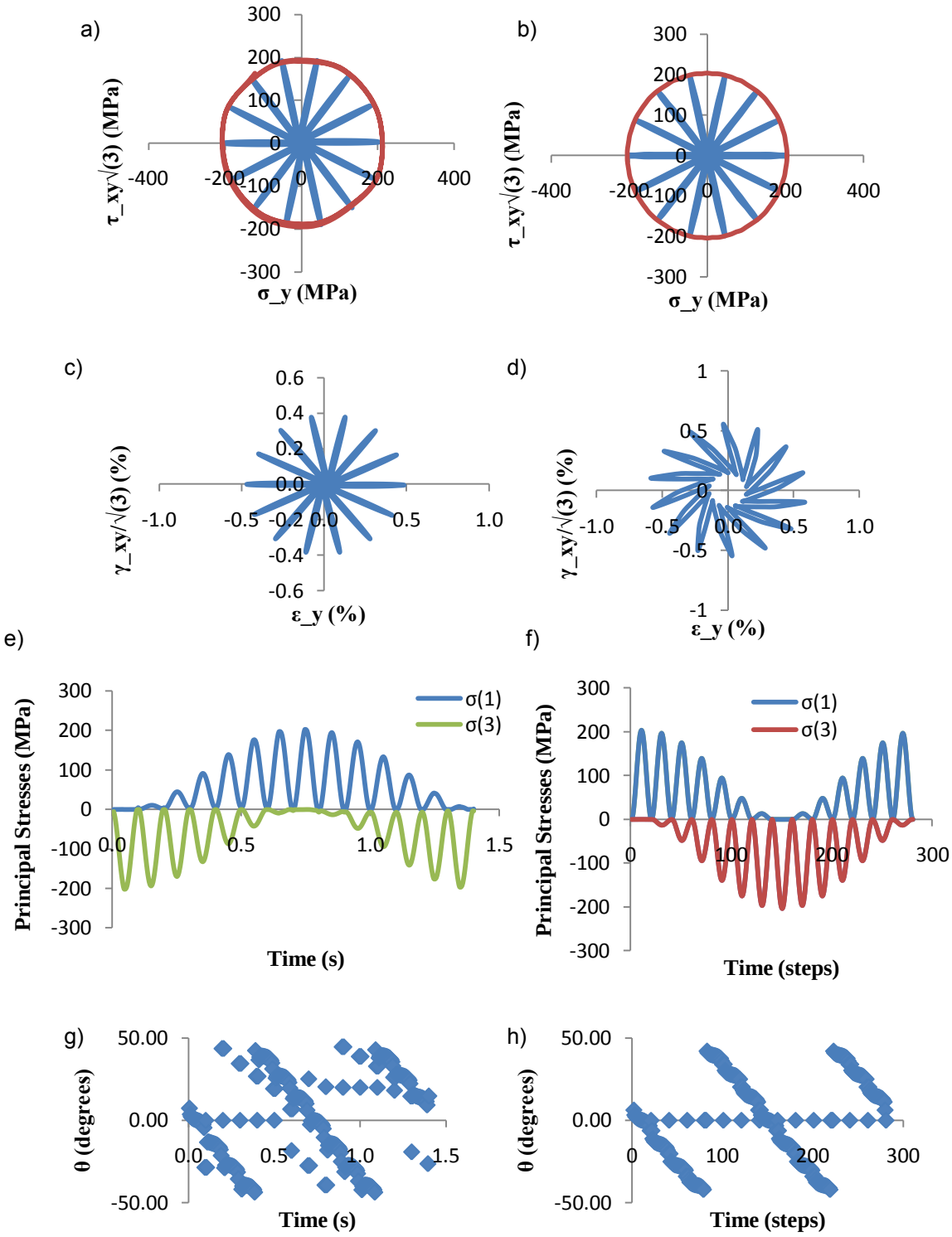

Figure 4.16 – Case 7 results: a) & b) shear stress*$\sqrt{3}$ vs axial stress, c) & d) shear strain/$\sqrt{3}$ vs axial strain, e) & f) principal stresses, g) & h) principal stresses plane angle

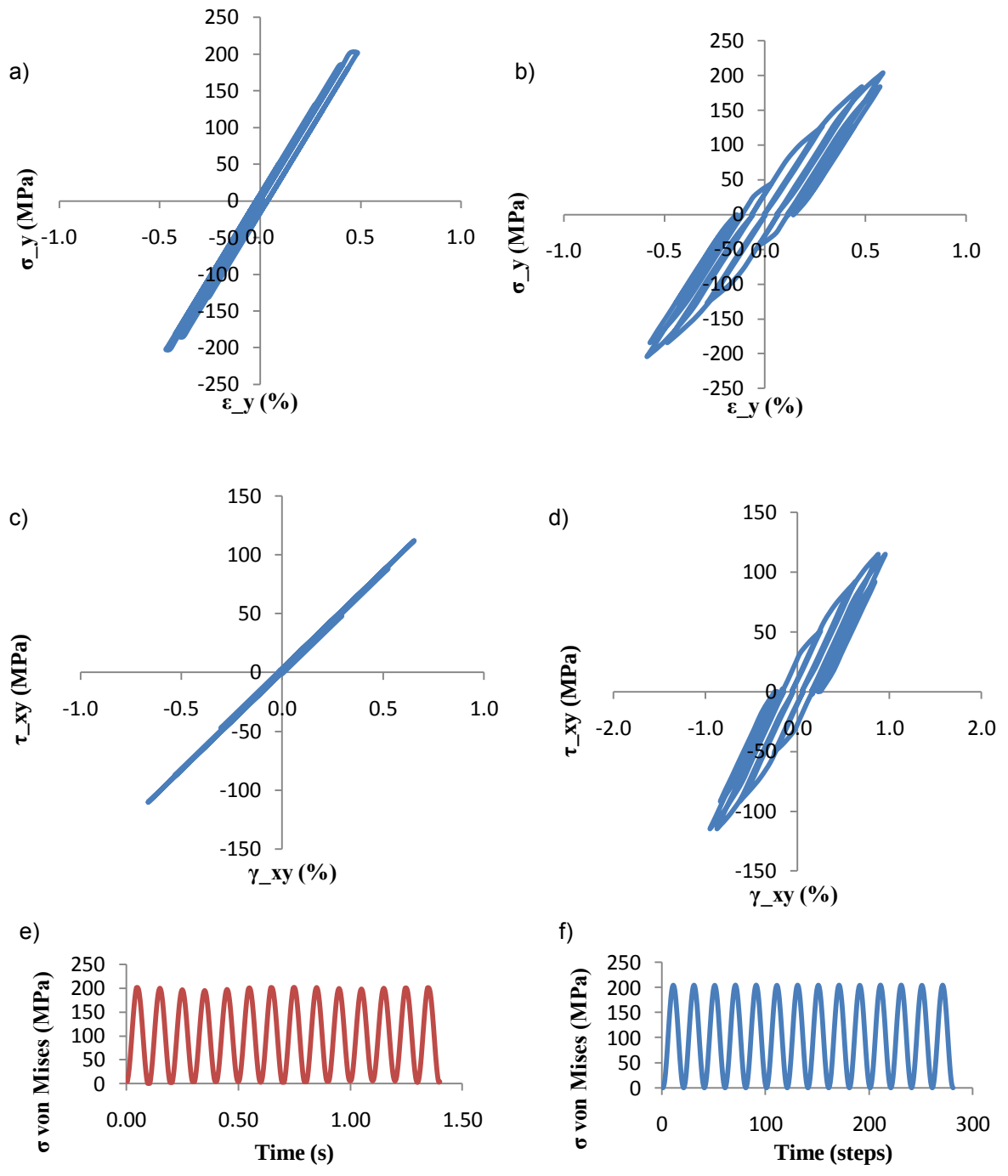

Figure 4.17 – Case 7 results: a) & b) axial stress vs axial strain, c) & d) shear stress vs shear strain, e) & f) von Mises stress

Case 7 results show similar behavior for both ANSYS and Plasticity program simulations except for the shear strain/$\sqrt{3}$ vs axial strain, axial stress vs axial strain and shear stress vs shear strain. In the hysteresis loop for both shear and axial modes loops it is observed that without nonproportional hardening effects, the work done by the material is greater for the Plasticity program case. In the shear strain/$\sqrt{3}$ vs axial strain figures, the range of strains is different. For figures that show similar behavior the results show the same ranges.

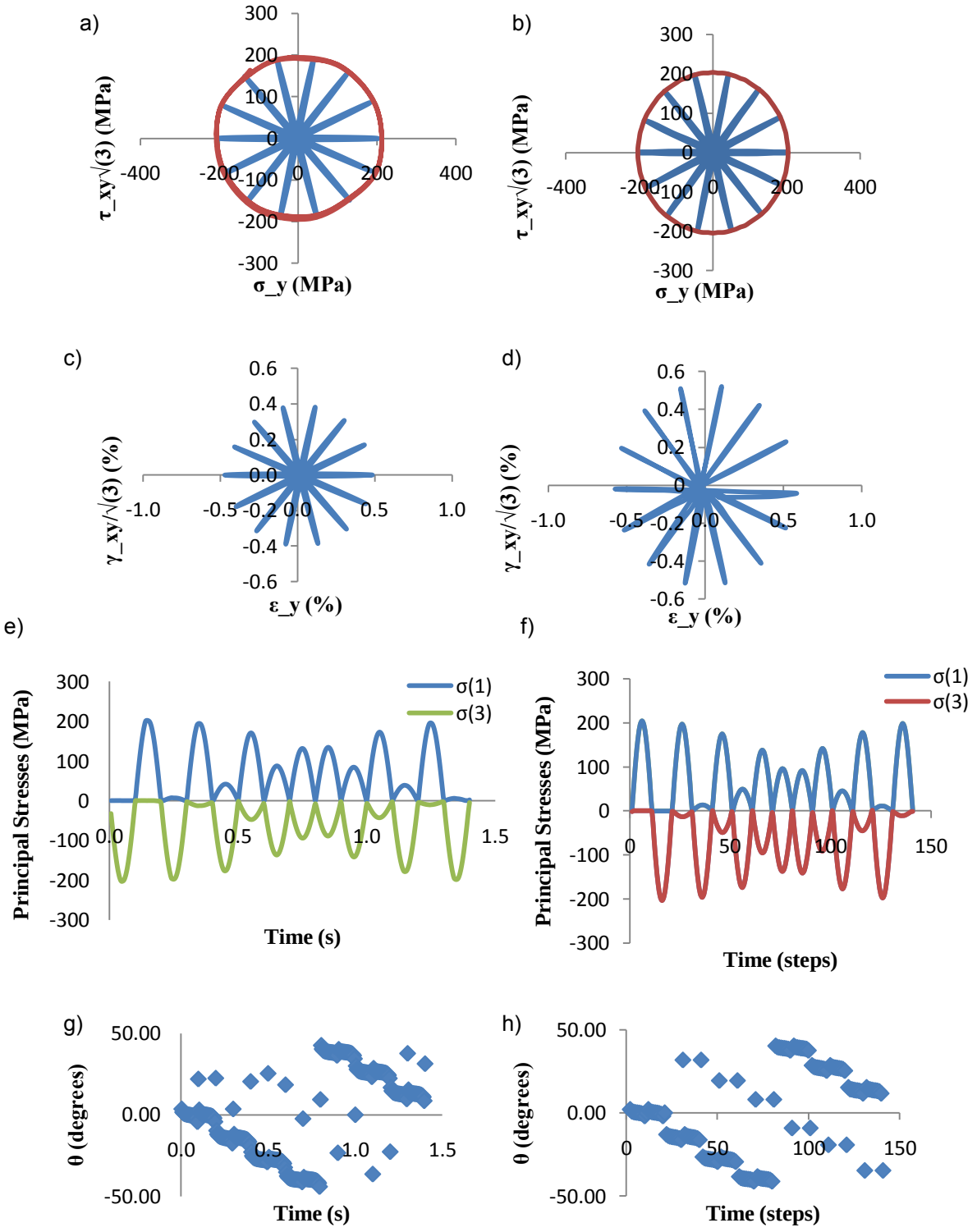

Figure 4.18 – Case 8 results: a) & b) shear stress*$\sqrt{3}$ vs axial stress, c) & d) shear strain/$\sqrt{3}$ vs axial strain, e) & f) principal stresses, g) & h) principal stresses plane angle

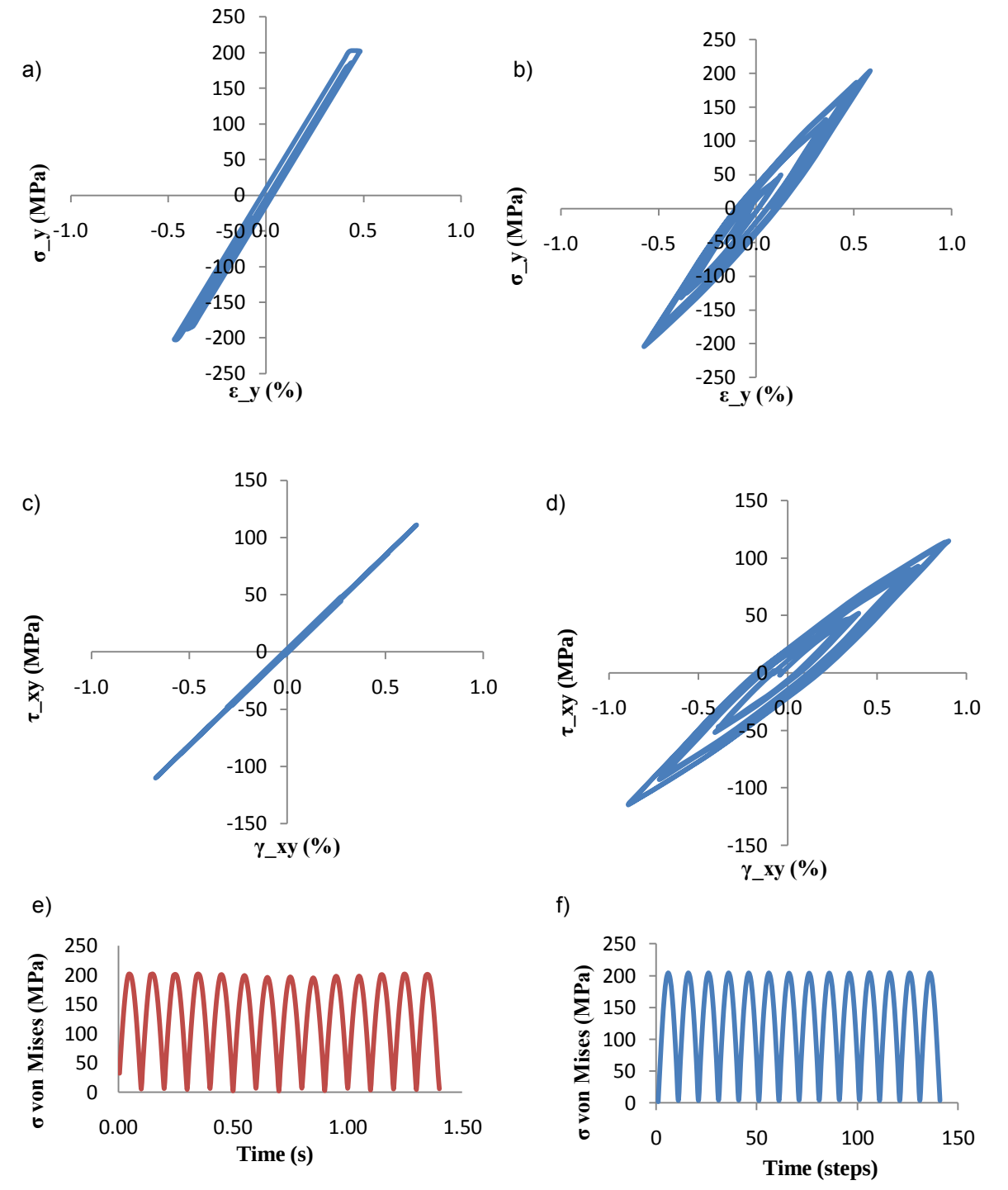

Figure 4.19 – Case 8 results: a) & b) axial stress vs axial strain, c) & d) shear stress vs shear strain, e) & f) von Mises stress

Case 7 results show similar behavior for both ANSYS and Plasticity program simulations except for the shear strain/$\sqrt{3}$ vs axial strain, axial stress vs axial strain and shear stress vs shear strain. In the hysteresis loop for both shear and axial modes loops it is observed that without nonproportional hardening effects, the work done by the material is greater for the Plasticity program case. In shear strain/$\sqrt{3}$ vs axial strain figures, the range of strains is different. For the figures that show similar behavior the results show the same ranges.

4.3 Critical Plane Results

The determined critical planes using a maximum von Mises stress of 204 MPa are presented in table 4.3 for the case of ANSYS loads. Critical planes for the cases of Plasticity program simulations are the same since the maximum von Mises stress applied is the same for all load cases.

Model	Findley	Brown & Miller	Fatemi & Socie	SWT	Liu I	Liu II
Case 1	-16/66	-12/60	-18/66	25	25	-20/70
Case 2	0	0	0	0	0	+-90/0
Case 3	0	0	0	0	0	+-90/0
Case 4	+-20	+-22	+-20	+-24	+-24	+-20/+-70
Case 5	+-28	+-28	+-30	+-8	+-12	+-58/+-32
Case 6	+-32	+-28	+-32	+-18	+-12	+-58/+-32
Case 7	+-4	+-4	+-6	0	0	+-84/+-6
Case 8	+-4	+-4	+-6	0	0	+-84/+-6

Table 4.3 – Critical plane angles (degrees)

In figures 4.20 to 4.25 the various damage parameters evolution is presented for all load cases.

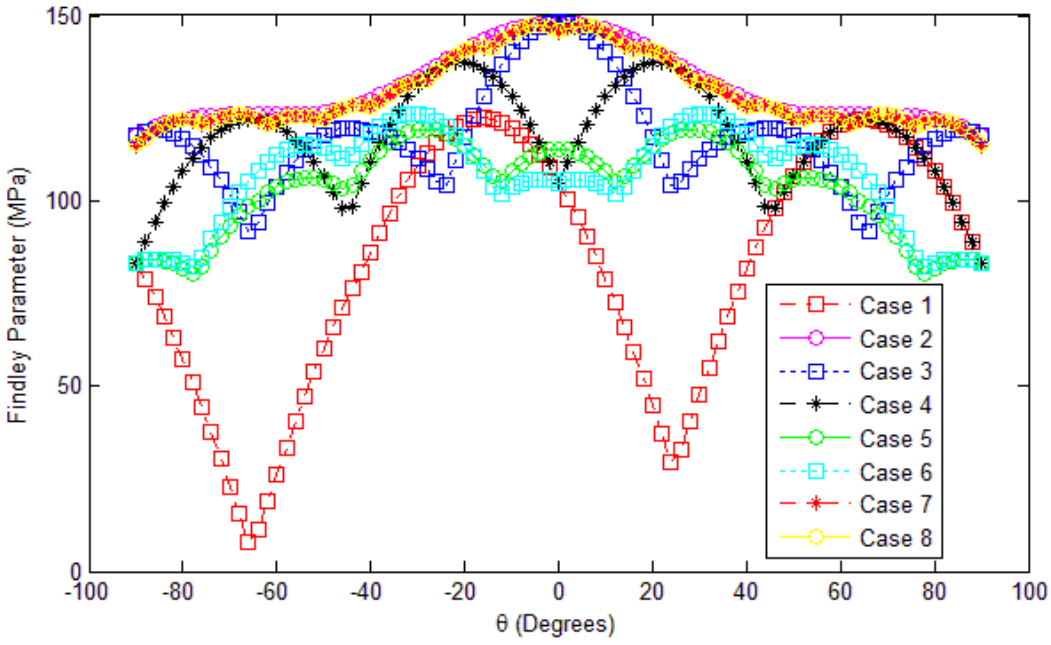

Figure 4.20 – Findley damage parameter

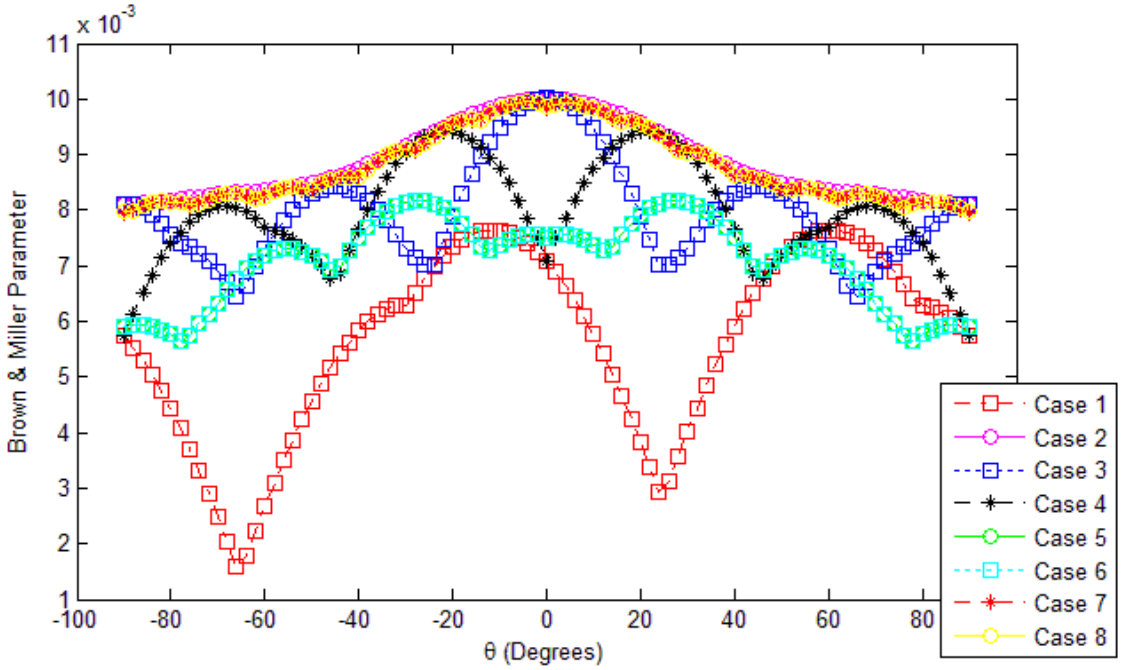

Figure 4.21 – Brown & Miller damage parameter

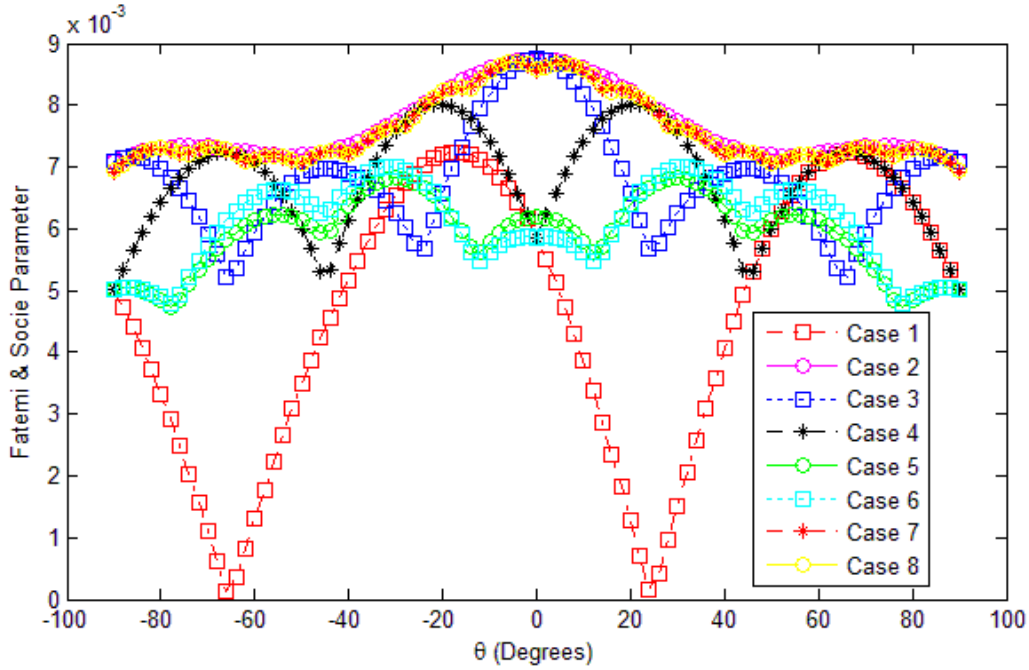

Figure 4.22 – Fatemi & Socie damage parameter

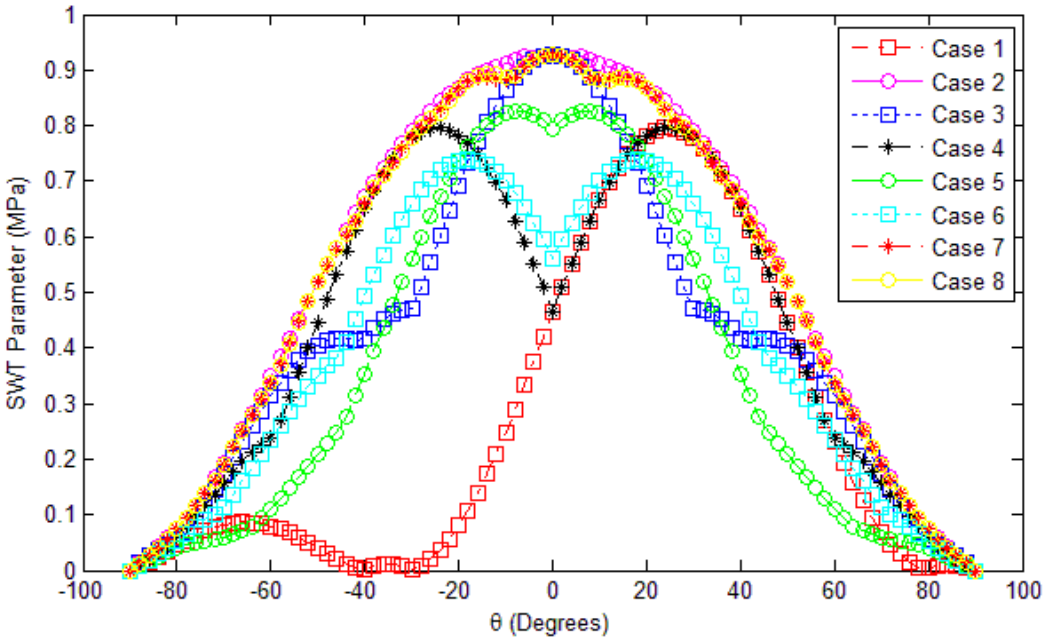

Figure 4.23 – SWT damage parameter

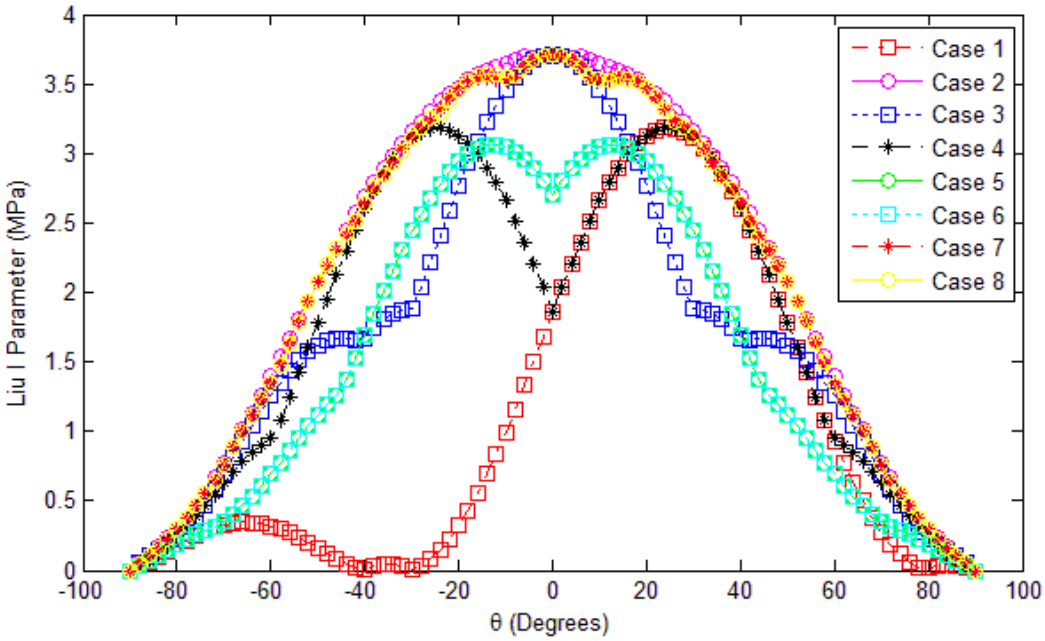

Figure 4.24 – Liu I damage parameter

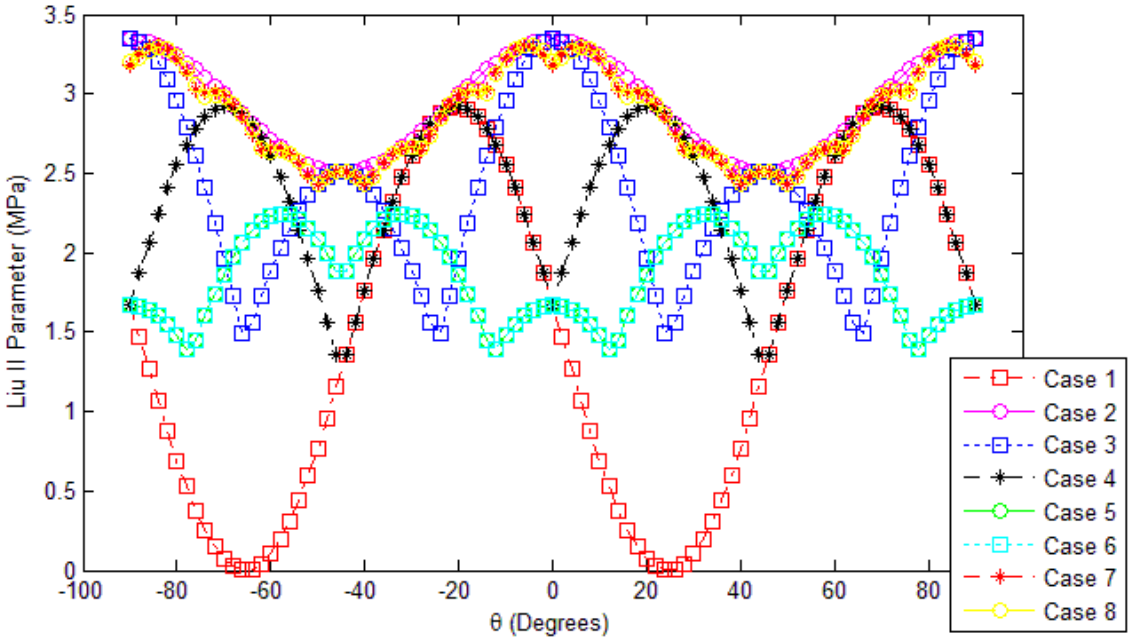

Figure 4.25 – Liu II damage parameter

As it can be seen in figures 4.20 to 4.25 the damage parameters of Findley, Brown & Miller, Fatemi & Socie and Liu II show similar behavior for the different loading cases. This happens because in these damage parameters the term that has a higher contribution to the parameters corresponds to a shear mode, i. e., a shear stress range or shear strain range. The same is observed for the damage parameters of SWT and Liu I, but in this case the term that has a higher contribution to the parameters corresponds to an axial mode, i. e., a normal stress range or normal strain range.

4.4 Fatigue Life Results

The obtained fatigue life or life cycles number for the ANSYS and Plasticity load cases are presented in table 4.4 considering different damage parameters.

Fatigue Life	Findley	Brown & Miller	Fatemi & Socie	SWT	Liu I	Liu II	Minimum
Case 1	1332	1366	2084	2171	2171	2134	1332
Case 2	365	345	771	1370	1370	1439	345
Case 3	365	345	771	1370	1370	1439	345
Case 4	613	468	1215	2171	2171	2134	468
Case 5	1564	964	2869	1940	2440	4706	964
Case 6	1257	964	2473	2702	2440	4706	964
Case 7	383	358	804	1370	1370	1493	358
Case 8	383	358	804	1370	1370	1493	358

Table 4.4 – Life cycles number results

The plasticity work obtained in ANSYS for each loading case is illustrated in figures 4.26 and 4.27.

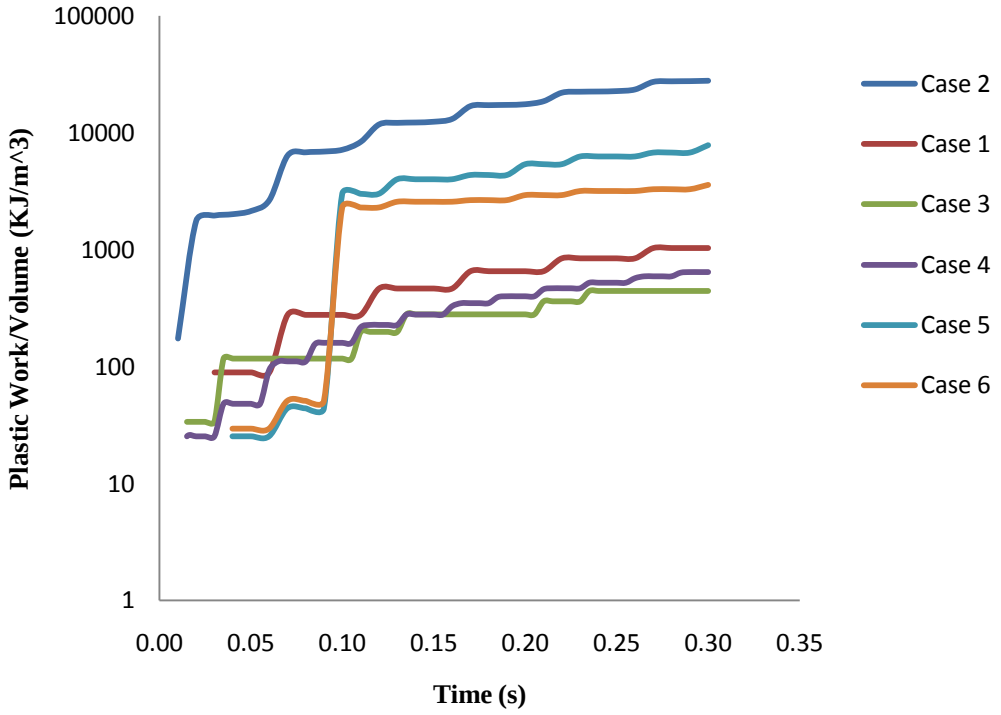

Figure 4.26 – Plastic work/volume for the ANSYS cases 1 to 6 simulations

Observing figure 4.26 it can be seen that the load that causes more plastic work is the case 2 and the load that causes less plastic work is the case 3. There is a high difference in the work done by these two cases (100x).

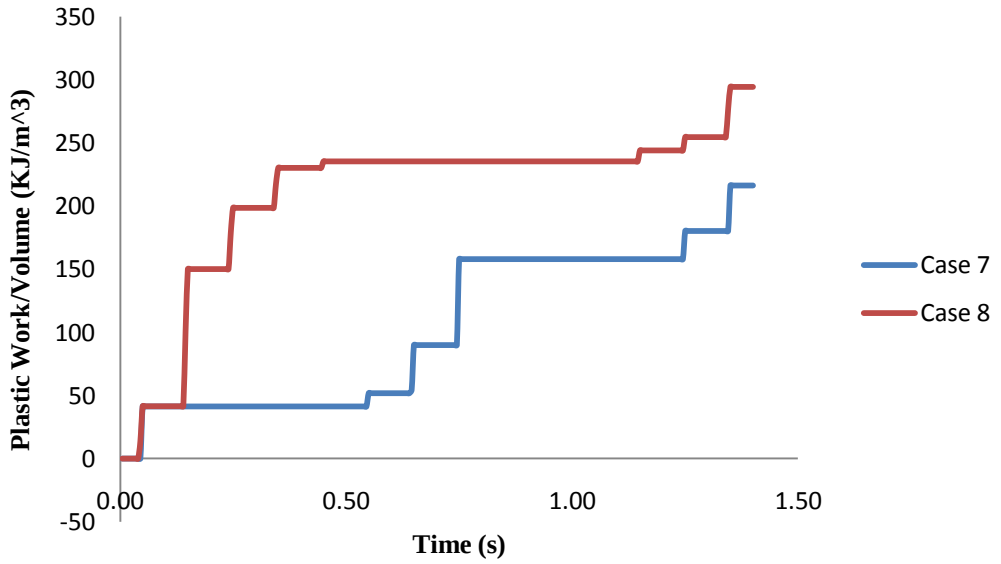

Figure 4.27 – Plastic work/volume for the ANSYS cases 7 and 8 simulations

Observing figure 4.27, it can be seen that case 8 causes more plastic work to the material than case 7.

The cases that cause more plastic work are not necessarily the cases that have less fatigue life according to ANSYS results. This can be seen, for example, for cases 2 and 3 that have the same fatigue life but cause very different plastic work to the material.

5 Conclusion

From the stresses results it can be concluded that for proportional loads the Plasticity program provides very similar results to ANSYS. However for nonproportional loads all the results differ much except von Mises stress, principal stresses and principal stresses plane angle.

As described in section 2.1, magnesium AZ31 alloys exhibit asymmetric hysteresis loops. The Plasticity program needs to be changed so that asymmetric hysteresis loop can be simulated. A method to introduce this asymmetric behavior in ANSYS needs to be searched too.

For the stresses results it is observed that for nonproportional loadings the material behavior results for ANSYS and Plasticity program are different. A method to include nonproportionality effects on ANSYS should be searched. Comparison of experimental results and the obtained data should be done. The plastic work observed for case 2 in ANSYS simulation results is higher than Plasticity program results. The opposite happens for case 4. The reason why this happens should be investigated with experiments.

All the damage parameters present a minimum fatigue life result for case 2 loading. However the maximum fatigue life result changes between cases 1, 5 and 6 for different damage parameters.

For loading case 2 and 3 all the damage parameters give equal results. This happens because damage parameters are based on stresses and strain ranges and they don't count the time the applied load is on a value that causes plastic strain. The same is observed for loading cases 7 and 8. To quantify the plastic strain caused by the time a loading path is on a value that causes plastic strain, an expression of type 5.1 should be investigated.

$$\frac{\overline{\sigma_{von\ Mises}}}{\sigma_{von\ Mises\ at\ yield}} \quad (5.1)$$

However this expression doesn't quantify the nonproportional hardening effects. This new von Mises expression is presented in figures 5.1 and 5.2 for all load cases. It can be observed that von Mises expression changes along the principal stresses plane angle θ. For loading cases 5 and 6 von Mises expression has the same values. The same happens for loading cases 7 and 8.

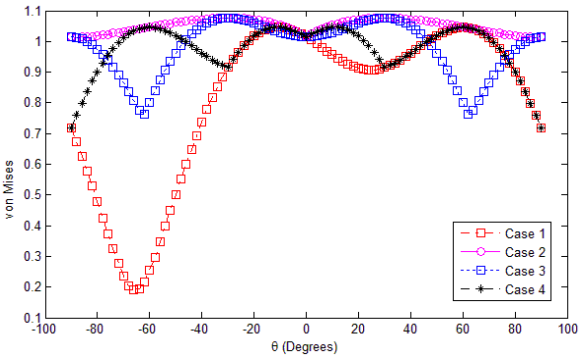

Figure 5.1 – von Mises expression for loading cases 1 to 4

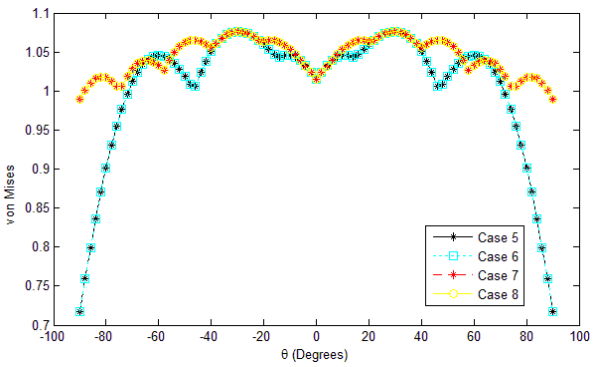

Figure 5.2 – von Mises expression for loading cases 5 to 8

A simple method to insert this expression in the damage parameters is multiplying the damage parameters defined by the expression 5.1. The critical plane results are presented in table 5.1 considering von Mises stress at yield, having a constant value for all the loading cases.

Model	Findley	Brown & Miller	Fatemi & Socie	SWT	Liu I	Liu II
Case 1	-14/64	-12/60	-16/64	25	25	-18/68
Case 2	+-10	+-10	+-10	+-10	+-10	+-6
Case 3	0	0	0	0	0	0/+-90
Case 4	+-18	+-18	+-18	+-20	+-20	+-18/+-90
Case 5	+-28	+-28	+-30	+-8	+-12	+-32
Case 6	+-30	+-28	+-32	+-20	+-12	+-32
Case 7	+-8	+-10	+-8	0	0	+-8
Case 8	+-8	+-10	+-8	0	0	+-8

Table 5.1 – Critical plane angles (degrees) for modified damage parameters

The fatigue life results are presented in table 5.2.

Fatigue Life	Findley	Brown & Miller	Fatemi & Socie	SWT	Liu I	Liu II	Minimum
Case 1	1023	1080	1714	2910	2910	2002	1023
Case 2	284	285	646	1235	1235	1324	284
Case 3	331	321	715	1311	1311	1378	321
Case 4	521	419	1074	2167	2167	2002	419
Case 5	961	664	1934	1708	2134	3780	664
Case 6	770	664	1678	2289	2134	3780	664
Case 7	292	294	656	1288	1288	1334	292
Case 8	292	294	656	1288	1288	1334	292

Table 5.2 – Life cycles number results for modified damage parameters

The fatigue life results change for cases 2 and 3 for the new damage parameters as expected. The loading case 2 shows less fatigue life than loading case 3. Experimental work needs to be done to study the possible application of this von Mises expression and how accurate it is.

6 References

[1] B. L. Mordike, T. Ebert. Magnesium Properties – applications – potential. Material Science and Engineering 2001; A302, p. 37-45

[2] Sp. G. Pantelakis, N. D. Alexopoulos, A. N. Chamos. Mechanical Performance Evaluation of Cast Magnesium Alloys for Automotive and Aeronautical Applications. Journal of Engineering Materials and Technology 2007; Vol.129, p. 422-430

[3] Elke Hombergsmeier. Magnesium for Aerospace Applications. EADS Deutschland Innovation Works 2007

[4] O. Pashkova, I. Ostrovsky, Y.Henn. Present State and Future of Magnesium Application in Aerospace Industry. New Challenges in Aeronautics Conference, Moscow, 2007

[5] T. David. The Principles of Magnesium Corrosion Protection. Presentation of Magnesium Elektron, 2004

[6] Internet Website Wikipedia. http://en.wikipedia.org/wiki/Galvanic_corrosion, 2010/09/01

[7] Internet Website RoyMech. http://www.roymech.co.uk/Useful_Tables/Corrosion/Cor_bi_met.html, 2010/09/01

[8] Internet Website Tagnite. http://www.tagnite.com/tagnite_coating/, 2010/09/01

[9] Internet Website Keronite. http://www.keronite.com/, 2010/09/01

[10] Internet Website MagForming. http://www.palbam.co.il/magforming/magforming_objectives.htm, 2010/09/01

[11] Internet Website MagForge. http://www.magforge.eu/, 2010/09/01

[12] Internet Website USCAR. http://www.uscar.org/guest/article_view.php?articles_id=38, 2010/09/01

[13] Internet Website Efunda. http://www.efunda.com, 2010/01/09

[14] United States Automotive Materials Partnership. Magnesium Vision 2020, 2006

[15] Norman E. Dowling. Mechanical Behavior of Materials. 3rd edition, 2007

[16] L. Reis. Comportamento Mecânico de Aços em Fadiga Multiaxial a Amplitude de Carga Constante e Síncrona 2004. PhD Thesis.

[17] Internet Website Advanced Magnesium Technologies and Solutions. http://www.magnesium-technologies.com/, 2010/09/05

[18] Internet Website Wikipedia, Alloy Wheel. http://en.wikipedia.org/wiki/Magnesium_alloy_wheel, 2010/09/06

[19] Internet Website Magnesium Elektron. http://www.magnesium-elektron.com, 2010/09/01

[20] K. Koski et al. . An aging aicraft´s wing under complex multiaxial spectrum loading: Fatigue assessment and repairing. International Journal of Fatigue 2006; Vol. 28, p. 652-656

[21] Yongming Liu et al. . Multiaxial fatigue reliability analysis of railroad wheels. Reliability Engineering & System Safety 2008; Vol 93, p. 456-467

[22] Internet Website Efatigue. Seminar Fatigue Made Easy. https://efatigue.com/seminars/, 2010/09/10

[23] W. Schütz. A History of Fatigue. Engineering Fracture Mechanics 1996; Vol 54, p. 263-300

[24] G. Perpétuo. Análise do efeito de carregamentos multiaxiais assíncronos na vida à fadiga no aço 42CrMo4, 2009

[25] V. Anes. Efeito da Sequência de Cargas Axial e de Torção na Previsão de Vida em Fadiga Multiaxial, 2009

[26] W. Henriques. Análise do dano acumulado devido a carregamentos multiaxiais na vida à fadiga no aço 42CrMo4, 2009

[27] L. Reis et al. . Simulation of cyclic stress/strain evolutions for multiaxial fatigue life prediction. International Journal of Fatigue 2006; Vol. 26, p. 451-458.

[28] S. Hasegawa et al. . Evaluation of low cycle fatigue life in AZ31 magnesium alloy. International Journal of Fatigue 2007; Vol. 30, p. 1839-1845

[29] S. Begum et al. . Low cycle fatigue properties of an extruded AZ31 magnesium alloy. International Journal of Fatigue 2009; Vol. 32, p. 726-735

[30] J. Albinmousa et al. . An energy-based fatigue model for wrought magnesium alloy under multiaxial load, The Ninth International Conference on Multiaxial Fatigue & Fracture, Parma, 2010

[31] L. Reis, B. Li and M. Freitas. Mean stress effect during stress/straining of 42CrMo4 structural steel. The Ninth International Conference on Multiaxial Fatigue & Fracture, Parma, 2010

[32] D. F. Socie, G. B. Marquis. Multiaxial Fatigue. SAE International, 2001

[33] Jiang, Y., and Sehitoglu, H. . “Modeling of Cyclic Ratcheting Plasticity, Part I: Development of Constitutive Equations. Journal of Applied Mechanics 1996; Vol. 63, pp 720-725

[34] Jiang, Y., and Sehitoglu, H. . “Modeling of Cyclic Ratcheting Plasticity, Part II: Comparison of Model Simulations with Experiments. Journal of Applied Mechanics 1996; Vol. 63, pp 726-733

[35] Catalogue of INSTRON 3360 machine, 2010

Annex A – 2D Stress State Equations

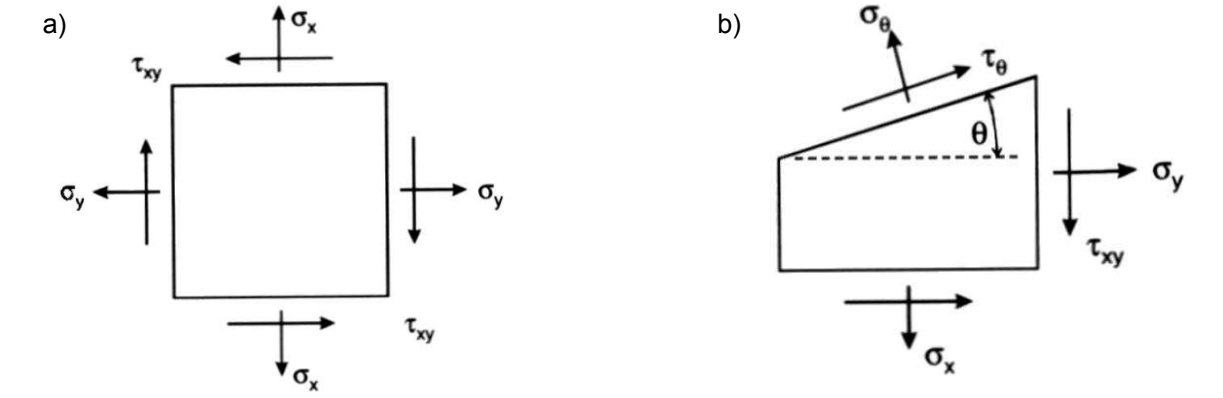

Figure A1 – Plane stress loading of a plate [32]

Static equilibrium on figure A1 b) is used to determine the stresses acting on a plane with an angle θ measured counterclockwise. The stresses are:

$$\sigma_\theta = \frac{\sigma_X + \sigma_Y}{2} + \frac{\sigma_X - \sigma_Y}{2} cos(2\theta) + \tau_{XY} sin(2\theta) \quad (A.1)$$

$$\tau_\theta = \frac{\sigma_X - \sigma_Y}{2} sin(2\theta) - \tau_{XY} cos(2\theta) \quad (A.2)$$

Strains can be determined substituting σ_X for ε_X, σ_Y for ε_Y and τ_{XY} for $\frac{\gamma_\theta}{2}$ in the expressions A.1 and A.2:

$$\varepsilon_\theta = \frac{\varepsilon_X + \varepsilon_Y}{2} + \frac{\varepsilon_X - \varepsilon_Y}{2} cos(2\theta) + \frac{\gamma_{XY}}{2} sin(2\theta) \quad (A.3)$$

$$\gamma_\theta = (\varepsilon_X - \varepsilon_Y) sin(2\theta) - \gamma_{XY} cos(2\theta) \quad (A.4)$$

The coordinate system having the maximum magnitude of normal stresses can be found doing $\frac{d\sigma_\theta}{d\theta} = 0$, obtaining:

$$\theta = \frac{1}{2} tan^{-1}\left(\frac{2\tau_{XY}}{\sigma_X - \sigma_Y}\right) \quad (A.5)$$

So the principal normal stresses can be found substituting A.5 into A.2, obtaining:

$$\sigma_1, \sigma_3 = \frac{\sigma_X + \sigma_Y}{2} \pm \sqrt{\left(\frac{\sigma_X - \sigma_Y}{2}\right)^2 + {\tau_{XY}}^2} \quad (A.6)$$

Since a 2D stress state is supposed:

$$\sigma_2 = 0 \quad (A.7)$$

Annex B – ANSYS APDL Code

```
FINISH

/clear,all


!!!!!!!!!!!!!!!!!!!!!!!!!!!!!!!!!!

!!!!GEOMETRY, MESH & MATERIAL PROPERTIES

!!!!!!!!!!!!!!!!!!!!!!!!!!!!!!!!!!

!Pre-Processor

/PREP7

ET,1,SOLID186


!Material Properties

Eyoung=44.8e9

niu_P=0.35

Rho=1770

T_yield=201e6


MP,EX,1,Eyoung,

MP,PRXY,1,niu_P,

!Mkin

TB,MKIN,1                       ! Activate a data table

TBTEMP,,STRAIN                          ! Next TBDATA values are strains

TBDATA,1,T_yield/Eyoung,2.956E-2,5.827e-2,9.985E-2! Strains for all temps

TBTEMP,0.0                              ! Temperature = 0.0

TBDATA,1,T_yield,246.17E6,270.3e6,291.71e6! Stresses at temperature = 0.0   ! Stresses at
temperature = 500

TBPLOT,MKIN,1


MPTEMP,,,,,,,,

MPTEMP,1,0
```

```
MPDATA,DENS,1,,Rho
!Specimen Geometry
!Points
K,1,0,-50e-3,0,
K,2,6e-3,-50e-3,0,
K,3,6e-3,-16e-3,0,
K,4,3.75e-3,0,0,
K,5,54.55e-3,0,0,
K,6,0,-16e-3,0
K,7,0,0,0

!!!!!!!!!!!!!!!!!!!!!!!!!!!!!!!!!!!!!!!!!!!!!!!!!!!
!!!!!!Controlled Geometry
!!!!!!!!!!!!!!!!!!!!!!!!!!!!!!!!!!!!!!!!!!!!!!!!!!!
Ndiv=12!Ndiv must be even and Ndiv2 too;    !8;12;4
Ndiv2=6                         !4;6;2
!Lines
L,1,2,Ndiv2
L,2,3,Ndiv*50/22
LARC,3,4,5,54.55e-3,Ndiv!*2
L,6,3,Ndiv2
L,4,7,Ndiv2
L,7,6,Ndiv!*2
L,6,1,Ndiv*50/22

!Geometry(Areas & Volumes) ; Mesh
AL,7,1,2,4
AL,3,4,5,6

ARSYM,Y,1, 2,1 , ,0,0
```

```
NUMMRG,all
VROTAT,1,2,3,4,,,6,1,360,,
NUMMRG,all
VMESH,all

!!!!!!!!!!!!!!!!!!!!!!!!!!!!!!!!!!!!
!!!!TRANSIENT ANALYSIS & SOLUTION
!!!!!!!!!!!!!!!!!!!!!!!!!!!!!!!!!!!!
 FINISH
/SOL
ANTYPE,4
TRNOPT,FULL
LNSRCH,1 !ACTIVATES LINE SEARCH
LUMPM,0
NLGEOM,1
NEQIT,30  ! MAXIMUM ITERATIONS NUMBER: 31

NUM_CILCOS=1
DELTIM,0.005,0,0.1*NUM_CILCOS !Defines how time changes
OUTRES,ERASE
OUTRES,ALL,ALL
TIME,0.1*NUM_CILCOS

DA,5,all,0
DA,18,all,0
DA,44,all,0
DA,31,all,0
DTRAN

*DIM,NIU_P_1,TABLE,60,1,1,TIME,PRESSURE,
```

```
*TREAD,NIU_P_1,'NIU_TETA_2','txt','.\Desktop\Tese Recta Final_2009_10_3\ANSYS\Excel\',2,
SFA,27,1,PRES, %NIU_P_1%
SFA,40,1,PRES, %NIU_P_1%
SFA,51,1,PRES, %NIU_P_1%
SFA,14,1,PRES, %NIU_P_1%
SBCTRAN

*DIM,M_TAU_1,TABLE,60,1,1,TIME,PRESSURE,
*TREAD,M_TAU_1,'TAU_TETA_2','txt','.\Desktop\Tese Recta Final_2009_10_3\ANSYS\Excel\',2,
*DIM,TAU_1,TABLE,60,1,1,TIME,PRESSURE,
*TREAD,TAU_1,'M_TAU_TETA_2','txt','.\Desktop\Tese Recta Final_2009_10_3\ANSYS\Excel\',2,

SFE,5750,4,PRES, ,%TAU_1%, , ,
SFE,5751,4,PRES, ,%TAU_1%, , ,
SFE,5500,5,PRES, ,%TAU_1%, , ,
SFE,5503,5,PRES, ,%TAU_1%, , ,
SFE,3397,5,PRES, ,%TAU_1%, , ,
SFE,3394,5,PRES, ,%TAU_1%, , ,
SFE,3645,4,PRES, ,%TAU_1%, , ,
SFE,3644,4,PRES, ,%TAU_1%, , ,
SFE,3883,5,PRES, ,%M_TAU_1%, , ,
SFE,3880,5,PRES, ,%M_TAU_1%, , ,
SFE,3402,4,PRES, ,%M_TAU_1%, , ,
SFE,3401,4,PRES, ,%M_TAU_1%, , ,
SFE,1295,4,PRES, ,%M_TAU_1%, , ,
SFE,1296,4,PRES, ,%M_TAU_1%, , ,
SFE,1774,5,PRES, ,%M_TAU_1%, , ,
SFE,1777,5,PRES, ,%M_TAU_1%, , ,
```

Annex C – Matlab Principal Function

```
%%%%%%%%%%%%%%%%%%%%%%%%%%%%%%%%%%%%%%%%%%%%%%%%%%%%%%%%%%%%%%%%%%%%%%%%%%%%%%%
%%Author: Agostinho Matos; 54808; Instituto Superior Técnico Lisboa; 2010%%
%%%%%%%%%%%%%%%%%%%%%%%%%%%%%%%%%%%%%%%%%%%%%%%%%%%%%%%%%%%%%%%%%%%%%%%%%%%%%%%
clear all %clean all variables
clc  %clean console
%% LOADING VARIABLES & LOAD SELECTION->> PROGRAMME INPUT
k_G=40;%20;%8*10;          %temporal discretization in k_G+1 points
%In flowers case, the first petal has k_G+1 points and the rest k_G points

TT_G=0.1;        %Period of the load
Load_Select=3;   %Number of the selected load
niu_x_G=204e6;   %Sigma.x Applied Stress
%% RUNS SELECTED LOAD
switch Load_Select
    case 1
        [XXaxial_G,YYaxial_G,YYtor_G]=Loads_1(k_G,TT_G,niu_x_G);
    case 2
        [XXaxial_G,YYaxial_G,YYtor_G]=Loads_2(k_G,TT_G,niu_x_G);
    case 3
        [XXaxial_G,YYaxial_G,YYtor_G]=Loads_3(k_G,TT_G,niu_x_G);
    case 4
        [XXaxial_G,YYaxial_G,YYtor_G]=Loads_4(k_G,TT_G,niu_x_G);
    case 5
        [XXaxial_G,YYaxial_G,YYtor_G]=Loads_5(k_G,TT_G,niu_x_G);
    case 6
        [XXaxial_G,YYaxial_G,YYtor_G]=Loads_6(k_G,TT_G,niu_x_G);
    case 7
        [XXaxial_G,YYaxial_G,YYtor_G]=Loads_7(k_G,TT_G,niu_x_G);
    case 8
        [XXaxial_G,YYaxial_G,YYtor_G,TT_G]=Loads_8(k_G,TT_G,niu_x_G);
        XXaxial_G=XXaxial_G';
        YYaxial_G=YYaxial_G';
        YYtor_G=YYtor_G';
    case 9
        [XXaxial_G,YYaxial_G,YYtor_G,TT_G]=Loads_9(k_G,TT_G,niu_x_G);
        XXaxial_G=XXaxial_G';
        YYaxial_G=YYaxial_G';
        YYtor_G=YYtor_G';
    end
```

```
%% GRAPHICAL PLOTS OF THE APPLIED LOAD
scrsz = get(0,'ScreenSize');
figure('Position',[10 scrsz(4)/2+30 scrsz(3)/5 scrsz(4)/2.812])
plot(YYaxial_G/1e6,sqrt(3)*YYtor_G/1e6)%,YA2/1e6,YT2*sqrt(3)/1e6)
xlabel(texlabel('sigma (MPa)'))
ylabel(texlabel('tau[3^(1/2)] (MPa)'))
figure('Position',[10+290 scrsz(4)/4+100 scrsz(3)/3 scrsz(4)/3])
plot(XXaxial_G,YYaxial_G/1e6,'--bs',XXaxial_G,YYtor_G/1e6,'--ko')
legend(texlabel('sigma (MPa)'),texlabel('tau (MPa)'))
xlabel('Time (s)')
ylabel('Loads (MPa)')
%% DAMAGE PARAMETER VARIABLES & D.P. SELECTION->> PROGRAMME INPUT
Parameter_select=2; %selection of the damage parameter
k_2_G=90;      %angular parameter discretization in k_2+1 points% It is
suitable to be an even number to avoid artifacts using griddata function
const_F=0.15;   %Findley model constant
const_B_M=0.321; %Brown Miller model constant
E_yg=44.8e9;
nn=0.35;        %Poisson coefficient
const_F_S=0.231; %Fatemi Socie model constant
niu_ced_G=201e6; %Yield stress
%% DETERMINE SIGMA_TETA AND TAU_TETA && DO GRAPHICAL PLOT OF THEM
[Vec_time_G,Vec_teta_G,niu_teta_G,tau_teta_G]=Tension_Teta(k_2_G,TT_G,XXaxi
al_G,YYaxial_G,YYtor_G);
[X,Y]=meshgrid(-90:180/(k_2_G):90,0:TT_G/(size(XXaxial_G,1)-1):TT_G);
Z=griddata(Vec_teta_G,Vec_time_G,niu_teta_G/1e6,X,Y);
figure('Position',[10+800 scrsz(4)/2+100 scrsz(3)/3 scrsz(4)/4])
surf(X,Y,Z)
xlabel(texlabel('theta (Degrees)'))
zlabel(texlabel('sigma_theta (MPa)'))
ylabel('Time (s)')
colormap Summer
Z=griddata(Vec_teta_G,Vec_time_G,tau_teta_G/1e6,X,Y);
figure('Position',[10+800 scrsz(4)/4-100+100 scrsz(3)/3 scrsz(4)/4])
surf(X,Y,Z)
xlabel(texlabel('theta (Degrees)'))
zlabel(texlabel('tau_theta (MPa)'))
ylabel('Time (s)')
colormap Summer
%% RUNS A DAMAGE PARAMETER FOR THE SELECTED LOAD
switch Parameter_select
```

```
    case 1
        [P_2D,P_3D]=P_Findley(k_2_G,const_F,TT_G,niu_teta_G,tau_teta_G);
        figure('Position',[10 50 scrsz(3)/5 scrsz(4)/3])
        plot(-90:180/(k_2_G):90,P_2D/1e6,'--bs')
        %legend('Findley Parameter')
        xlabel(texlabel('theta (Degrees)'))
        ylabel('Findley Parameter (MPa)')
        colormap Summer
    case 2
[P_2D,P_3D]=P_Brown_Miller(k_2_G,const_B_M,E_yg,nn,TT_G,YYaxial_G,YYtor_G);
        figure('Position',[10 50 scrsz(3)/5 scrsz(4)/3])
        plot(-90:180/(k_2_G):90,P_2D/1e6,'--bs')
        xlabel(texlabel('theta (Degrees)'))
        ylabel('Brown & Miller Parameter (MPa)')
        colormap Summer
    case 3
[P_2D,P_3D]=P_Fatemi_Socie(niu_ced_G,k_2_G,const_F_S,E_yg,nn,TT_G,YYaxial_G
,YYtor_G,niu_teta_G);
        figure('Position',[10 50 scrsz(3)/5 scrsz(4)/3])
        plot(-90:180/(k_2_G):90,P_2D/1e6,'--bs')
        xlabel(texlabel('theta (Degrees)'))
        ylabel('Fatemi & Socie Parameter (MPa)')
        colormap Summer
    case 4
      [P_2D,P_3D]=P_S_W_T(nn,k_2_G,E_yg,TT_G,niu_teta_G,YYaxial_G,YYtor_G);
        figure('Position',[10 50 scrsz(3)/5 scrsz(4)/3])
        plot(-90:180/(k_2_G):90,P_2D/1e6,'--bs')
        xlabel(texlabel('theta (Degrees)'))
        ylabel('SWT Parameter (MPa)')
        colormap Summer
    case 5
[P_2D,P_3D]=P_Liu_I(k_2_G,E_yg,nn,TT_G,YYaxial_G,YYtor_G,niu_teta_G,tau_tet
a_G);
        figure('Position',[10 50 scrsz(3)/5 scrsz(4)/3])
        plot(-90:180/(k_2_G):90,P_2D/1e6,'--bs')
        xlabel(texlabel('theta (Degrees)'))
        ylabel('Liu I Parameter (MPa)')
        colormap Summer
    case 6
[P_2D,P_3D]=P_Liu_II(k_2_G,E_yg,nn,TT_G,YYaxial_G,YYtor_G,niu_teta_G,tau_te
ta_G);
```

```
        figure('Position',[10 50 scrsz(3)/5 scrsz(4)/3])
        plot(-90:180/(k_2_G):90,P_2D/1e6,'--bs')
        xlabel(texlabel('theta (Degrees)'))
        ylabel('Liu II Parameter (MPa)')
        colormap Summer
end
figure('Position',[300 50 scrsz(3)/3 scrsz(4)/3])
Z=griddata(Vec_teta_G,Vec_time_G,P_3D/1e6,X,Y);
surf(X,Y,Z)
xlabel(texlabel('theta (Degrees)'))
zlabel('Parameter (MPa)')
ylabel('Time (s)')
colormap Summer
AUX_G=-90:180/(k_2_G):90;
        [A,B]=max(P_2D);
     for i=1:B-1
        AUX_2(i)=(abs((P_2D(i)-A)/A*100));
     end
        AUX_2(B)=100;
     for i=B+1:k_2_G+1
        AUX_2(i)=(abs((P_2D(i)-A)/A*100));
     end
[A2,B2]=min(AUX_2);
K_ERR=min(AUX_2);
Parameter_Maximum_Values_MPa={'TT1 (deg.)','P_TT1 (MPa)','TT2
(deg.)','P_TT2 (MPa)','Relative
error %';AUX_G(B),A/1e6,AUX_G(B2),P_2D(B2)/1e6,K_ERR}

'PRESS ENTER IN THIS CONSOLE TO CLOSE THE GRAPHICAL INFO'
pause
close all
%Fatigue Life calculation
[NFFF]=Calcula_Vida(A,Parameter_select);
vpa(NFFF,7)
```